

Analysis Note for the
2006 EEMC Neutral Pion Paper:
Part II

Argonne/Valparaiso STAR Spin Group

May 16, 2013

Contents

1	Introduction	2
2	Data Selection	3
2.1	Run Selection	3
2.2	Trigger Thresholds	4
2.3	Event Selection	5
2.4	Luminosity and Polarization Values	6
2.5	Data, Monte Carlo Comparison	7
3	Analysis	17
3.1	Formalism	17
3.2	Background Subtraction	23
3.3	Unfolding and Reconstruction Efficiency	42
3.4	Trigger Efficiency	46
4	Systematics	49
4.1	Vertical Scale Uncertainties	49
4.2	Non-Vertical Scale Uncertainties	49
4.3	Table of Results	54
5	Results	56
5.1	Cross Section	56
5.2	Longitudinal Spin Asymmetries	56
5.3	Transverse Spin Asymmetry	56
A	Run Lists	61
A.1	Longitudinal Runs for both Asymmetry and Cross Section	61
A.2	Additional Longitudinal Runs for the Cross Section	61
A.3	Transverse Runs for both Asymmetry and Cross Section	62
A.4	Additional Transverse Runs for the Cross Section	62

Chapter 1

Introduction

This is part II of the Analysis Notes in support of the publication of the EEMC measurement of the π^0 cross section and spin asymmetries (longitudinal and transverse) from 2006 data. Part I focuses on general studies of reconstructing photons and π^0 s with the STAR EEMC, carried over the past many years by a variety of individuals. Some of these studies directly relate to the procedures and methods used for the paper, while many studies are only indirectly related or led to dead ends. However, the studies in Part I have been essential in understanding the response of the EEMC and in forming the algorithms and methods currently used.

Part II focuses on the specific, final choices, which directly lead to the results proposed for publication. In terms of the data flow, Part I describes how to reconstruct π^0 s with the EEMC, with the EEMC data, hits, clusters, photons, π^0 s, etc., being saved EEmcTrees. Part II focus on how to use the information in the EEmcTrees to determine the cross section and spin asymmetries.

Chapter 2

Data Selection

2.1 Run Selection

Run lists for the transverse and second longitudinal polarization periods of run6 are generated as described below. The final list of runs are given in Appendix A. A spreadsheet with more details is available in Ref. [1].

A number of checks are made, the first of which is the “runQA” organized by Jim Sowinski and performed by a number of collaborators shortly after the run was taken (Ref. [2]), resulting in a list of priority or good runs (Ref. [3]). During the runQA, online plots are checked, and rates and notes in the shift log are evaluated. The run length is required to be more than 60 sec. Runs that are labeled “bad” at RTS are omitted, while those labeled “bad” or “questionable” by the shift leader are included for the runQA.

Scripts have also been written to check that luminosity (Ref. [4]) and polarization (Ref. [5]) information was available for each run. Furthermore, the run log has been checked for each run to ensure that the desired trigger was available for that run (not a test run, for example), and that at least the EEMC and ESMD were read out. Finally, some runs have been found not to have MuDsts available—these runs are not included.

For the longitudinal runs, a list existed from the dissertation of Weihong He (Ref. [6]), which has been used as the basis for the final run list. These 347 runs are divided into three categories: those with some problems found (19); those with only EEMC, ESMD, and good trigger, but no TPC (29); and the rest with TPC, EEMC, ESMD, and good trigger (299). There are also five other categories of runs from J. Sowinski’s list: min bias runs with TPC, EEMC, ESMD (3); min bias runs with EEMC, ESMD, but no TPC (83); possible good runs with TPC, EEMC, ESMD (37); possible good runs with only EEMC, ESMD (4); and other runs not to be included (47) due to lack of MuDsts, luminosity or polarization information. The total number of longitudinal runs in all lists is 521. The longitudinal asymmetry results use the “good” runs, with the TPC, that are not minbias runs.

For the transverse runs, the list from the runQA has been the starting point. Some runs not including the EEMC and ESMD or those involving test triggers have been removed. The remaining runs are sorted into five categories: good data runs with TPC, EEMC, ESMD (404); good data runs with only EEMC and ESMD, but no TPC (35); min bias runs with TPC, EEMC, ESMD (6); min bias runs with only EEMC and ESMD (93); and bad runs with no luminosity information (123). The total number of transverse runs in all lists is 661. The transverse asymmetry result uses the 404 runs in the the first category.

Two final checks have been placed on all runs. First, for each run, the ratio of `eemc-http-mb-L2gamma` to min bias triggers, corrected for prescaling, is computed. Several runs passing all other requirements were found to cause outlying points and were removed from the run list. The ratio of the number of π^0 candidates within the mass peak region to the number of `eemc-http-mb-L2gamma` triggers is also computed. No runs were found to cause outlying points. The results for both checks are shown in Figure 2.1.

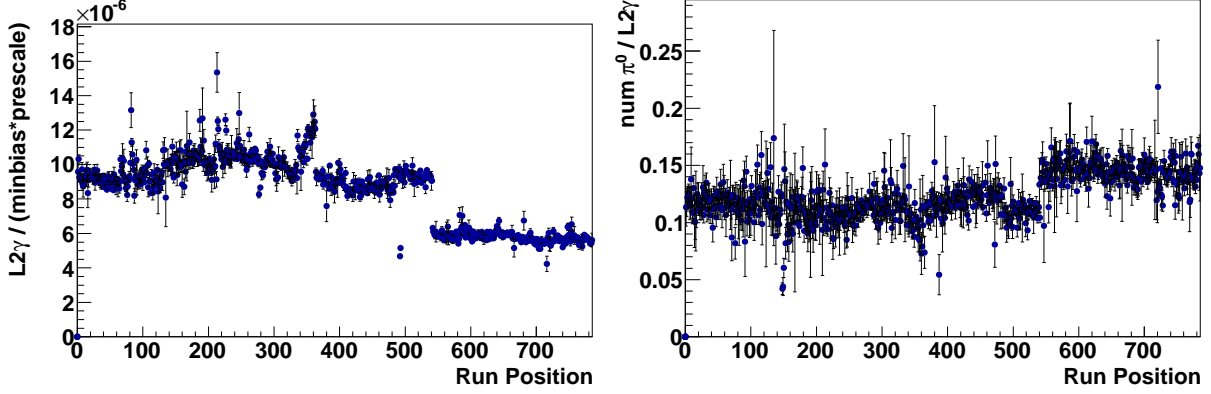


Figure 2.1: Left panel: the ratio of `eemc-http-mb-L2gamma` triggers to min bias triggers, corrected for prescaling. Right panel: ratio of the number of π^0 candidates with $0.1 < M_{\gamma\gamma} < 0.2 \text{ GeV}/c^2$ to the number of L2gamma triggers. The transverse runs correspond to x -axis values of 1-482 and runs from the second longitudinal period correspond to 483-799.

Label	HT	TP	First Run	Last Run	Running Condition
a	12 (2.6 GeV/c)	17 (3.8 GeV/c)	7082082	7097000	pp200 long
b	12 (2.6 GeV/c)	17 (3.8 GeV/c)	7097000	7100031	pp200 trans
c	13 (2.8 GeV/c)	21 (4.7 GeV/c)	7100052	7129067	pp200 trans
d	12 (2.6 GeV/c)	20 (4.5 GeV/c)	7130037	7132029	pp200 long
e	17 (3.8 GeV/c)	20 (4.5 GeV/c)	7132045	7133051	pp200 long
f	16 (3.5 GeV/c)	20 (4.5 GeV/c)	7133052	7156040	pp200 long

Table 2.1: L0 hardware thresholds used in 2006 for the `eemc-http-mb-L2gamma` trigger [7]. The energy values are approximate, based on Ref. [9].

2.2 Trigger Thresholds

The main analysis is performed with the `eemc-http-mb-L2gamma` trigger which requires at least one high tower in the EEMC having E_T above the high tower (HT) threshold, with the E_T of the 3x3 block of towers surrounding the high tower to be above the trigger patch (TP) threshold. The minbias condition (BBC coincidence) is also required. The HT and TP are applied at both a level-0 (L0) stage (using DSM values) and an level-2 (L2) stage (using energy). The `eemc-http-mb-L2gamma` trigger is given the number of 117647 (during the first longitudinal running), 127647 (during the transverse running), 137647 (during the second longitudinal running), and 6 (for testing values of the thresholds regardless of the beam polarization orientation).

One needs to distinguish between the hardware triggers, used when taking the data, versus the software triggers, computed via STAR's trigger emulator. Both hardware and software trigger cuts are applied in this analysis. A cut on the software trigger is used for Monte Carlo data, where there is no hardware trigger, as well as the real data, to smooth out variations in the pedestals and gains (since the pedestals available when the run was taken may not be the optimal estimate of the pedestals). A cut on the hardware trigger is also used for the data.

As the L0 and L2 thresholds have not always been changed in unison, two tables of hardware trigger thresholds (and their times of applicability) are provided, Table 2.1 for the L0 thresholds and Table 2.2 for the L2 thresholds. Other test values that do not enter into runs in the run list are not included in these tables. The threshold levels have been given a single letter label ('a' through 'f') to distinguish the threshold sets.

The software trigger thresholds are given in Table 2.3. To keep track of various choices of software

HT	TP	Running Condition
3.4	5.4	pp200 trans
2.9	4.5	pp200 2nd long
3.7	5.1	pp200 2nd long
3.7	5.2	pp200 2nd long
3.8	5.0	Monte Carlo

Table 2.2: L2 hardware thresholds used in 2006 for the `eemc-http-mb-L2gamma` trigger [8]. The Monte Carlo values are the thresholds used for both the Pythia and BFC level filters.

Label	L0		L2	
	HT [DSM]	TP [DSM]	HT [GeV]	TP [GeV]
f	16 (3.5 GeV/c)	20 (4.5 GeV/c)	3.7	5.2
g	18 (4.0 GeV/c)	21 (4.7 GeV/c)	3.9	5.5
h	19 (4.2 GeV/c)	22 (5.0 GeV/c)	4.2	6.0
i	19 (4.2 GeV/c)	22 (5.0 GeV/c)	4.326	6.18

Table 2.3: Trigger thresholds for the software trigger. The energy values for the L0 thresholds are approximate, based on Ref. [9].

thresholds, different sets of values have been assigned letter designations. The first six designations (‘a’ through ‘f’) correspond to the main six values used during the *pp* running in 2006. The L0 thresholds were raised 1 or 2 DSM for ‘g’ (roughly 5%) and an additional 1 DSM for ‘h’ and ‘i’, approximately 10% above nominal. The L2 threshold ‘f’ was intended to be the nominal value, and ‘g’ was set to 5% above ‘f’. However, the Pythia and BFC filters used a HT threshold of 3.8, and so ‘h’ is set to 10% above the maximum values used (3.8 and 5.2 GeV/c) rather than 10% above ‘f’. The threshold set ‘i’ is set to 3% higher than ‘h’, as various studies have indicated the simulation may have an energy scale which is around 3% [10]. The energy scale difference between data and Monte Carlo is further discussed in Section 3.2.3. The main analysis uses the hardware trigger and software trigger set ‘h’ for the data and software trigger set ‘i’ for the Pythia Monte Carlo.

2.3 Event Selection

The cuts used are

- 7-bit bunch crossing not in 31-39, 111-119 and not 20 or 60.
- Exists a TPC vertex with vertex z -position in ± 120 .
- Each photon has detector- η in $[1.11, 1.96]$ [11].
- Physical- η for π^0 candidates in $[0.8, 2.0]$.
- $5 < p_T < 16$ GeV/c¹.
- $M_{\gamma\gamma} < 0.3$ GeV/c²².
- $E_\gamma > 2.0$ GeV (TSIU), $E_\gamma > 1.5$ GeV (IU).
- Preshower energy of each photon < 40 MeV.

¹Some studies used an upper value of 25 GeV/c, but there are few statistics with p_T between 16 and 25 GeV/c. One systematic for the cross section uses data in $4 < p_T < 5$ GeV/c. The asymmetries do not use the data in $12 < p_T < 16$ GeV/c.

²Some studies use up to $M_{\gamma\gamma} < 0.6$ GeV/c².

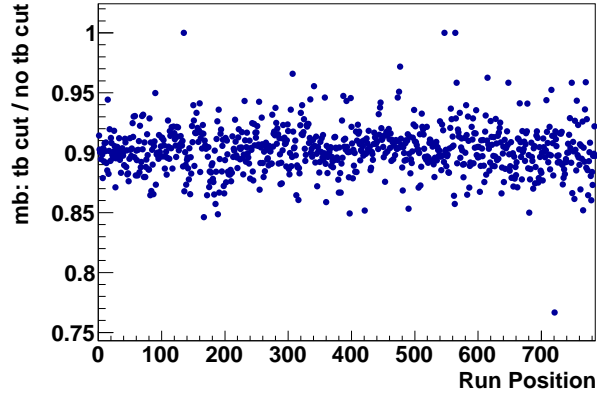


Figure 2.2: Ratio of the number of min bias events with the BBC East-West timing cut to the number without the cut as a function of run position. Both transverse and the second longitudinal run period data are shown.

The first six cuts are based on known, fixed issues: avoiding invalid bunch crossings, matching the vertex cut using in the simulations, avoiding candidates too close to the edge of the EEMC, defining the η and p_T region of sensitivity, and focusing in the general region of the π^0 mass peak. The last two cuts were adjusted to optimize the amount of signal, both the total amount and the signal fraction [12]. Other cuts were also considered, but not found to be effective; see [12, 13].

Note, the mass peak region is defined as $0.1 < M_{\gamma\gamma} < 0.2 \text{ GeV}/c^2$. The background subtraction fits are nominally performed for $0.0 < M_{\gamma\gamma} < 0.3 \text{ GeV}/c^2$. The variation of these ranges is considered in Section sec:sysRangeVar.

2.4 Luminosity and Polarization Values

The polarization values are directly taken from the CNI web pages [5].

The relative luminosities for the spin asymmetries come from the scalar boards. The readout of the scalar board information was provided by S. Trentelage. The number of counts for time bins 7, 8 and 9 are summed for each combination of spin states ($++$, $+-$, $-+$, $-$). These sums are proportional to the luminosities for each spin state combination.

The absolute luminosity (used for the cross section) should not be determined from the scalar boards, as this does not accurately account for dead time. Instead, the number of minbias events, corrected for prescaling, is used. This number is computed both with and without a cut on the BBC time bin being within [6, 10]. The average is used as the number of minbias events, and the difference is taken as a systematic uncertainty (which is dwarfed by other systematic uncertainties). The ratio of the number within the cut to the number without the cut, per run, is plotted in Figure 2.2. The results look sufficiently stable.

The absolute luminosity is then the number of counts divided by the BBC cross section, $26.1 \pm 2 \text{ mbarns}$. The relative uncertainty on the number of counts is much less than the relative uncertainty on the BBC cross section, and so the uncertainty on the BBC cross section is only non-negligible source of the 7.7% (relative) vertical scale uncertainty on the final cross section plot.

The total luminosity per data taking period, as computed according to the above paragraphs, is given in Table 2.4 and denoted “sampled” luminosity. Note, the “total” sampled luminosity is the quantity used for the cross section, and is slightly higher than the sum of the sampled transverse and longitudinal sampled luminosities, due to a few runs being “good” except for problems affecting the spin and/or polarization.

Period	Sampled Luminosity
Trans.	2.8 pb ⁻¹
Long.	4.8 pb ⁻¹
Total	8.0 pb ⁻¹

Table 2.4: Sampled Luminosity per running condition.

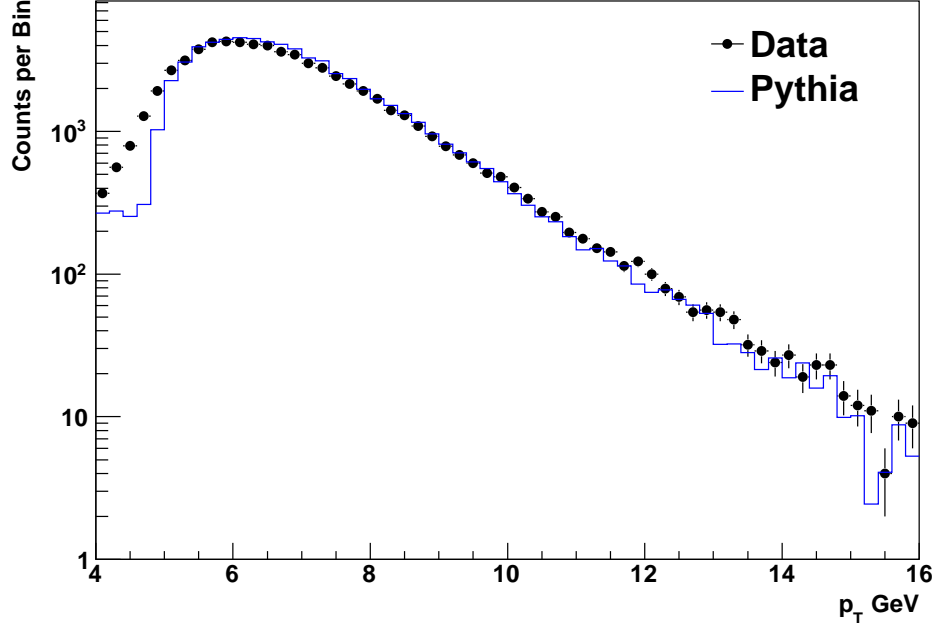


Figure 2.3: Distribution of transverse momentum for π^0 pairs within the peak window for data (black markers) and Pythia (blue histogram). Pythia data is normalized using the 8-16 GeV/ c window.

2.5 Data, Monte Carlo Comparison

A variety of quantities are compared between data and the official Pythia Monte Carlo production [14], some being lower level or more basic quantities, others being higher level.

2.5.1 Lower Level Comparisons

First, the p_T spectrum of π^0 candidates in the mass peak window (and within the usual set of cuts) is compared. The Monte Carlo is normalized so that the integral between 8 and 16 GeV/ c matches that of the data. This same normalization factor is then applied to all of the “lower level comparison” Monte Carlo histograms. The results are shown in Figure 2.3. The agreement is very good for $p_T > 6$ GeV/ c , with the Monte Carlo seeming to miss events at $4 < p_T \lesssim 5.5$ GeV/ c .

The next quantity compared is the “max E_T ,” defined as the maximum tower E_T per event. The max E_T plots are binned according to π^0 candidate p_T , i.e. per event, for each π^0 candidate passing the nominal cuts (including the $M_{\gamma\gamma} < 0.6$ GeV/ c^2 requirement), the maximum tower E_T for the event is added to the histogram corresponding to the p_T bin of the π^0 candidate. The max E_T value should be basically zero until reaching the HT threshold value, rise until reaching almost the TP threshold level, and then fall (due to the falling cross section for higher E_T events).

The results are shown in Figure 2.4. The shape is generally as expected. The data and Monte Carlo show significant disagreement at $4 < p_T < 5$ GeV/ c , but only mild disagreement at $5 < p_T < 6$ GeV/ c and good agreement at $p_T > 6$ GeV/ c .

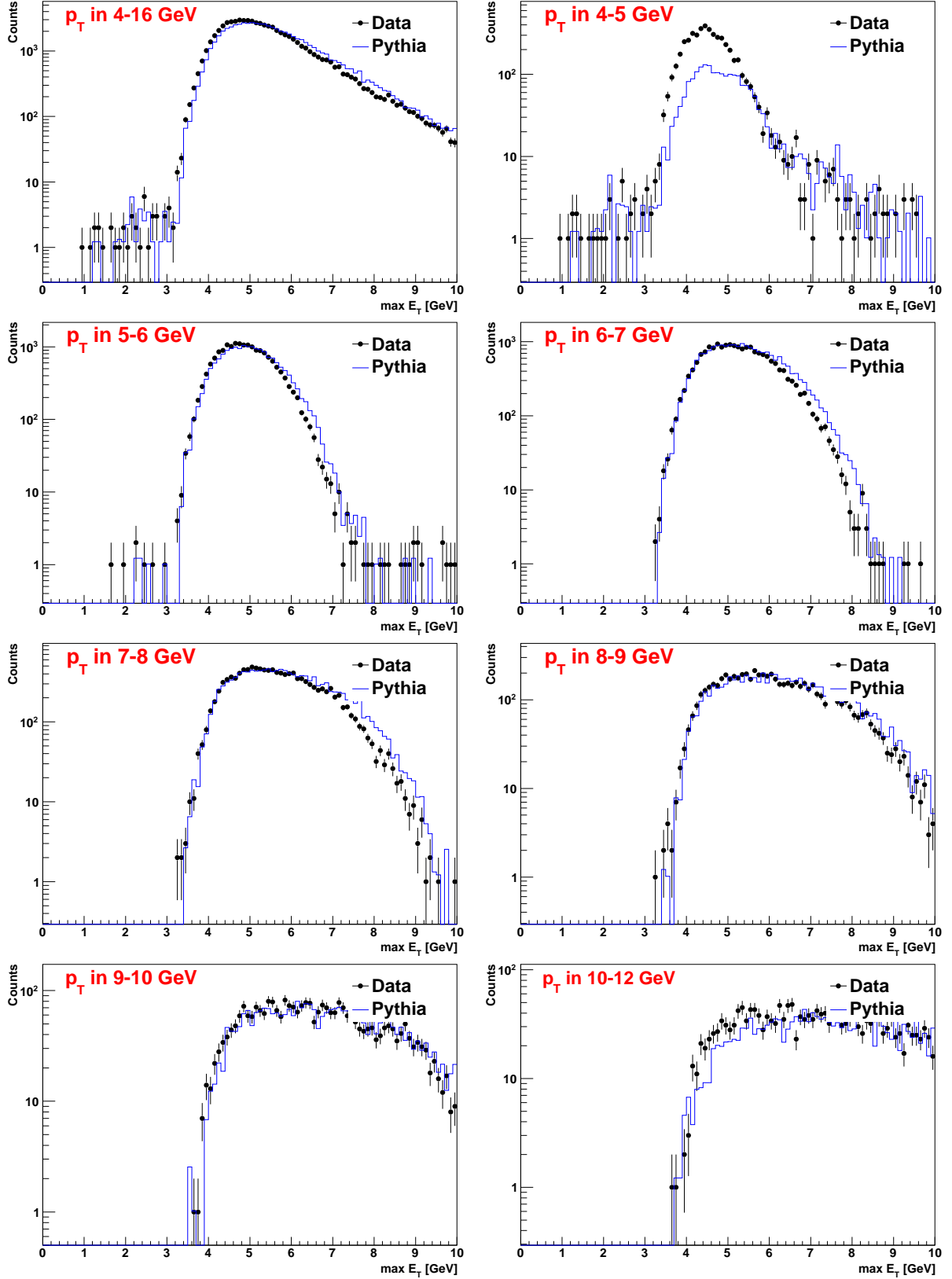


Figure 2.4: A comparison of the distribution of the maximum tower E_T per event versus π^0 candidate p_T for data (black markers) and Pythia (blue histogram).

A similar quantity is the max E_T ratio, the ratio of the max E_T as defined above, divided by the sum of the E_T for the 3x3 patch of towers centered on (and including) the tower with the max E_T . Results are shown in Figure 2.5. Again, a strange discrepancy between data and Monte Carlo is observed for $4 < p_T < 5$ GeV/ c , but at higher p_T the comparison is good.

The last low level comparison is to look at the profile of the max E_T ratio per max E_T bin per π^0 candidate p_T bin. The results are shown in Figure 2.6. The Pythia tends to be slightly higher, but no significant effects are seen—even at $4 < p_T < 5$ GeV/ c .

2.5.2 Higher Level Comparisons

For the higher level comparisons, each histogram is normalized to have an integral of unity. The quantities compared all correspond to the two-photon system, i.e. the π^0 candidate, and all the usual cuts are used. The quantities compared are the mass $M_{\gamma\gamma}$ (Figure 2.7), energy (Figure 2.8), energy asymmetry $Z_{\gamma\gamma}$ (Figure 2.9), physical η (Figure 2.10), and the vertex Z position (Figure 2.11). Note the energy asymmetry is defined as the absolute value of the difference in the two photon energies divided by the sum.

The high level comparison shows that the data has more low mass events in the $4 < p_T < 5$ GeV/ c bin, and that the η and vertex Z distributions are also off in these two bins. For $p_T > 5$ GeV/ c the comparison is generally quite good.

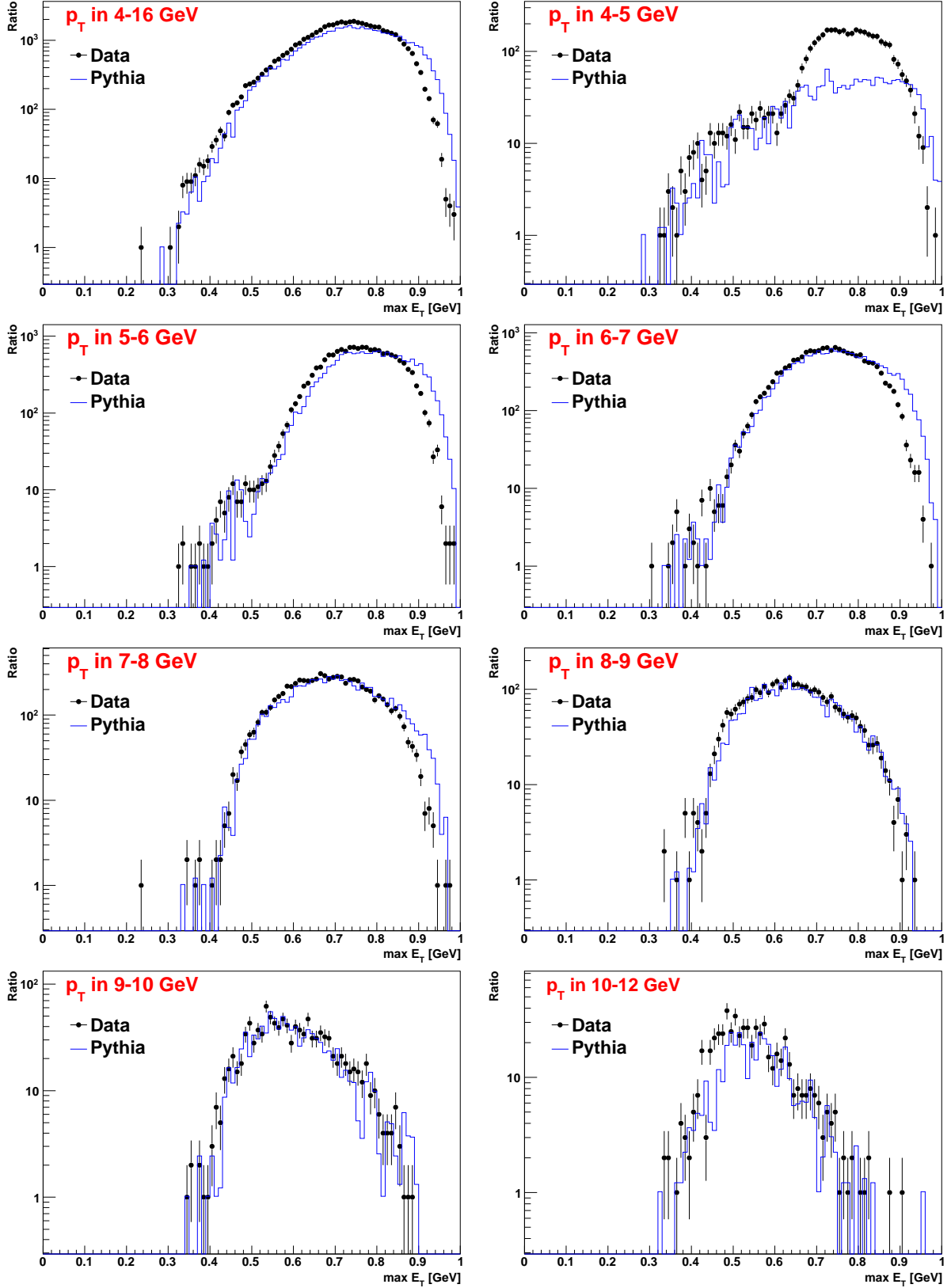


Figure 2.5: Distribution of the $\max E_T$ ratio quantity (described in the text) for data (black markers) and Pythia (blue histogram) versus π^0 candidate p_T .

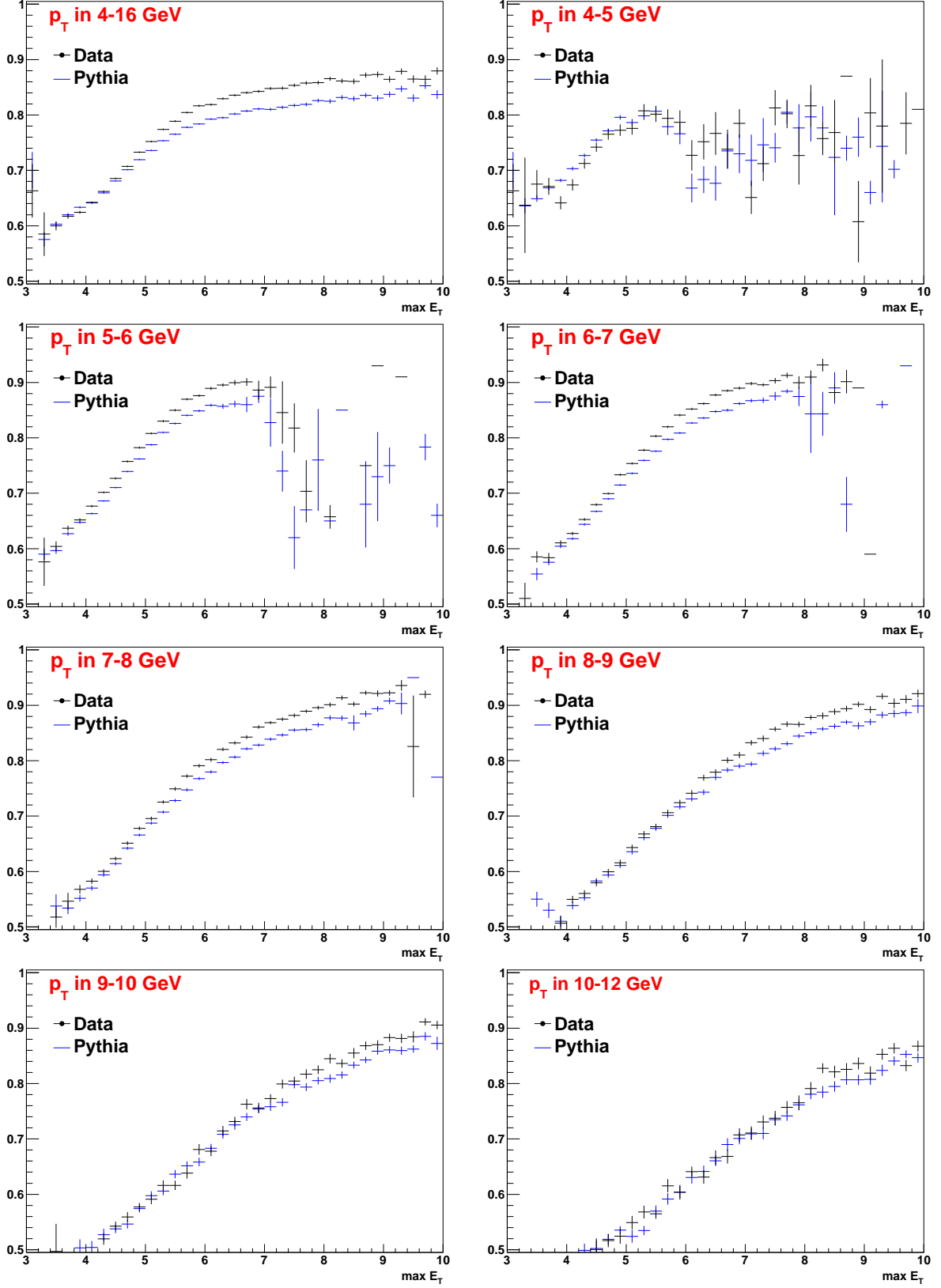


Figure 2.6: Max E_T ratio vs max E_T (as defined in the text) for data (black markers) and Pythia (blue histogram) versus π^0 candidate p_T .

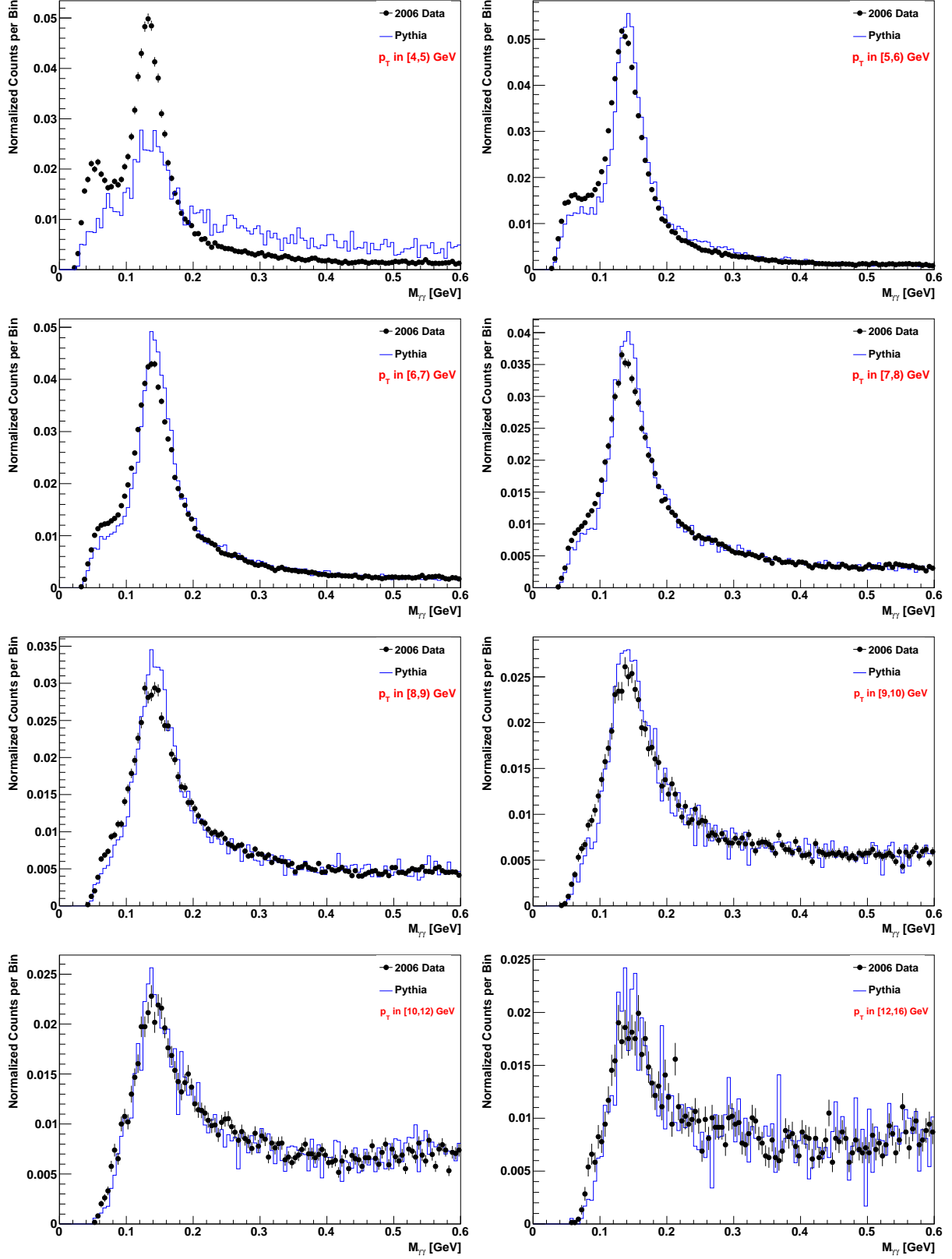


Figure 2.7: Invariant mass distribution for data (black markers) and Pythia (blue histogram) versus π^0 candidate p_T .

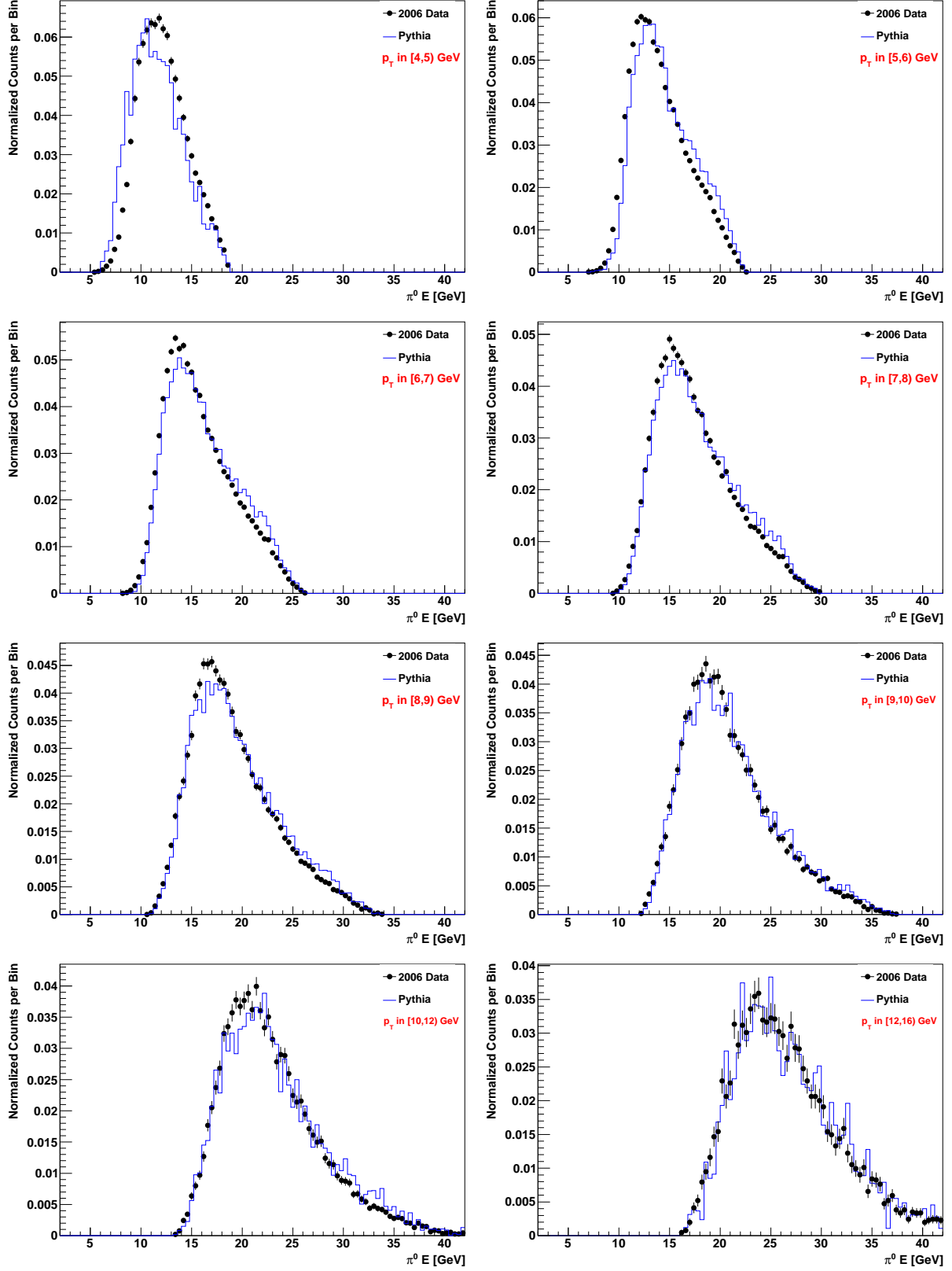


Figure 2.8: Energy distribution for data (black markers) and Pythia (blue histogram) versus π^0 candidate p_T .

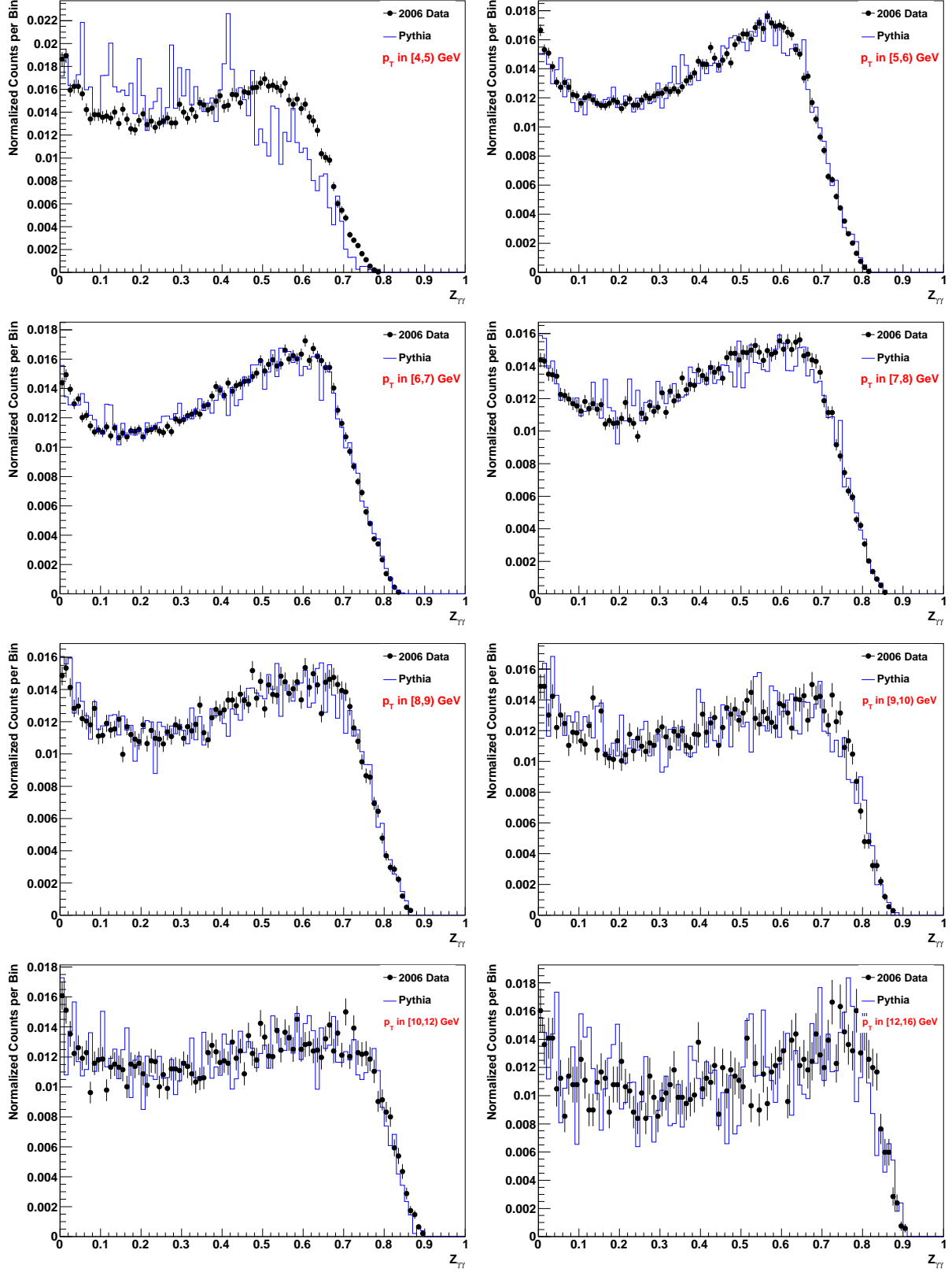


Figure 2.9: Energy asymmetry distribution for data (black markers) and Pythia (blue histograms) versus π^0 candidate p_T .

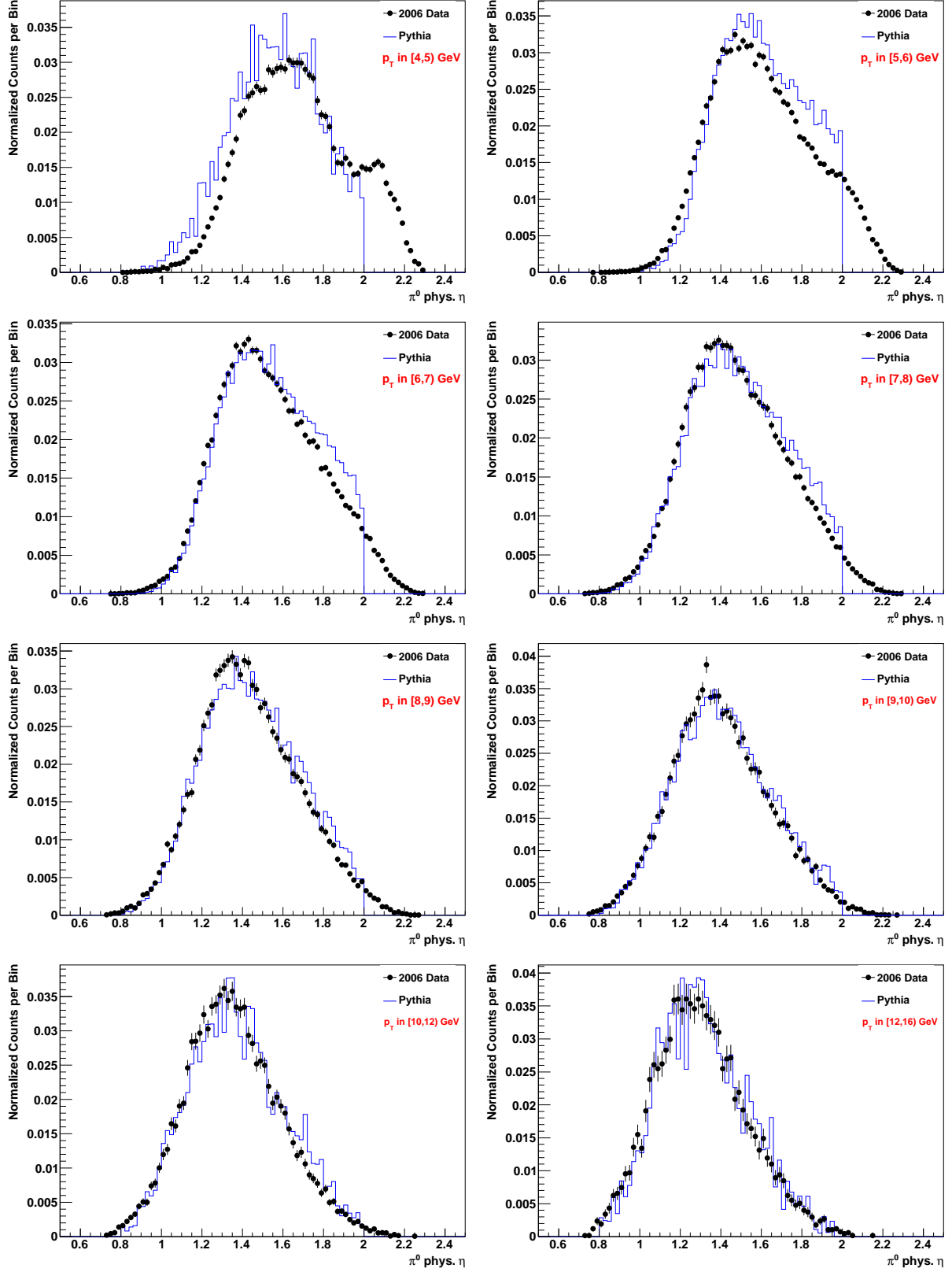


Figure 2.10: Physical η distribution for data (black markers) and Pythia (blue histograms) versus π^0 candidate p_T .

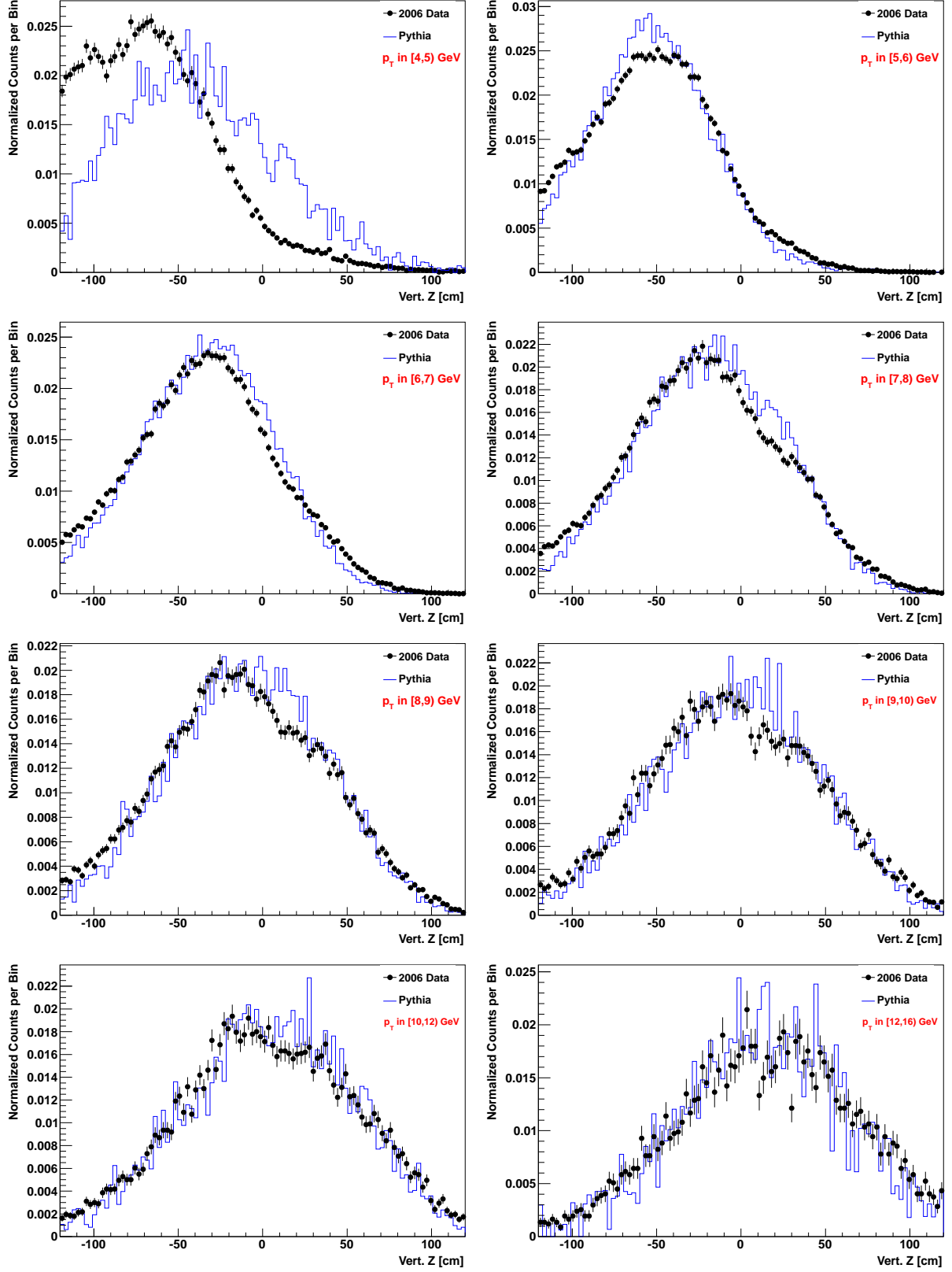


Figure 2.11: Vertex Z position distribution for data (black markers) and Pythia (blue histograms) versus π^0 candidate p_T .

Chapter 3

Analysis

A chart showing the general analysis flow is shown in Figure 3.1. The starting point is the EEmcTrees with the π^0 merger afterburner, both of which are described in Part I of this Analysis Note. The histograms are made of the simulation data separately for the signal and backgrounds, and these histogram templates are then fit with functional forms. The histograms for the data are also generated from the EEmcTrees, and a fit is performed to determine the amount of signal under the π^0 peak. The result is the number of (background subtracted) π^0 s per bin. To determine the cross section, an additional step of p_T -unfolding is applied, while the spin asymmetries are directly calculated from the background subtracted number of π^0 s. Unfolding is not applied to the spin asymmetries as it is not needed, since dependence of the asymmetries on p_T is sufficiently weak.

The type of bin varies for each final result: for the cross section, the bins are π^0 p_T bins; for the longitudinal spin asymmetries, the bins are beam spin states and π^0 p_T ; and for transverse spin asymmetries, the bins are the beam spin states and either the π^0 x_F or the π^0 p_T . A 2D binning in p_T and physical η is also considered for the cross section.

This chapter first presents the mathematical formalism of the entire analysis procedure, and then has sections focusing on the results of each major step: the background subtraction, unfolding and reconstruction efficiencies, and trigger efficiencies.

3.1 Formalism

For all results, the initial, common step, is to determine the signal fraction s_i per bin and the raw number of π^0 candidates per bin $N_i^{(R)}$. The (background subtracted) number of π^0 s is simply the product $N_i^{(\pi^0)} = s_i N_i^{(R)}$. The standard uncertainty propagation gives

$$\left[\delta^2 N_i^{(\pi^0)} \right]_{(STAT)} = s_i^2 N_i^{(R)}, \quad (3.1)$$

$$\left[\delta^2 N_i^{(\pi^0)} \right]_{(SYS)} = \delta^2 s_i \left(N_i^{(R)} \right)^2 + \dots, \quad (3.2)$$

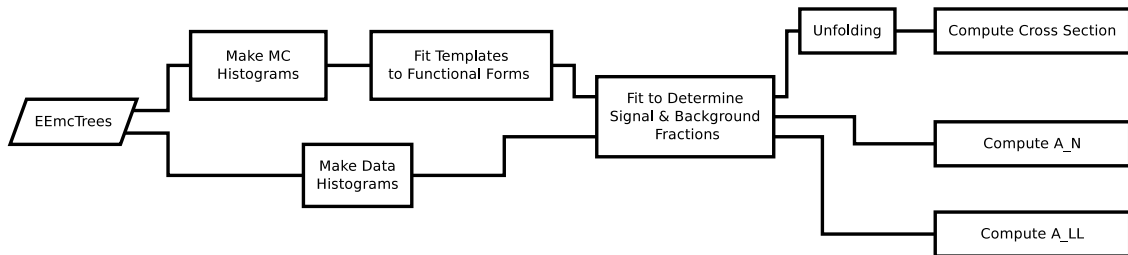


Figure 3.1: Flow chart representing the analysis procedure.

where the dots represent an additional systematic uncertainty that may be added to the number of π^0 s based on the studies of Chapter 4. The computation of the variance on $\delta^2 s_i$ is discussed in Section 3.2.6.

3.1.1 Cross Section Formalism

The guiding formula for unfolding is a Fredholm integral equation,

$$p\left(p_T^{(R)}, \text{rec, trig}\right) = \int dp_T^{(G)} p\left(p_T^{(R)} \mid \text{rec, trig}, p_T^{(G)}\right) p\left(p_T^{(G)}, \text{rec, trig}\right). \quad (3.3)$$

This formula quantifies the statement that the probability of a reconstructed photon with reconstructed $p_T = p_T^{(R)}$, in an event satisfying the trigger, is the integral over all generated p_T (i.e. $p_T^{(G)}$) of the product of (a) the conditional probability of a π^0 having reconstructed $p_T = p_T^{(R)}$ given that it had generated $p_T = p_T^{(G)}$ and given that the π^0 is reconstructed and is in an event satisfying the trigger.

By binning in p_T (or equivalently p_T and η), one can reduce the integral equation to a matrix equation

$$N_i^{(\pi^0)} = \sum_j S_{i,j} N_j^{(U)} + N_i^{(IO)}, \quad (3.4)$$

where $S_{i,j}$ is the smearing matrix, $N_j^{(U)}$ is the unfolded number of π^0 counts in a generated p_T bin j , and $N_j^{(IO)}$ is the number of π^0 counts which were generated outside the p_T range of the smearing matrix and which are reconstructed in bin i , i.e. inside the p_T range of the smearing matrix. The quantity $N_i^{(IO)}$ is sometimes denoted the “outside smeared in” background, though it represents real π^0 signals that were just generated outside of a chose p_T range. The quantity $N_j^{(U)}$ is the numeric estimate of the conditional probability $p\left(p_T^{(G)} \mid \text{rec, trig}\right)$, the probability of a generated π^0 with p_T equal to $p_T^{(G)}$, given that the pion is reconstructed and that the event satisfies the trigger. One can alternately define a multiplicative correction factor f_i instead of the linear factor $N_j^{(IO)}$, with the relation

$$N_i^{(\pi^0)} - N_i^{(IO)} = f_i N_i^{(\pi^0)}, \quad (3.5)$$

resulting in the unfolding equation

$$f_i N_i^{(\pi^0)} = \sum_j S_{i,j} N_j^{(U)}. \quad (3.6)$$

The statistical and systematic covariances on the unfolded counts $N_i^{(U)}$, using the standard methods of uncertainty propagation, are

$$\left[\text{Cov}\left(N_i^{(U)}, N_j^{(U)}\right)\right]_{(STAT)} = \sum_k S_{i,k}^{-1} \left(\left[\delta^2 N_k^{(\pi^0)}\right]_{(STAT)}\right) S_{j,k}^{-1}, \quad (3.7)$$

$$\left[\text{Cov}\left(N_i^{(U)}, N_j^{(U)}\right)\right]_{(SYS)} = \sum_k S_{i,k}^{-1} \left(\left[\delta^2 N_k^{(\pi^0)}\right]_{(SYS)} + \sum_\ell \delta^2 S_{k,\ell} \left(N_\ell^{(U)}\right)^2\right) S_{j,k}^{-1} + \dots \quad (3.8)$$

where the uncertainty due to $N_i^{(IO)}$ or f_i has not been explicitly notated. The uncertainty on the smearing matrix S is assumed to be Poisson, $\delta^2 S_{k,\ell} = S_{k,\ell}$, and it is assumed there are no correlations between elements of the smearing matrix. Note the “+...” on the systematic uncertainties indicate that there may be additional contributions to the systematic uncertainty, based on studies in Chapter 4, and also include the systematic uncertainty propagated from the uncertainty on $N_i^{(IO)}$ or f_i .

To relate $N_j^{(U)}$ to the cross section, one must divide by the reconstruction and trigger efficiencies, as well as to account for the phase space, branching ratio, luminosity, and an overall factor of the average p_T per bin.

The formula used for computing the cross section is then (without the explicit reference to bin j)

$$\sigma = \frac{1}{\Delta p_T \Delta \phi \Delta \eta} \frac{1}{\langle p_T \rangle} \frac{1}{BR} \frac{1}{\epsilon_T} \frac{1}{\epsilon_R} \frac{1}{\mathcal{L}} N^{(U)}, \quad (3.9)$$

where $\Delta p_T \Delta \phi \Delta \eta$ is the phase space volume in p_T , ϕ and η , and where $\langle p_T \rangle$ is the average p_T per bin, BR is the branching ratio, ϵ_T and ϵ_R are the trigger and reconstruction efficiencies, and $N^{(U)}$ is the unfolded number of π^0 s, and \mathcal{L} is the luminosity. The computation of the luminosity and its uncertainty is described in Section 2.4. The number of π^0 s and luminosities are summed over all available runs.

Note that since the trigger and reconstruction efficiencies are applied after the the unfolding, they are computed purely with the generated π^0 information. The only reconstruction information needed is whether the reconstructed event passes the trigger.

The uncertainties on the efficiencies, on $\langle p_T \rangle$, and the systematic uncertainty on the unfolded number of counts $N_j^{(U)}$ are propagated to the systematic uncertainty on the cross section. The systematic uncertainty can also have additional contributions, as detailed in Chapter 4. The statistical uncertainty on the cross section is just the propagated uncertainty on the unfolded number of counts, $N_j^{(U)}$. The uncertainty on $\langle p_T \rangle$ is determined using the EEMC energy resolution of $0.16\sqrt{E}/E$ and a nominal η of 1.1.

The uncertainty on the branching ratio is negligible compared to other uncertainties, and there is no uncertainty assigned related to the phase space factor. The uncertainty on the luminosity is not indicated on the points of the cross section, but rather in the text on the figure stating an overall vertical scale uncertainty of 7.7%, dominated by the uncertainty on the BBC cross section.

3.1.2 Longitudinal Spin Asymmetry Formalism

The measured yield for longitudinally polarized beams can be written

$$N^{++} = \epsilon L^{++} \sigma_0 (1 + P_B A_{L,B} + P_Y A_{L,Y} + P_B P_Y A_{LL}), \quad (3.10)$$

$$N^{+-} = \epsilon L^{+-} \sigma_0 (1 + P_B A_{L,B} - P_Y A_{L,Y} - P_B P_Y A_{LL}), \quad (3.11)$$

$$N^{-+} = \epsilon L^{-+} \sigma_0 (1 - P_B A_{L,B} + P_Y A_{L,Y} - P_B P_Y A_{LL}), \quad (3.12)$$

$$N^{--} = \epsilon L^{--} \sigma_0 (1 - P_B A_{L,B} - P_Y A_{L,Y} + P_B P_Y A_{LL}), \quad (3.13)$$

where ϵ is some spin independent efficiency, N^{by} is the number of signal counts for blue beam polarized with helicity $b = \pm 1$ and yellow beam polarized with helicity $y = \pm 1$, σ_0 is the unpolarized cross section, and P_B and P_Y are the polarizations of the blue and yellow beam. These expressions assume the polarizations for the blue beam and yellow beam do not depend on helicity states. Let $L_B^+ = L^{++} + L^{+-}$, $L_B^- = L^{-+} + L^{--}$, and similarly for L_Y . Further, let L define the luminosity summed over all helicity states, $L = L^{++} + L^{--} + L^{+-} + L^{-+}$; L^{like} define the luminosity sum of like-sign helicities $L^{\text{like}} = L^{++} + L^{--}$; and L^{unlike} define the luminosity sum of unlike-sign helicities $L^{\text{unlike}} = L^{+-} + L^{-+}$. One can express linear combinations, $\mathcal{C}_X(N^{by})$, of the π^0 counts relevant for each respective spin asymmetry

$$\mathcal{C}_T(N^{by}) = \sum_a N_a^{++} + N_a^{--} + N_a^{+-} + N_a^{-+} \quad (3.14)$$

$$= \epsilon \sigma_0 \sum_a L_a \left[1 + \frac{L_a^{\text{like}} - L_a^{\text{unlike}}}{L_a} P_{B,a} P_{Y,a} A_{LL} + \frac{L_{B,a}^+ - L_{B,a}^-}{L_a} P_{B,a} A_{L,B} + \frac{L_{Y,a}^+ - L_{Y,a}^-}{L_a} P_{Y,a} A_{L,Y} \right],$$

$$\mathcal{C}_{LL}(N^{by}) = \sum_a N_a^{++} + N_a^{--} - N_a^{+-} - N_a^{-+} \quad (3.15)$$

$$= \epsilon \sigma_0 \sum_a L_a \left[\frac{L_a^{\text{like}} - L_a^{\text{unlike}}}{L_a} + P_{B,a} P_{Y,a} A_{LL} + \frac{L_{Y,a}^+ - L_{Y,a}^-}{L_a} P_{B,a} A_{L,B} + \frac{L_{B,a}^+ - L_{B,a}^-}{L_a} P_{Y,a} A_{L,Y} \right],$$

$$\mathcal{C}_{B,L}(N^{by}) = \sum_a N_a^{++} + N_a^{+-} - N_a^{-+} - N_a^{--} \quad (3.16)$$

$$\begin{aligned} &= \epsilon\sigma_0 \sum_a L_a \left[\frac{L_{B,a}^+ - L_{B,a}^-}{L_a} + P_B A_{L,B} \right. \\ &\quad \left. + \frac{L_a^{\text{like}} - L_a^{\text{unlike}}}{L_a} P_{Y,a} A_{L,Y} + \frac{L_{Y,a}^+ - L_{Y,a}^-}{L_a} P_{B,a} P_{Y,a} A_{LL} \right], \\ \mathcal{C}_{Y,L}(N^{by}) &= \sum_a N_a^{++} - N_a^{+-} + N_a^{-+} - N_a^{--} \quad (3.17) \\ &= \epsilon\sigma_0 \sum_a L_a \left[\frac{L_{Y,a}^+ - L_{Y,a}^-}{L_a} + P_Y A_{L,Y} \right. \\ &\quad \left. + \frac{L_a^{\text{like}} - L_a^{\text{unlike}}}{L_a} P_{B,a} A_{L,B} + \frac{L_{B,a}^+ - L_{B,a}^-}{L_a} P_{B,a} P_{Y,a} A_{LL} \right], \end{aligned}$$

where the sum over a is the sum over runs.

Generally, terms coupling luminosity asymmetries to physical asymmetries are negligible. Specifically, terms of the form

$$\frac{\Delta L}{L} \times P \times A_L \quad (3.18)$$

couple luminosity asymmetries with the parity-violating single-spin asymmetry, A_L , which is expected to be quite small. The luminosity asymmetries, themselves, are quite small from the ability of RHIC to alternate spin directions for successive bunch patterns using a complex 8-bunch polarization pattern. Thus, such terms are safely considered negligible. Furthermore, terms of the form

$$\frac{\Delta L}{L} \times P_B P_Y \times A_{LL}, \quad (3.19)$$

again, couple luminosity asymmetries to A_{LL} which is expected to be no more than a few percent. Again, such terms are safely negligible.

Applying the approximations and defining

$$\mathcal{C}_T(L^{by}) = \sum_a L_a, \quad (3.20)$$

$$\mathcal{C}_T(L^{by} P_B P_Y) = \sum_a L_a P_{B,a} P_{Y,a}, \quad (3.21)$$

$$\mathcal{C}_{LL}(L^{by}) = \sum_a L_a^{++} + L_a^{--} - L_a^{+-} - L_a^{-+}, \quad (3.22)$$

one can write

$$\frac{\mathcal{C}_{LL}(N^{by})}{\mathcal{C}_T(N^{by})} = \frac{\mathcal{C}_{LL}(L^{by}) + \mathcal{C}_T(L^{by} P_B P_Y) A_{LL}}{\mathcal{C}_T(L^{by})}, \quad (3.23)$$

resulting in the solution

$$A_{LL} = \frac{\mathcal{C}_T(L^{by})}{\mathcal{C}_T(L^{by} P_B P_Y)} \left(\frac{\mathcal{C}_{LL}(N^{by})}{\mathcal{C}_T(N^{by})} - \frac{\mathcal{C}_{LL}(L^{by})}{\mathcal{C}_T(L^{by})} \right). \quad (3.24)$$

This equation can be interpreted as the asymmetry in the counts, minus the asymmetry in the luminosities, scaled by the luminosity weighted polarization. The equations for the single spin asymmetries have identical form,

$$A_{B,L} = \frac{\mathcal{C}_T(L^{by})}{\mathcal{C}_T(L^{by} P_B)} \left(\frac{\mathcal{C}_{B,L}(N^{by})}{\mathcal{C}_T(N^{by})} - \frac{\mathcal{C}_{B,L}(L^{by})}{\mathcal{C}_T(L^{by})} \right), \quad (3.25)$$

$$A_{Y,L} = \frac{\mathcal{C}_T(L^{by})}{\mathcal{C}_T(L^{by} P_Y)} \left(\frac{\mathcal{C}_{Y,L}(N^{by})}{\mathcal{C}_T(N^{by})} - \frac{\mathcal{C}_{Y,L}(L^{by})}{\mathcal{C}_T(L^{by})} \right). \quad (3.26)$$

The uncertainty on the relative luminosity is negligible compared with the uncertainty on the number of π^0 counts. In propagating the uncertainty on the counts to the uncertainty on the asymmetries, we note that the denominator and numerator have correlated uncertainties. The variance on the numerator and denominator are just the sums of the variances of the counts, while the covariance between the numerator and denominator is equal to a linear combination of the variances. The linear combination is the same linear combination that occurs in the numerator of the asymmetry, i.e. $\mathcal{C}_{LL}(\delta^2 N^{by})$ for A_{LL} , $\mathcal{C}_{B,L}(\delta^2 N^{by})$ for blue beam A_L , etc. Specifically,

$$\delta^2 A_{LL} = \left[\frac{\mathcal{C}_T(L^{by})}{\mathcal{C}_T(L^{by} P_B P_Y)} \right]^2 \left\{ \left[\frac{1}{\mathcal{C}_T^2(N^{by})} + \frac{\mathcal{C}_{LL}^2(N^{by})}{\mathcal{C}_T^4(N^{by})} \right] \mathcal{C}_T(\delta^2 N^{by}) - 2 \frac{\mathcal{C}_{LL}(N^{by})}{\mathcal{C}_T^3(N^{by})} \mathcal{C}_{LL}(\delta^2 N^{by}) \right\}. \quad (3.27)$$

and similarly for the single beam asymmetries.

3.1.3 Transverse Spin Asymmetry Formalism

The transverse spin asymmetry introduces an azimuthal angle ϕ . This angle ϕ is defined as the azimuthal angle of the π^0 minus the azimuthal angle of the spin polarization [15].

One can writing the measured yields for for one transversely polarized beam, including the ϕ , as OhlsenKeaton

$$N(\phi) = L \epsilon(\phi) \sigma_0 (1 + P_T A_N \sin(\phi)), \quad (3.28)$$

where P_T is the beam polarization and A_N is the analyzing power. Utilizing the symmetry of the detector, one can consider yields for different spin states in different halves of the detector,

$$N^\uparrow(\phi) = L^\uparrow \epsilon(\phi) \sigma_0 (1 + P_T A_N \sin(\phi)) \quad (3.29)$$

$$N^\downarrow(\phi) = L^\downarrow \epsilon(\phi) \sigma_0 (1 - P_T A_N \sin(\phi)) \quad (3.30)$$

$$\begin{aligned} N^\uparrow(\phi + \pi) &= L^\uparrow \epsilon(\phi + \pi) \sigma_0 (1 + P_T A_N \sin(\phi + \pi)) \\ &= L^\uparrow \epsilon(\phi + \pi) \sigma_0 (1 - P_T A_N \sin(\phi)) \end{aligned} \quad (3.31)$$

$$\begin{aligned} N^\downarrow(\phi + \pi) &= L^\downarrow \epsilon(\phi + \pi) \sigma_0 (1 - P_T A_N \sin(\phi + \pi)) \\ &= L^\downarrow \epsilon(\phi + \pi) \sigma_0 (1 + P_T A_N \sin(\phi)). \end{aligned} \quad (3.32)$$

Note that Equations 3.29 and 3.32 represent the same physics and Equations 3.30 and 3.31 also represent the same physics.

Next, one can combine like physics terms to express the difference and the sum,

$$\sqrt{N^\uparrow(\phi) N^\downarrow(\phi + \pi)} - \sqrt{N^\downarrow(\phi) N^\uparrow(\phi + \pi)} = 2 \sqrt{L^\uparrow \epsilon(\phi) L^\downarrow \epsilon(\phi + \pi) \sigma_0 P_T A_N \sin(\phi)} \quad (3.33)$$

$$\sqrt{N^\uparrow(\phi) N^\downarrow(\phi + \pi)} + \sqrt{N^\downarrow(\phi) N^\uparrow(\phi + \pi)} = 2 \sqrt{L^\uparrow \epsilon(\phi) L^\downarrow \epsilon(\phi + \pi) \sigma_0} \quad (3.34)$$

$$(3.35)$$

Define the ratio of Equations 3.33 and 3.34, scaled by the inverse polarization, as

$$\mathcal{A}_N(\phi) = \frac{1}{P_T} \frac{\sqrt{N^\uparrow(\phi) N^\downarrow(\phi + \pi)} - \sqrt{N^\downarrow(\phi) N^\uparrow(\phi + \pi)}}{\sqrt{N^\uparrow(\phi) N^\downarrow(\phi + \pi)} + \sqrt{N^\downarrow(\phi) N^\uparrow(\phi + \pi)}}. \quad (3.36)$$

Ideally, one then has

$$\mathcal{A}_N(\phi) = A_N \sin(\phi) \quad (3.37)$$

Thus, A_N can be extracted without explicitly using the relative luminosity. The variance on $\mathcal{A}_N(\phi)$ for a given ϕ bin can be expressed

$$\begin{aligned} (\delta A_N)^2 &= \frac{1}{P_T} \frac{(N(\phi + \pi)^\downarrow + N(\phi)^\uparrow) (N(\phi + \pi)^\uparrow N(\phi)^\downarrow)}{\left[\sqrt{N(\phi)^\uparrow N(\phi + \pi)^\downarrow} + \sqrt{N(\phi + \pi)^\uparrow N(\phi)^\downarrow} \right]^4} \\ &+ \frac{1}{P_T} \frac{(N(\phi + \pi)^\uparrow + N(\phi)^\downarrow) (N(\phi + \pi)^\downarrow N(\phi)^\uparrow)}{\left[\sqrt{N(\phi)^\uparrow N(\phi + \pi)^\downarrow} + \sqrt{N(\phi + \pi)^\uparrow N(\phi)^\downarrow} \right]^4}. \end{aligned} \quad (3.38)$$

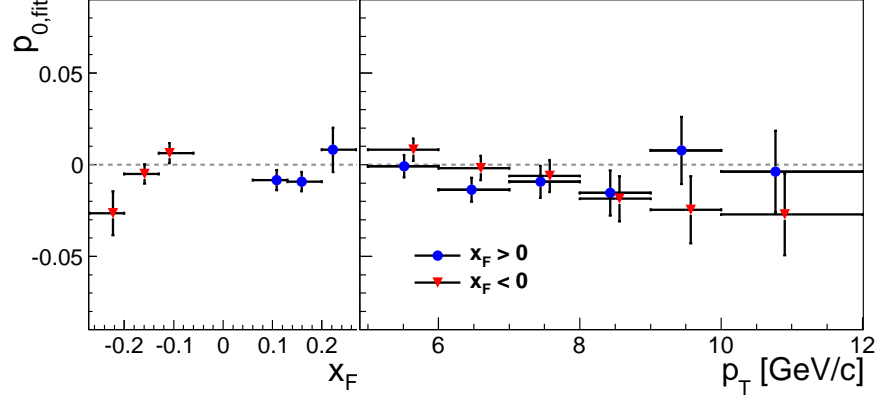


Figure 3.2: The physics, instrumental, and luminosity asymmetries for the $5 < p_T < 6$ GeV/c bin, including the fit value for p_0 and $\varepsilon = p_1$.

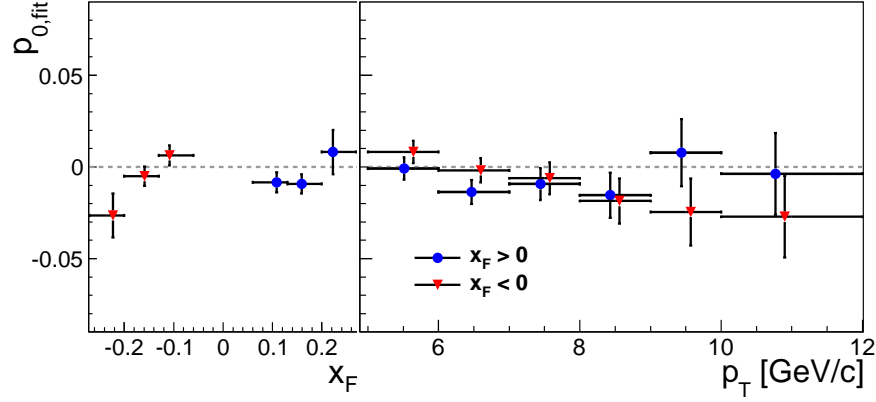


Figure 3.3: The p_0 values from the A_N fits.

Note, this is the same form as described in Ref. [16].

In practise, not all assumptions hold perfectly, and $\mathcal{A}_N(\phi)$ can have offsets and higher harmonics than just the sine modulation. We also correct for polarization after computing the asymmetry. Thus, we compute

$$\mathcal{E}(\phi) = \frac{\sqrt{N^\uparrow(\phi) N^\downarrow(\phi + \pi)} - \sqrt{N^\downarrow(\phi) N^\uparrow(\phi + \pi)}}{\sqrt{N^\uparrow(\phi) N^\downarrow(\phi + \pi)} + \sqrt{N^\downarrow(\phi) N^\uparrow(\phi + \pi)}}, \quad (3.39)$$

and then fit \mathcal{E} to the functional form

$$\mathcal{E}(\phi) = p_0 + p_1 \sin(\phi). \quad (3.40)$$

The fit parameter p_1 is often denoted ε or the raw asymmetry. This quantity ε is then corrected for polarization and the background asymmetry. The value of p_0 serves as an indication for how well the assumptions in the formalism hold. As a typical bin, the physics, instrumental, and luminosity asymmetries for the $5 < p_T < 6$ GeV/c bin are shown in Figure 3.2. The p_0 values for all of the fits versus x_F and p_T are shown in Figure 3.3.

3.1.4 Combining Monte Carlo Runs

The Pythia Monte Carlo production used for this analysis [14] have a number of runs in various partonic p_T bins; see Table 3.1. Let $n_{a,j}$ be the number of Pythia events generated (before filtering) for partonic p_T

Partonic p_T Bin	Luminosity
4 to 6	0.8 pb ⁻¹
6 to 9	0.8 pb ⁻¹
6 to 15	0.9 pb ⁻¹
15 to 35	1.1 pb ⁻¹

Table 3.1: Table of generated luminosities per partonic p_T bin for the official Pythia sample [14].

bin a and run j . Let $\sigma_{a,j}$ be the reported cross section, also for run j bin a . To use the full Monte Carlo production, one must both combine runs within and across partonic p_T bins. One would like to estimate the number of π^0 candidates, per π^0 p_T bin per unit luminosity. The absolute normalization of the Monte Carlo is never used, and so it is just as well to leave the normalization as for a single unit of luminosity.

Let $N_{a,i,j}$ be the number of generated π^0 s within a π^0 p_T bin i from run j of partonic p_T bin a . One would like to combine the runs such that one has a minimally biased estimate for Y_i , the number of generated π^0 s in π^0 p_T bin i per unit luminosity.

Within a partonic p_T bin, the reported cross sections $\sigma_{a,j}$ should be almost identical (for various j), and represent estimates of the integral. These integral estimates can be thought of as an average value, with the number of samples being $n_{a,j}$. Thus to compute σ_a , the cross section for all runs in the p_T bin, one must use the weighted average

$$\sigma_a = \frac{\sum_j n_{a,j} \sigma_{a,j}}{\sum_j n_{a,j}} \quad (3.41)$$

However, to combine the number of trials and the number of π^0 counts, one can simply add over the runs,

$$n_a = \sum_j n_{a,j}, \quad (3.42)$$

$$N_{a,i} = \sum_j N_{a,i,j}. \quad (3.43)$$

The final result for Y_i is

$$Y_i = \sum_a \frac{N_{a,i}}{n_a} \sigma_a. \quad (3.44)$$

and the variance is

$$\delta^2 Y_i = \sum_a \frac{N_{a,i}}{n_a^2} \sigma_a^2. \quad (3.45)$$

One can interpret each element of the sum in Equation 3.44 as the number of π^0 candidates divided by the effective luminosity, or the effective branching ratio to π^0 s times the cross section (for independent cross sections).

Equation 3.44 can be re-expressed in terms of the more fundamental quantities as

$$Y_i = \sum_a \frac{\sum_j N_{a,i,j}}{\left(\sum_j n_{a,j}\right)^2} \sum_j n_{a,j} \sigma_{a,j}. \quad (3.46)$$

Note: Equation 3.44 is used in several circumstances, and each case may have different cuts or be from various productions.

3.2 Background Subtraction

To determine the signal fraction, the invariant mass distribution in data is fit to a linear combination of a template functions. The template functions include the a signal shape function and two background shape functions. Three options for the templates have been considered: 1) a histogram method, where the

histograms from the Monte Carlo data are used directly, 2) a function method, where the histograms are fit to functional forms, or 3) a hybrid method where functional forms are used for the backgrounds and a histogram is used for the data.

Note: the cuts on the reconstructed candidates in Monte Carlo are identical to those used in data. Recall, the emulated trigger is used for both data and Monte Carlo.

3.2.1 Definition of Signal and Background(s) in Monte Carlo

Signal A reconstructed photon pair is associated with the π^0 signal if $\Delta R < 0.04$ in η, ϕ space between the momentum direction of the reconstructed pair and generated π^0 is less than 0.04.

Conversion Background Similarly, a reconstructed photon pair is associated with the conversion background if $\Delta R < 0.04$ between the momentum direction of the reconstructed pair and a generated, decayed photon.

Other background Photon pairs that are not identified as signal or conversion background are identified as other background. This includes combinatorial background, and well as backgrounds to due other reconstruction issues and/or interplay between conversions, combinatorics, and reconstruction.

3.2.2 Template Details

Whether each template is a functional form or a histogram, several basic operations must be available.

- Must be able to evaluate the value and uncertainty for any given point.
- Must be able to evaluate the derivative for any given point.
- Must be able to compute an integral between any two points.

Each template is normalized over the fit range, and then scaled by the number of data points within the fit range divided by the bin width of the data histogram. For the histogram templates, an additional factor of the bin width of the template histogram is included. In the software, the template normalization factor and the bin factors are all considered a property of the template. In the presentation in this note, the bin factors will be assumed to be part of the template (and thus not explicitly noted), but the normalization factor will be considered separate from the template and explicitly included in Section 3.2.3.

Histograms Forms

To evaluate a the histogram at any point, we use linear interpolation, as provided in ROOT via `TH1::Interpolate`. The uncertainty at any point is set to the uncertainty of the bin that the point falls in. We use a simple numeric estimate of the derivative by evaluating ± 0.1 times the bin width, and setting the derivative equal to the difference over ± 0.2 times the bin width. As the function is piecewise linear (due to the linear interpolation), this simple estimate of the derivative is sufficiently accurate.

In order for the integral to account for the partial bins, we do a simple Riemann integral, with 499 points evenly spaced between the end points, and also include evaluating at the end points. Specifically, if $f(x)$ is the function equal to linearly interpolating the histogram, $\delta^2 f(x)$ is the variance at point x , and $w(x)$ is the bin width at point x , the integral between x_1 and x_{501} and its variance is

$$I = \frac{x_{500} - x_1}{501} \sum_{i=1}^{500} \frac{f(x_i)}{w(x_i)} \quad (3.47)$$

$$\delta^2 I = \frac{x_{500} - x_1}{501} \sum_{i=1}^{500} \frac{\delta^2 f(x_i)}{w(x_i)}. \quad (3.48)$$

Functional Forms

Let the template functions (i.e. functional forms) be enumerated as $\{f_i(M_{\gamma\gamma})\}_{i=1}^3$. Specifically, let $f_1(M_{\gamma\gamma})$ be the signal template function, $f_2(M_{\gamma\gamma})$ the conversion background template function, and $f_3(M_{\gamma\gamma})$ the other background template function.

The shape of the signal is chosen to be the sum of two skewed Gaussian distributions, with one mean limited to near the π^0 peak $0.12 < M_{\gamma\gamma} < 0.18 \text{ GeV}/c^2$ and the other mean limited to less than the PDG π^0 peak mass, $0.00 < M_{\gamma\gamma} < 0.135 \text{ GeV}/c^2$. Note: for $p_T > 9 \text{ GeV}/c^2$, only a single skewed Gaussian is used.

The conversion background shape and other background shape are also chosen to be a skewed Gaussian. While the conversion background looks like a skewed Gaussian, the choice of this shape for the other background is not so obvious. However, in studies this shape was found to represent the histogram fairly well and can effectively model the shape at the low mass turn-on region. The functions can be written:

$$f_1(M_{\gamma\gamma}; \boldsymbol{\theta}_1) = C_1 \mathcal{N}(\mu_1, \sigma_1 + (\tau_1 - \mu_1)M_{\gamma\gamma}) + C'_1 \mathcal{N}(\mu_1, \sigma'_1 + (\tau'_1 - \mu_1)M_{\gamma\gamma}) \Bigg], \quad (3.49)$$

$$f_2(M_{\gamma\gamma}; \boldsymbol{\theta}_2) = C_2 \mathcal{N}(\mu_2, \sigma_2 + (\tau_2 - \mu_2)M_{\gamma\gamma}), \quad (3.50)$$

$$f_3(M_{\gamma\gamma}; \boldsymbol{\theta}_3) = a_0 + a_1 M_{\gamma\gamma} + a_2 M_{\gamma\gamma}^2 + a_3 M_{\gamma\gamma}^3, \quad (3.51)$$

with the fit parameters being

$$\boldsymbol{\theta}_1 = [C_1, \mu_1, \sigma_1, \tau_1, \epsilon_1, \sigma'_1, \tau'_1], \quad (3.52)$$

$$\boldsymbol{\theta}_2 = [C_2, \mu_2, \sigma_2, \tau_2], \quad (3.53)$$

$$\boldsymbol{\theta}_3 = [a_0, a_1, a_2, a_3]. \quad (3.54)$$

The signal function parameters are initialized with C_1 set to the maximum value of the histogram, μ_1 set to the $M_{\gamma\gamma}$ position of the maximum bin, $\sigma_1 = 0.02 \text{ GeV}/c^2$, $\tau_1 = 0$, C'_1 set to the bin height at $M_{\gamma\gamma} = 0.05 \text{ GeV}/c^2$, $\mu'_1 = 0.07 \text{ GeV}/c^2$, $\sigma'_1 = 0.04$, and $\tau'_1 = 0.4$. The conversion background function parameters are initialized with C_2 set to the maximum value of the histogram, μ_2 set to the average of the $M_{\gamma\gamma}$ position of the maximum bin and the mean $M_{\gamma\gamma}$ position over the histogram range ($0 < M_{\gamma\gamma} < 0.6 \text{ GeV}/c^2$), σ_1 set to half of the histogram RMS, and $\tau_2 = 0$. The other background function parameters are initialized with C_3 set to the maximum value of the histogram, $\mu_3 = 0.07 \text{ GeV}/c^2$, $\sigma_3 = 0.035 \text{ GeV}/c^2$, and $\tau_2 = 0.7$.

The functions are fit to the template histograms using ROOT's `TH1::Fit`. The fits are performed using ROOT v5.30, which seems to have more stable default fitting routines than ROOT v5.22 (the default version on BNL RCF nodes). The fit range for these fits are the same as the fit range for the fit of the data to the templates, nominally 0.0 to 0.3 GeV/c^2 .

The reduced χ^2 values for the template fits are given in Figure 3.4. The fits are generally quite good. Recall a 1.5σ difference causes a χ^2/ndf of 2.25. The individual histograms and the results for the fits are given in Figure 3.5 (signal), Figure 3.6 (conversion background), and Figure 3.7 (other background).

The value of the function at any point can be evaluated using `TF1::Eval`. The variance at any $x = M_{\gamma\gamma}$ point is

$$\delta^2 f(x; \boldsymbol{\theta}) = \sum_{i,j} \frac{\partial f(x)}{\partial \theta_i} \text{Cov}(\theta_i, \theta_j) \frac{\partial f(x)}{\partial \theta_j}. \quad (3.55)$$

The derivative with respect to $M_{\gamma\gamma}$ can be evaluated with `TF1::Derivative` and the derivatives with respect to the parameters can be evaluated with `TF1::GradientPar`. The integral is computed with `TF1::Integral` and the uncertainty on the integral due to the variance and covariance on the parameters is computed using `TF1::IntegralError`.

3.2.3 The Combined Fit

The combined fit function $f_T(M_{\gamma\gamma})$ is defined as the weighted sum of the normalized templates, with a scale factor to allow for differences in the energy scale between data and Monte Carlo. For more information regarding causes of this energy scale difference, see Section 4f in Part I of this analysis note, entitled ‘‘Studies of the Sampling Fraction’’.

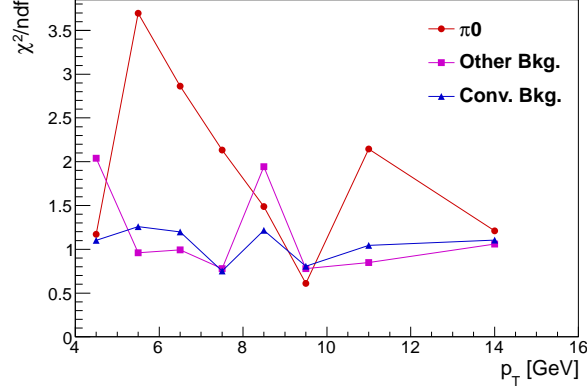


Figure 3.4: Reduced χ^2 values, per p_T bin, for fitting the template functions to the Monte Carlo histograms.

As we will later consider the effect of varying the fit and peak range, we will use the notation of $[M_{\gamma\gamma,1}, M_{\gamma\gamma,4}]$ to indicate the fit region and $[M_{\gamma\gamma,2}, M_{\gamma\gamma,3}]$ to indicate the peak region. Let $f_i(M_{\gamma\gamma}) \pm \delta f_i(M_{\gamma\gamma})$ denote the template value and uncertainty for template i . As previously noted, each template is divided by the integral over the fit range,

$$F_i = \int_{0.0 \text{ GeV}/c^2}^{0.3 \text{ GeV}/c^2} dM_{\gamma\gamma} f_i(M_{\gamma\gamma}), \quad (3.56)$$

and combined function is also multiplied by the number of counts in the data histogram within the mass fit range so that the sum of the weights is near one. At first, `TF1::Fit` was used to fit the scaled linear combination of the templates to the data histogram. However, this procedure does not use the uncertainty on the templates to determine the minimum position nor the uncertainty on the parameters.

Instead, a χ^2 method was implemented, with

$$\chi^2 = \sum_i \frac{h_i^D - \sum_i \frac{w_i}{F_i} f_i(x_i/\alpha)}{\delta^2 h_i^D - \sum_i \frac{w_i^2}{F_i^2} \delta^2 f_i(x_i/\alpha)}, \quad (3.57)$$

where h_i^D is the data histogram value for point i , $\delta^2 h_i^D$ is the data histogram variance for point i , and x_i is the bin center of bin i .

All bins overlapping in the fit range are included in the sum. A `ROOT::Math::Minimizer` object is used to find the minimum χ^2 value. `MIGRAD` as provided in `Minuit` is used when all templates are functional forms. However, the piece-wise linear extrapolation used in evaluating the histogram templates causes difficulties for derivative based minimization techniques, such as `MIGRAD`, and thus the simplex algorithm is used if any of the templates are histograms.

3.2.4 Histogram versus Functional Templates

The combinations of template types have been considered,

- Function: functional forms used for all three templates.
- Histogram: histograms used for all three templates.
- Hybrid: histogram used for the signal template (as it has a more complex shape and higher MC statistics) and functional forms used for the backgrounds (as the MC statistics are low).

In the limit of infinite Monte Carlo statistics and a perfect functional form, the three options would give identical results. However, the functional form adds in the information that the shape is smoothly varying,

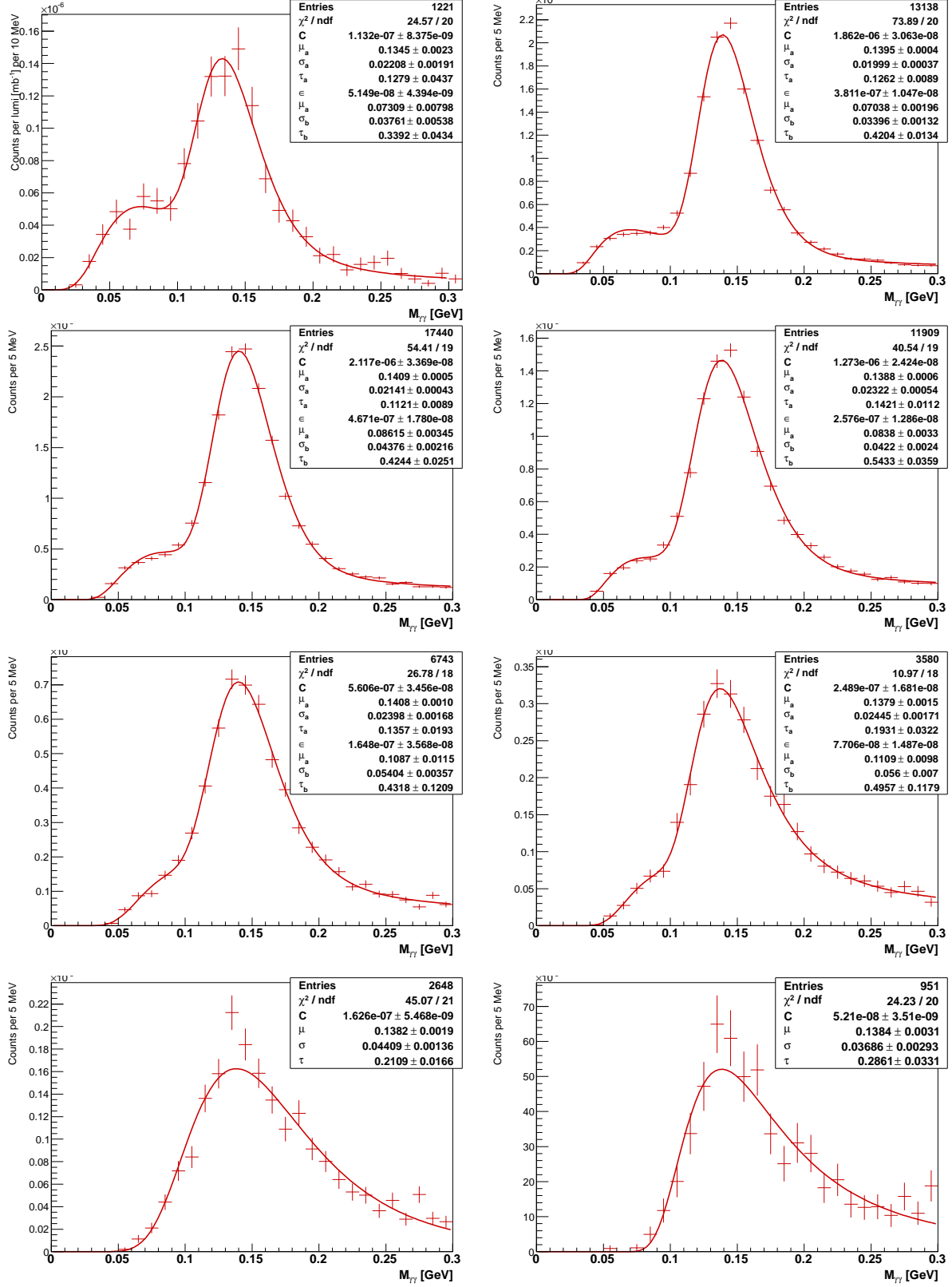


Figure 3.5: Signal shape fits: plot of the Monte Carlo data (data points with error bars) superimposed with the result for the template shapes (colored line). Plots are shown for each p_T bin, with the upper left being 4-5 GeV/c, upper right 5-6 GeV/c, second row left 6-7 GeV/c, and so forth.

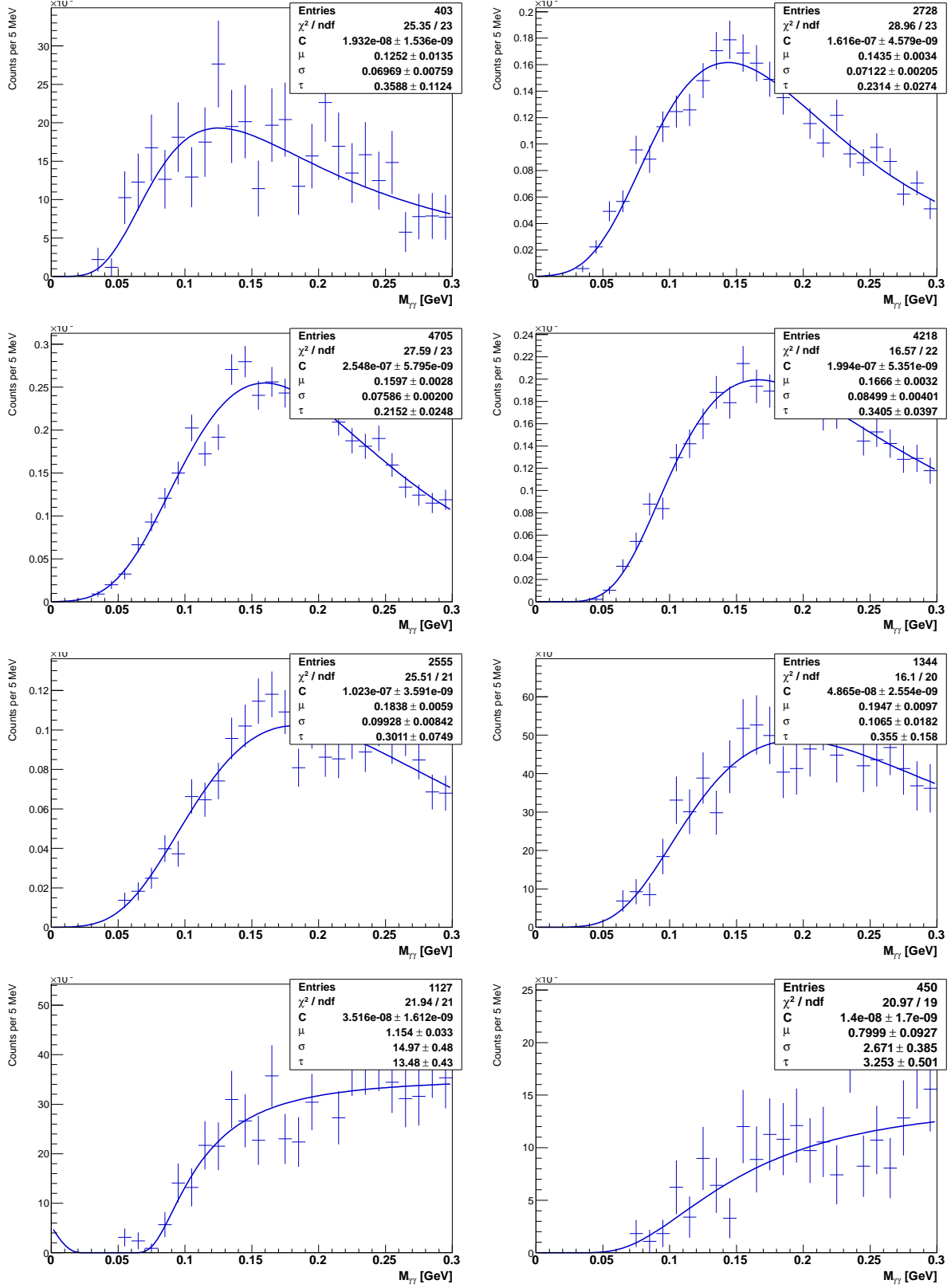


Figure 3.6: Conversion background shape fits: plot of the Monte Carlo data (black histogram) superimposed with the result for the template shapes (colored line). Panels are arranged as in Figure 3.5.

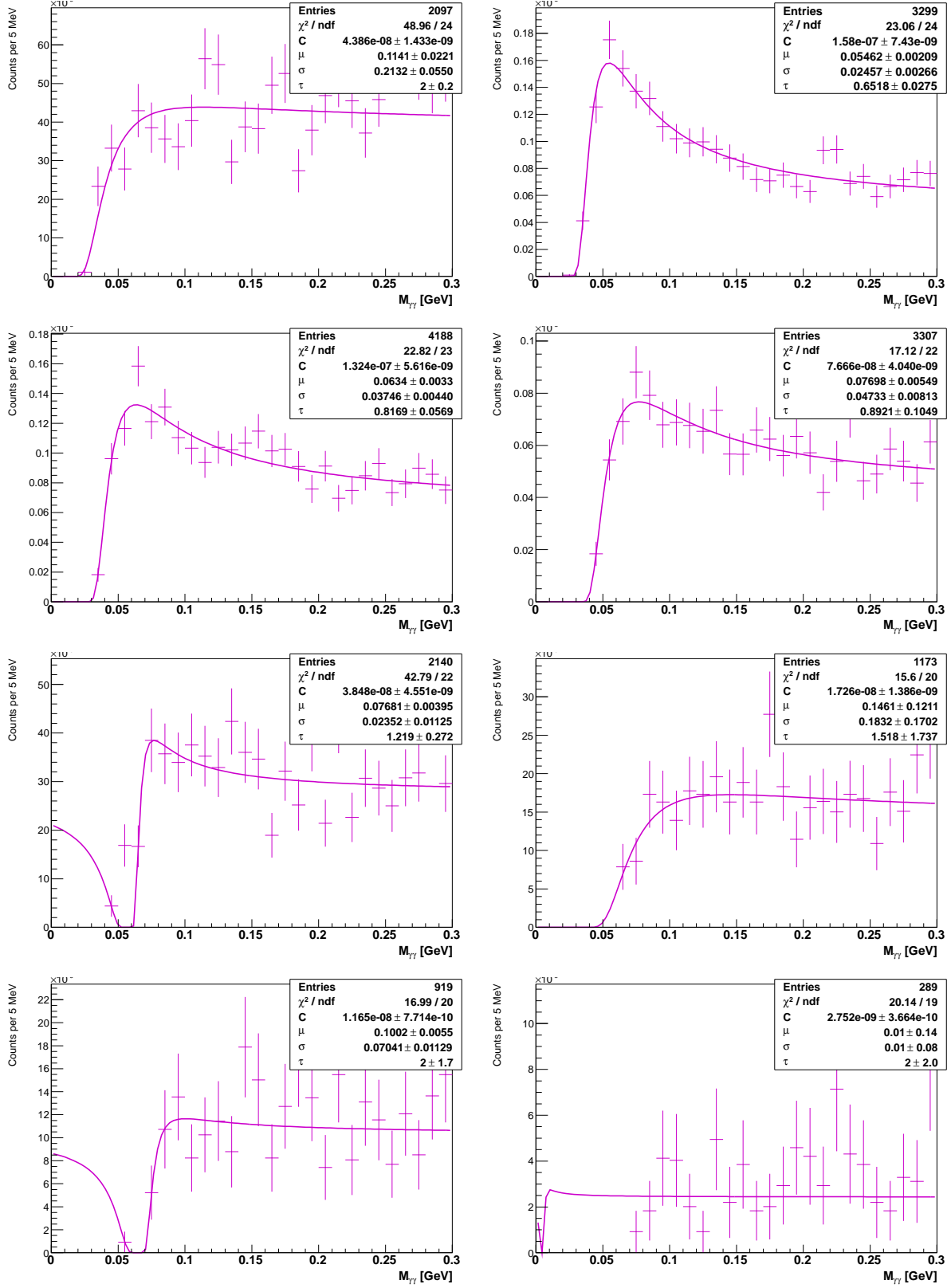


Figure 3.7: Other background shape fits: plot of the Monte Carlo data (black histogram) superimposed with the result for the template shapes (colored line). Panels are arranged as in Figure 3.5.

and thus makes the result less sensitive to the noise due to limited Monte Carlo statistics. Thus the functional forms could increase the accuracy and precision. In contrast, the functional forms may not exactly match the template shapes in data, and which would deteriorate the accuracy and precision.

Plots including the data and the templates, scaled according to the fit results, are provided in Figures 3.8, 3.9, and 3.10, for the functional, histogram, and hybrid options. Note, the uncertainties on the templates are included in the plots, but the uncertainties on the fitted weights and α are not. Some differences can be seen in some p_T bins, particularly in relative amounts of the conversion vs. other backgrounds, though some bins, such as $7 < p_T < 8$ GeV/ c , are nearly identical for the three options.

The weights and α values for the three options are compared in Figure 3.11. The central value of the signal fraction is quite consistent across the three options. This suggests that the choice of functional forms is sufficiently accurate. Due to the limited Monte Carlo statistics, the uncertainties on the signal fraction is generally lower for the functional option than the other options.

As the functional form option gives similar central values as the other options, with lower uncertainties across most of the p_T bins, this method is used for the final results and further analysis. The histogram and hybrid options are not used for any other studies.

3.2.5 Fit Results

The plots for the polarized data sets corresponding to Figure 3.8 for the full data set are given in Figures 3.13 (longitudinal), 3.14 (transverse vs. p_T), and 3.15 (transverse vs. x_F). The results are quite consistent between the two data samples and the combined sample. Note the full sample contains all of the transverse and longitudinal data samples, as well as a few additional runs in which the polarization was poor or unmeasured.

Figure 3.16 shows the results of the weights and the α factor coming directly from the fit. Again, the results are consistent across the data samples.

Since the π^0 peak position does not come directly from the fit, the peak position is found by finding the maximum point on the signal fraction template function, scaling by α . The uncertainty is determined by fitting a Gaussian function to the histogram, and taking the uncertainty on the mean scaled by α . The value of the π^0 peak position does not directly influence the results, but is an indication of how well the entire calibration, reconstruction, and background subtraction procedures are functioning. The resulting peak positions are shown in Figure 3.17. The peak position is highly correlated with the α value from the fit.

3.2.6 Computing the Number of Signal Counts

Determining the Signal Fraction

From the fit procedure, one has weights w_i with covariance matrix $\text{Cov}(w_i, w_j)$. Although the templates were fit over a large region (nominally 0.0 to 0.3 GeV/ c^2 , see Section 3.2.3), only the number of π^0 signal counts in the peak region (nominally 0.1 to 0.2 GeV/ c^2) are used for the main results. As we will later consider the effect of varying the fit and peak range, we will use the notation of $[M_{\gamma\gamma,1}, M_{\gamma\gamma,4}]$ to indicate the fit region and $[M_{\gamma\gamma,2}, M_{\gamma\gamma,3}]$ to indicate the peak region.

The relative fractions of the signal and backgrounds in the peak can be written as

$$w_i^{(P)} = \frac{w_i R_i}{\sum_k w_k R_k}, \quad (3.58)$$

with R_i the ratio of the integrals in the peak region vs. over the fit region,

$$R_i = \frac{1}{F_i} \int_{M_{\gamma\gamma,2}}^{M_{\gamma\gamma,3}} dM_{\gamma\gamma} f_i(M_{\gamma\gamma}/\alpha), \quad (3.59)$$

$$= \frac{\alpha}{F_i} \int_{M_{\gamma\gamma,2}/\alpha}^{M_{\gamma\gamma,3}/\alpha} dM_{\gamma\gamma} f_i(M_{\gamma\gamma}). \quad (3.60)$$

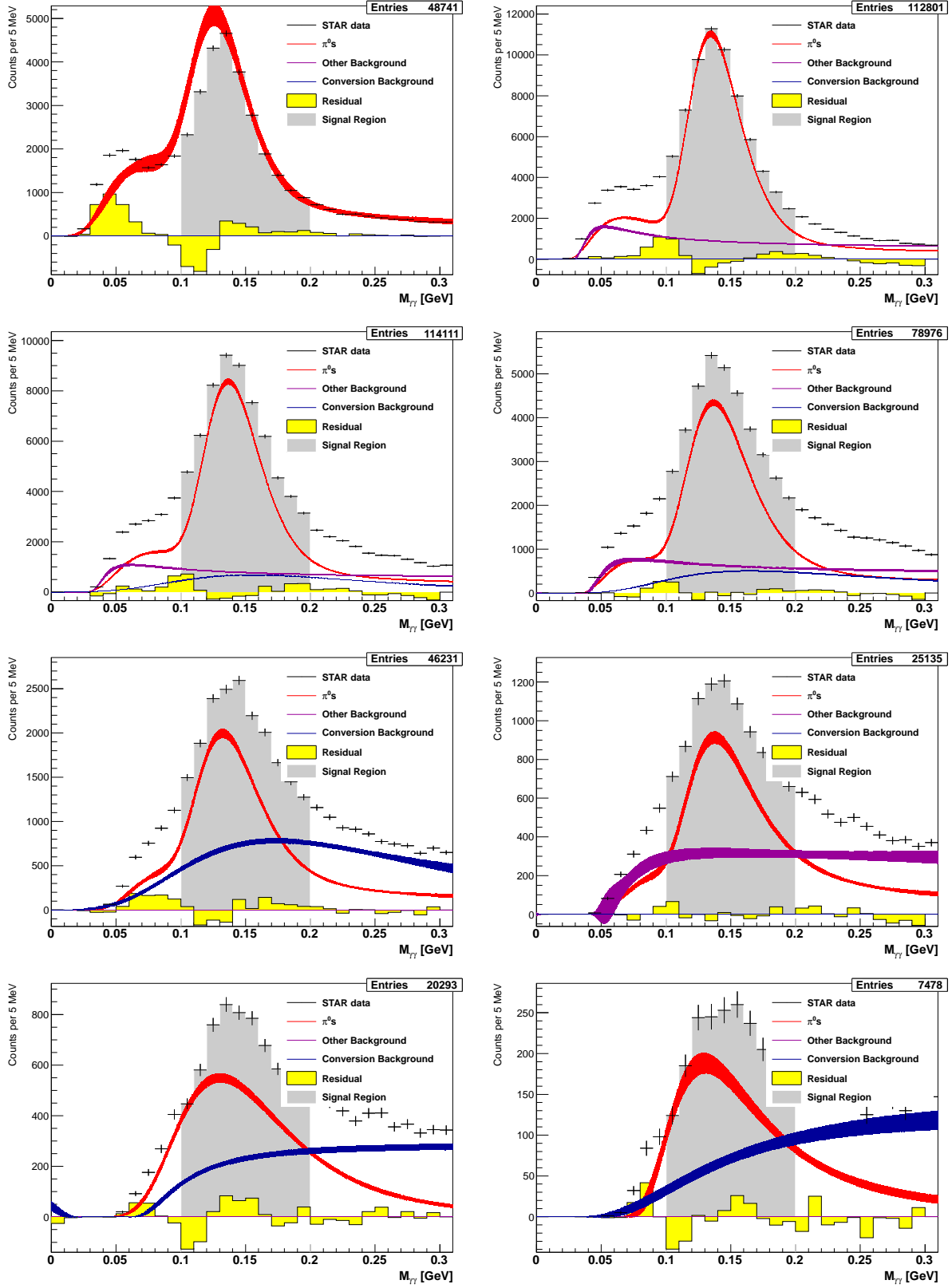


Figure 3.8: Fit results per p_T bin using function templates. Panels are arranged as in Figure 3.5.

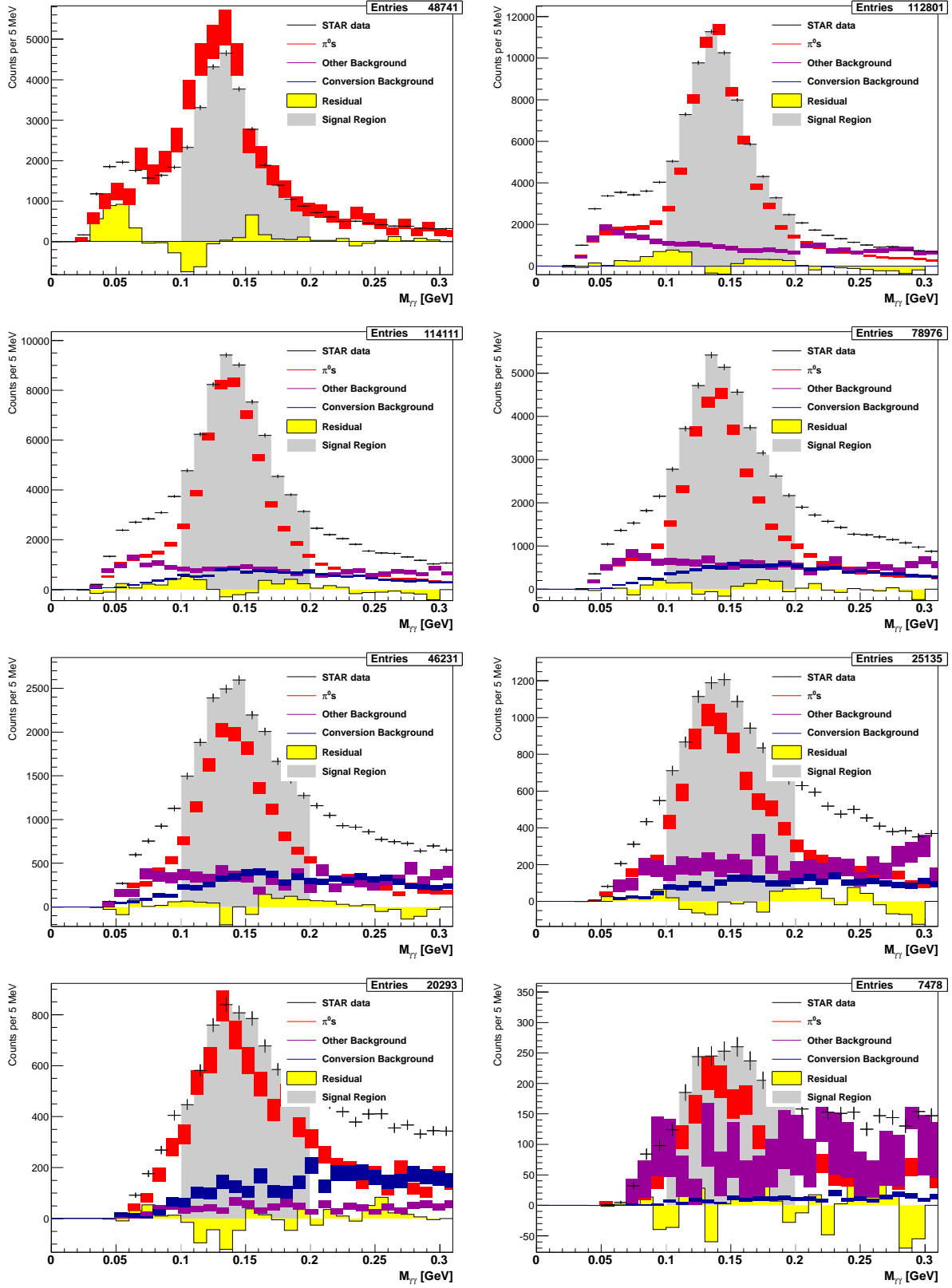


Figure 3.9: Fit results per p_T bin using histogram templates. Panels are arranged as in Figure 3.5.

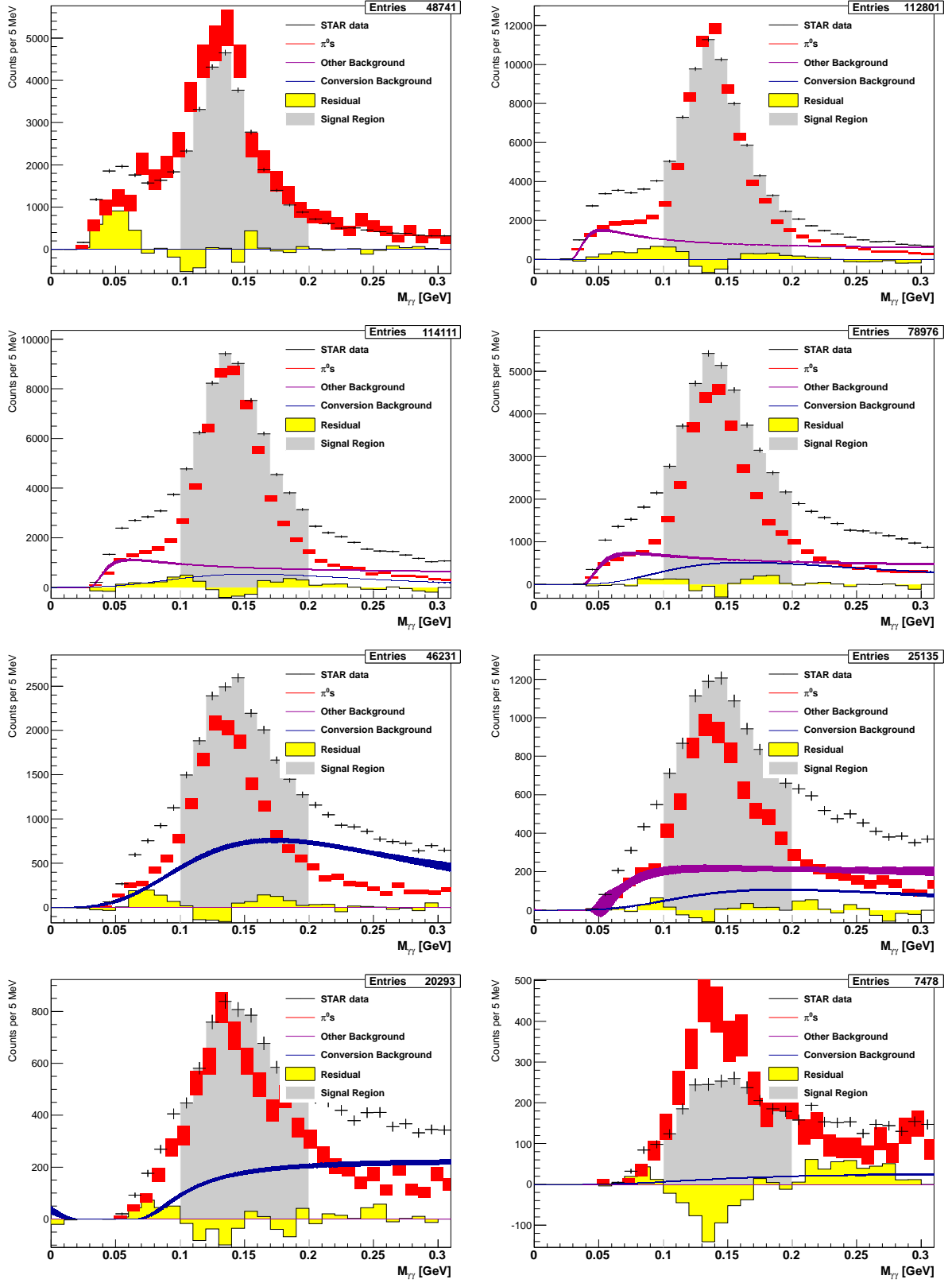


Figure 3.10: Fit results per p_T bin using hybrid template option. Panels are arranged as in Figure 3.5.

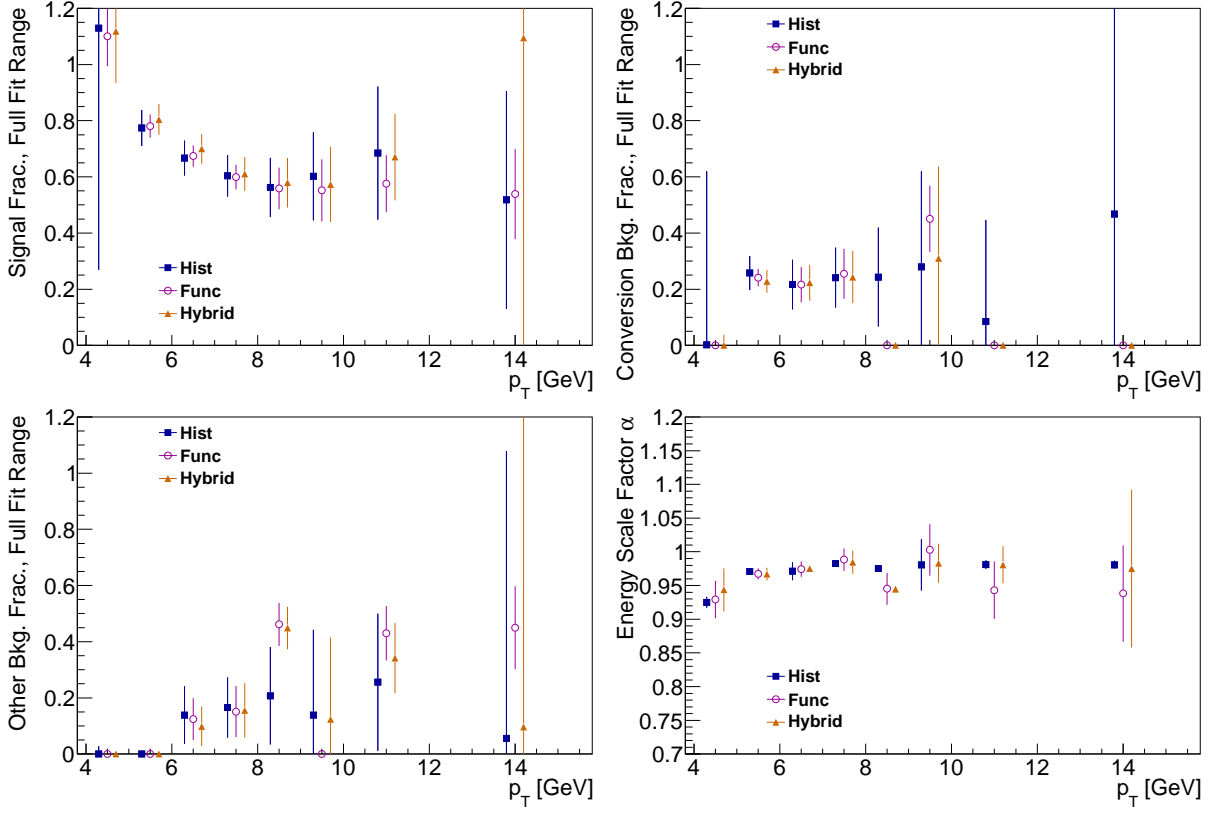


Figure 3.11: Comparison of the parameters from the combined fit for the three template options. Upper left panel is w_1 (signal fraction), upper right is w_2 (conversion background fraction), lower left is w_3 (other background fraction), and lower right is the energy scale factor α .

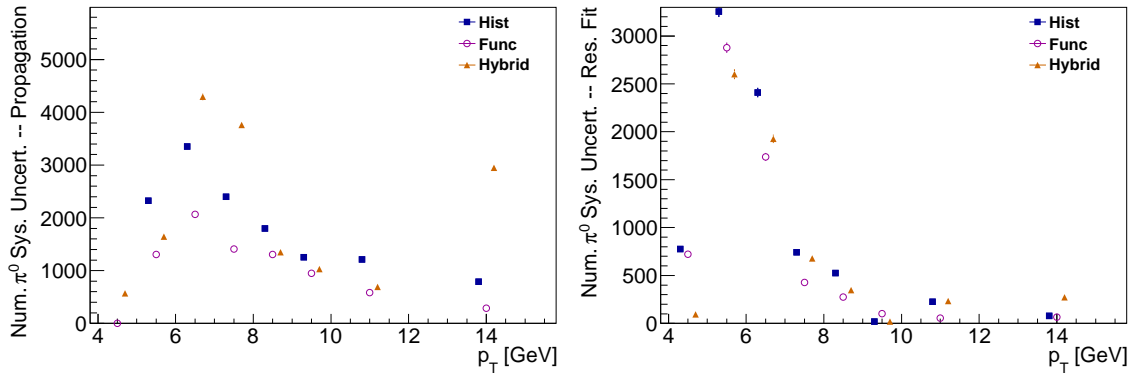


Figure 3.12: Systematic uncertainties on the number of π^0 counts in the peak region for the cross section data set, computed for each of the three options: histogram (blue squares), function (magenta circles), and hybrid (orange triangles). Left panel: the uncertainty due to the signal fraction in the peak; right panel: the uncertainty due to the fit of the residual.

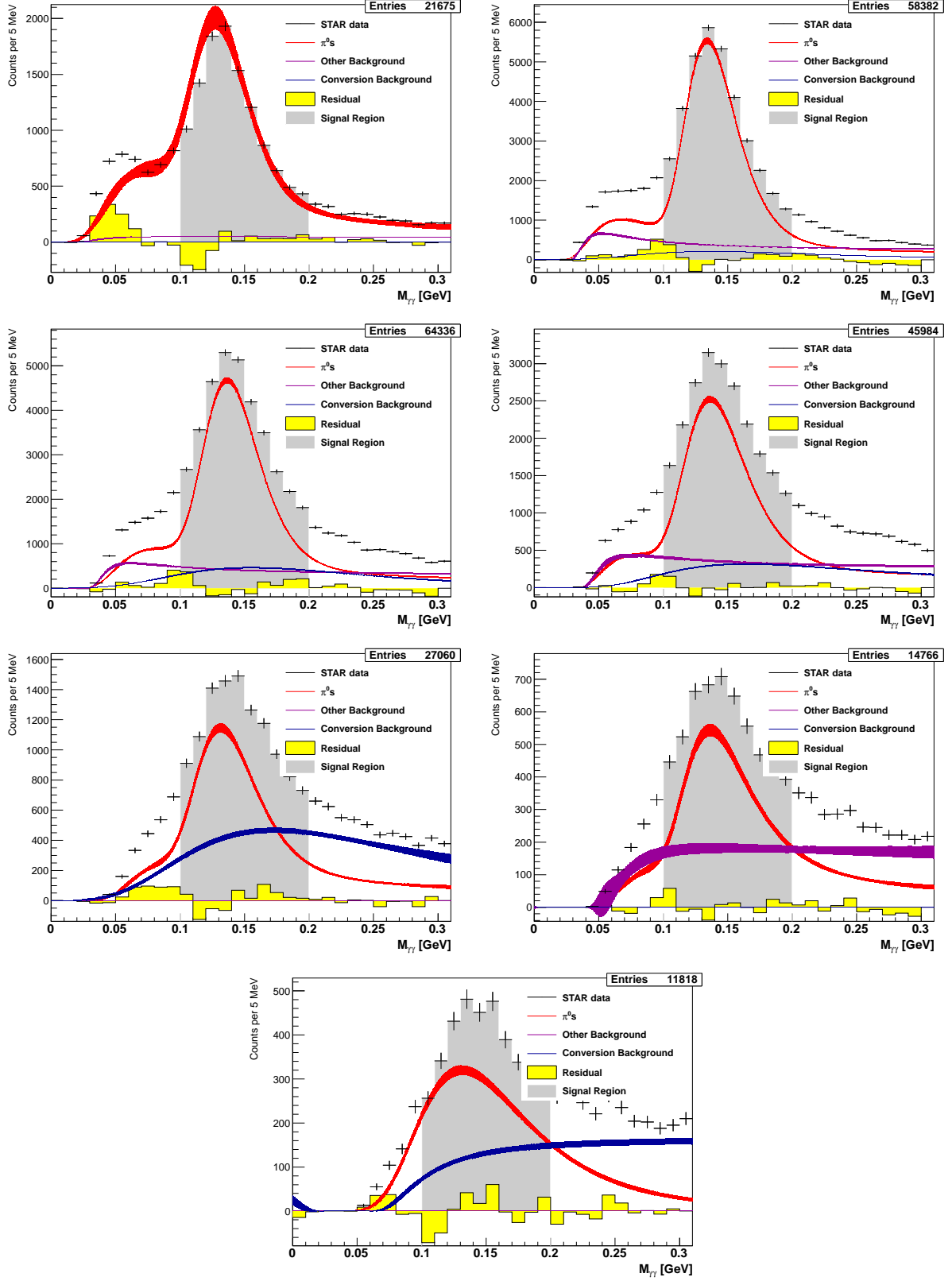


Figure 3.13: Fit results per p_T bin using function templates for the longitudinal data set. Panels are arranged as in Figure 3.5, with the exception of the highest p_T bin not being shown.

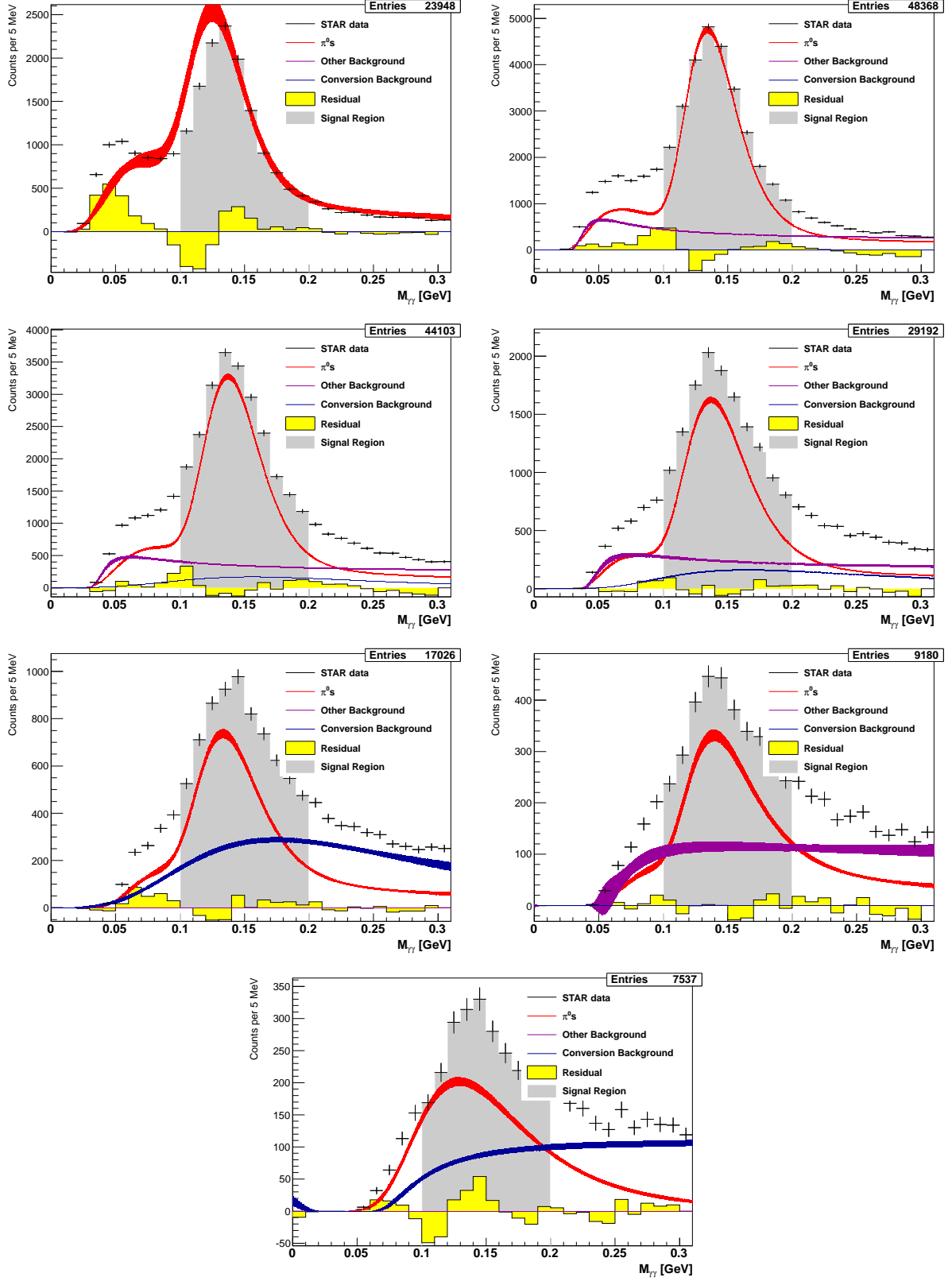


Figure 3.14: Fit results per p_T bin using function templates for the transverse data set. Panels are arranged as in Figure 3.5, with the exception of the highest p_T bin not being shown.

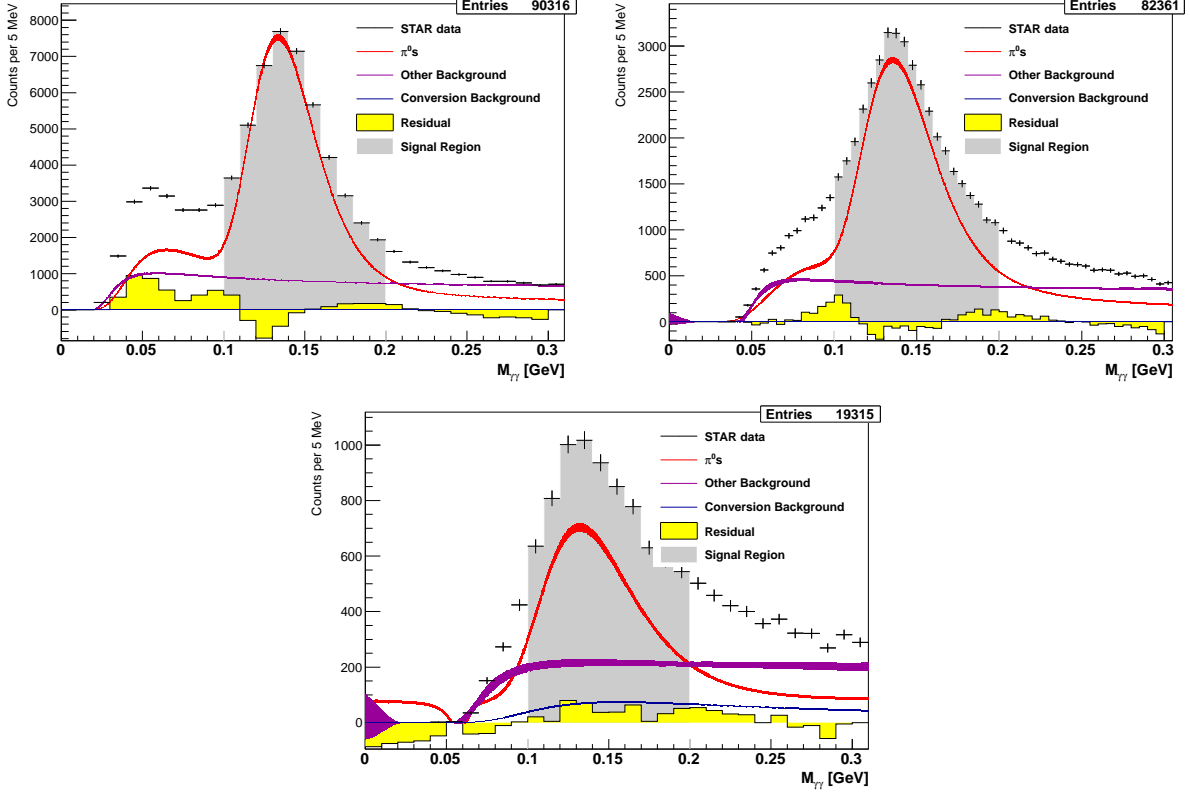


Figure 3.15: Fit results per x_F bin using function templates for the transverse data set. Upper left first x_F bin, upper right, second x_F bin, and lower panel, third x_F bin.

The quantities F_i are the integrals used to normalize the templates, discussed in Section 3.2.2. For convenience, define

$$I_i = \int_{M_{\gamma\gamma,2/\alpha}}^{M_{\gamma\gamma,3/\alpha}} dM_{\gamma\gamma} f_i(M_{\gamma\gamma}), \quad (3.61)$$

$$R'_i = \frac{I_i}{F_i}, \quad (3.62)$$

so that

$$R_i = \alpha R'_i(\alpha). \quad (3.63)$$

Uncertainty on Integral Ratio

Using standard propagation of uncertainties, the covariance on the integral ratios is

$$\text{Cov}(R_i, R_j) = \left(\frac{\partial R_i}{\partial \alpha} \right) \left(\frac{\partial R_j}{\partial \alpha} \right) \delta^2 + \delta_{i,j} \alpha^2 \delta^2 R'_i. \quad (3.64)$$

with

$$\frac{\partial R_i}{\partial \alpha} = R'_i + \alpha \frac{\partial R'_i}{\partial \alpha} \quad (3.65)$$

$$\frac{\partial R'_i}{\partial \alpha} = \frac{1}{F_i} \frac{\partial}{\partial \alpha} \int_{M_{3/\alpha}}^{M_{4/\alpha}} dM_{\gamma\gamma} f_i(M_{\gamma\gamma}), \quad (3.66)$$

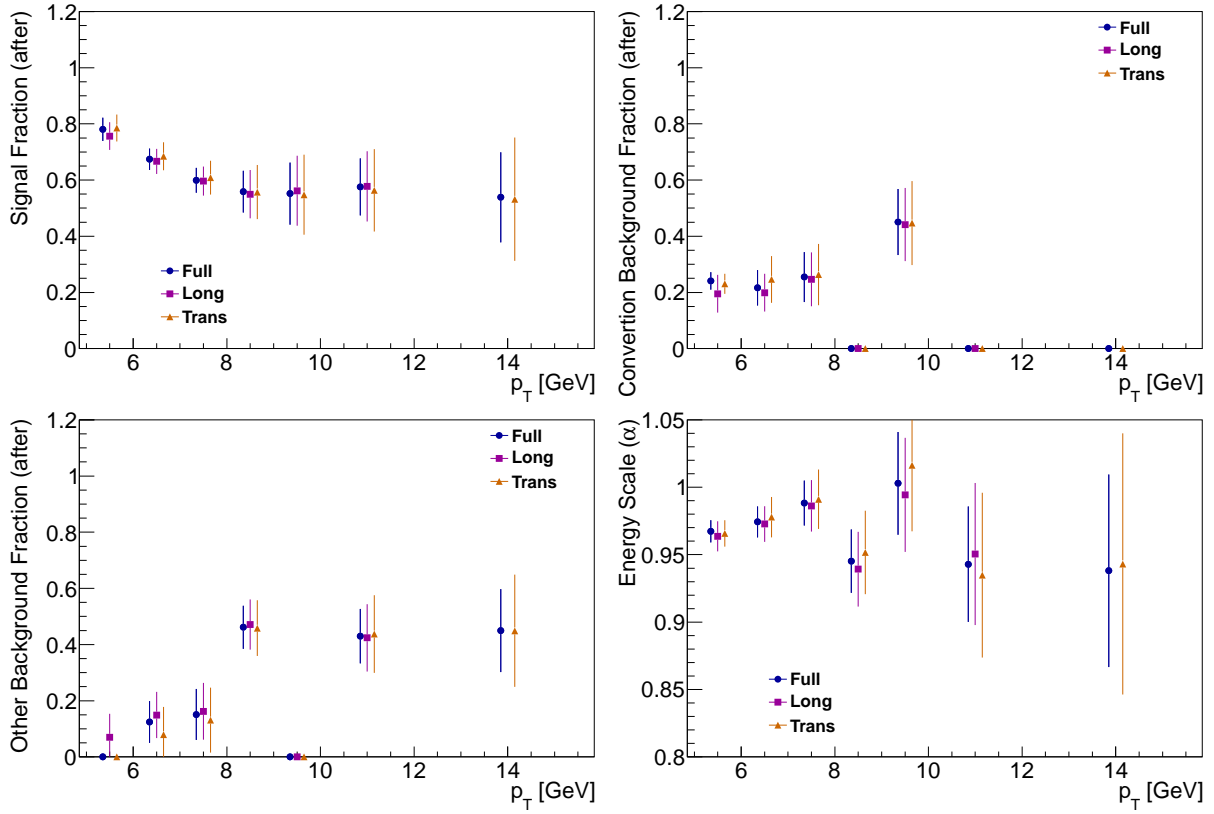


Figure 3.16: Comparison of the parameters from the combined fit for the three template options. Upper left panel is w_1 (signal fraction), upper right is w_2 (conversion background fraction), lower left is w_3 (other background fraction), and lower right is the energy scale factor α .

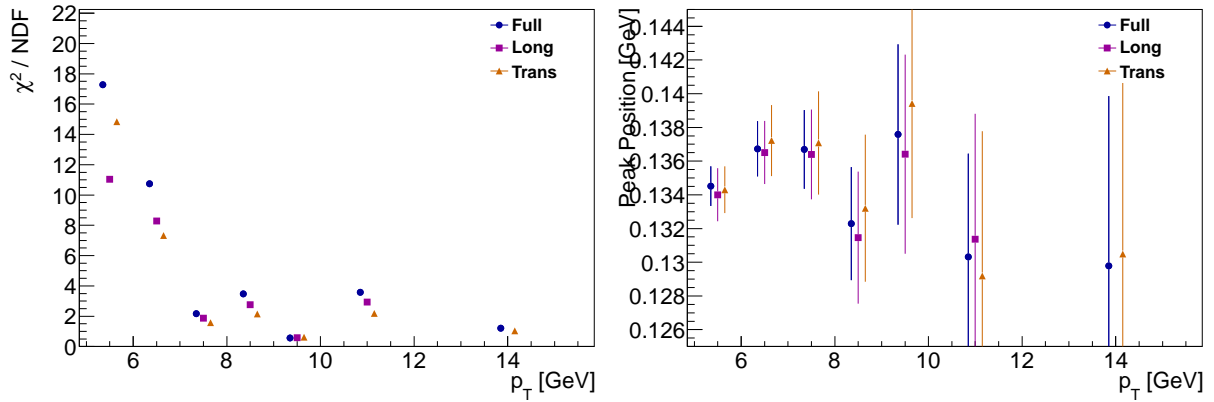


Figure 3.17: Left panel: reduced χ^2 vs. p_T for each data set. Right panel: derived peak position for the three data sets.

$$= \frac{1}{F_i} \frac{\partial}{\partial \alpha} \left[F_i(M_4/\alpha) - F_i(M_3/\alpha) \right], \quad (3.67)$$

$$= \frac{1}{F_i} \left[\frac{M_3}{\alpha^2} f_i \left(\frac{M_3}{\alpha} \right) - \frac{M_4}{\alpha^2} f_i \left(\frac{M_4}{\alpha} \right) \right]. \quad (3.68)$$

The uncertainty on R' which is independent of α comes from the uncertainty on the parameters in the functional templates (and is not present for histogram templates), and the uncertainty on the integrals I_i and F_i . For the case of functional templates, the integration error also includes the covariance on the parameters through `TF1::IntegralError`. For the case of histogram templates, the integration error involves the uncertainties on the bins. As the domain of I_i is a subset of the domain of F_i , and both are integrals of the same function, the uncertainties are thus correlated. The uncertainty on R'_i can be written,

$$\delta^2 R'_i = \sum_{k,\ell} \left(\frac{\partial R'_i}{\partial \theta_{i,k}} \right) \text{Cov}(\theta_{i,k}, \theta_{i,\ell}) \left(\frac{\partial R'_i}{\partial \theta_{i,\ell}} \right) + R_i'^2 \left((1 - R'_i) \frac{\delta^2 I_i}{I_i^2} + \frac{\delta^2 F_i}{F_i^2} \right). \quad (3.69)$$

The derivative of the ratio R'_i with respect to the template parameters is

$$\frac{\partial R'_i}{\partial \theta_{i,j}} = \frac{1}{F_i^2} \left(F_i \frac{\partial I_i}{\partial \theta_{i,j}} - I_i \frac{\partial F_i}{\partial \theta_{i,j}} \right), \quad (3.70)$$

and the derivative of the integrals are simply the integrals of the derivatives. The derivatives have been defined earlier for each template, and the integrals of the derivatives can then be computed using `TF1::Integral`.

Determining the Signal Fraction Uncertainty

For convenience, define

$$W = \sum_k w_k R_k. \quad (3.71)$$

For propagating uncertainties, one needs the Jacobians

$$J_{i,j}^{(w)} = \frac{\partial w_i^{(P)}}{\partial w_j} = \frac{\delta_{ij} R_j W - w_i R_i R_j}{W^2} \quad (3.72)$$

$$J_{i,j}^{(R)} = \frac{\partial w_i^{(P)}}{\partial R_j} = \frac{\delta_{ij} w_j W - w_i R_i w_j}{W^2} \quad (3.73)$$

The full covariance one fractions in the peak is

$$\text{Cov} \left(w_i^{(P)}, w_j^{(P)} \right) = \sum_{k,\ell} J_{i,k}^{(w)} \text{Cov}(w_k, w_\ell) J_{j,\ell}^{(w)} + \sum_{k,\ell} J_{i,k}^{(R)} \text{Cov}(R_k, R_\ell) J_{j,\ell}^{(R)} \quad (3.74)$$

Note, the above indices are indexing the templates (i.e. signal and backgrounds), and are computed within each reconstructed π^0 p_T or x_F bin (which are not specifically indexed in this section). As $i = 1$ corresponds to the signal template, the variance on the signal fraction $\delta^2 s$ (which enters into Equation 3.1) is

$$\delta^2 s = \text{Cov} \left(w_1^{(P)}, w_1^{(P)} \right) = \delta^2 w_1^{(P)}. \quad (3.75)$$

The further propagation of uncertainty is included in Section 3.1.

Signal Fraction within the Peak

The results for the signal fraction in the peak are shown in Figure 3.18. The values are quite consistent across the different run periods.

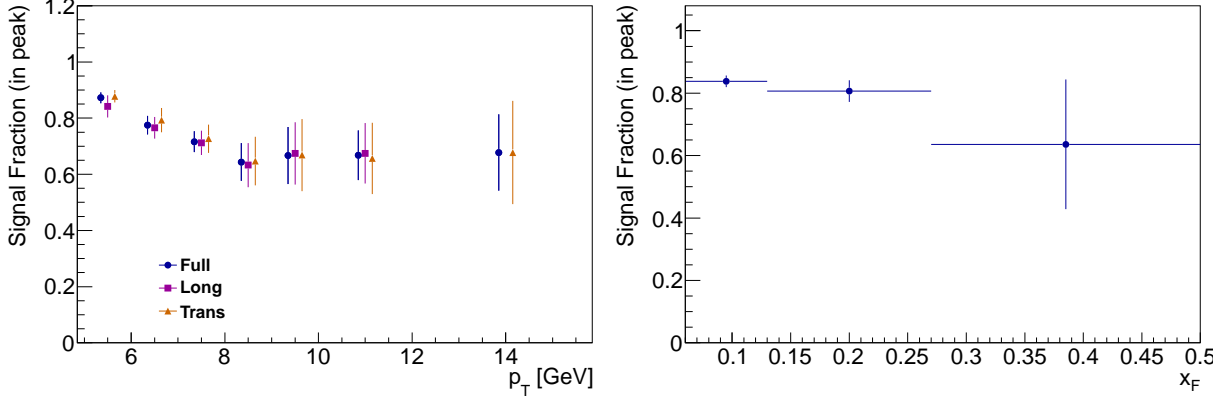


Figure 3.18: Signal fraction in the peak region, with uncertainties from Equation 3.75. Left panel is versus p_T and the right panel is versus x_F .

3.2.7 Background Asymmetry Corrections

The general procedure is to compute the asymmetries using the number of π^0 candidates in the peak region. The signal fraction per p_T (or x_F) bin is computed using the data summed over spin states and azimuthal bins. The background asymmetry is estimated, and the final, background-subtracted, asymmetry is computed according

$$A^{sig} = \frac{1}{s} (A^{raw} - (1-s)A^{bkg}). \quad (3.76)$$

and the variance is

$$\delta^2 A^{sig} = \frac{\delta^2 A^{raw}}{s^2} + \left(\frac{1-s}{s} \right)^2 \delta^2 A^{bkg} + \left(\frac{A^{raw} - A^{bkg}}{s^2} \right)^2 \delta^2 s. \quad (3.77)$$

For the longitudinal spin asymmetries, A^{raw} is the asymmetry computed using Equations 3.25, 3.26, and 3.24. For the transverse asymmetry, A^{raw} is $\varepsilon = p_1$, where p_1 is from fitting Equation 3.39 with Equation 3.40. The result is afterwards divided by the weighted polarization. Note, the polarization used for A_N is the number-of- π^0 -candidates weighted polarization, which is nearly numerically identical to the luminosity weighted polarization. Due to limited statistics, the background estimate is computed integrating over p_T and x_F , for all longitudinal and transverse spin asymmetries.

Another possibility has been considered, where the signal fraction is computed per spin state (and hemisphere/ ϕ_S bin for A_N). In this case, one can directly compute the signal asymmetry because the background has been subtracted before computing the asymmetry. With significantly higher data and Monte Carlo statistics, this method has the possibility of having lower uncertainties. However, given the present statistics cannot constrain the signal fractions as well for the spin-sorted data, and the fact that the background fractions and uncertainties are small, uncertainties are significantly higher using this “before” method.

Longitudinal Spin Asymmetry

In order to estimate the background asymmetry, the asymmetry of the π^0 candidates (without background subtraction) was computed in the signal region, $0.1 < M_{\gamma\gamma} < 0.2$ GeV/ c^2 , and two side band regions, $0 < M_{\gamma\gamma} < 0.1$ GeV/ c^2 and $0.2 < M_{\gamma\gamma} < 0.3$ GeV/ c^2 [17]. One must take care interpreting the results, as a fair amount of π^0 signal is also present outside of the π^0 peak region, as seen, e.g., in Figure 3.8. The results for A_L (blue), A_L (yellow) and A_{LL} are shown in Figure 3.19.

Each result is fit to a constant, with the results being shown in Table 3.2. The χ^2/ndf values are reasonable, or possibly too good. However, as the systematic uncertainty related to the uncertainty on this estimate is much smaller than the statistical uncertainty, this is not a concern. The average of the two

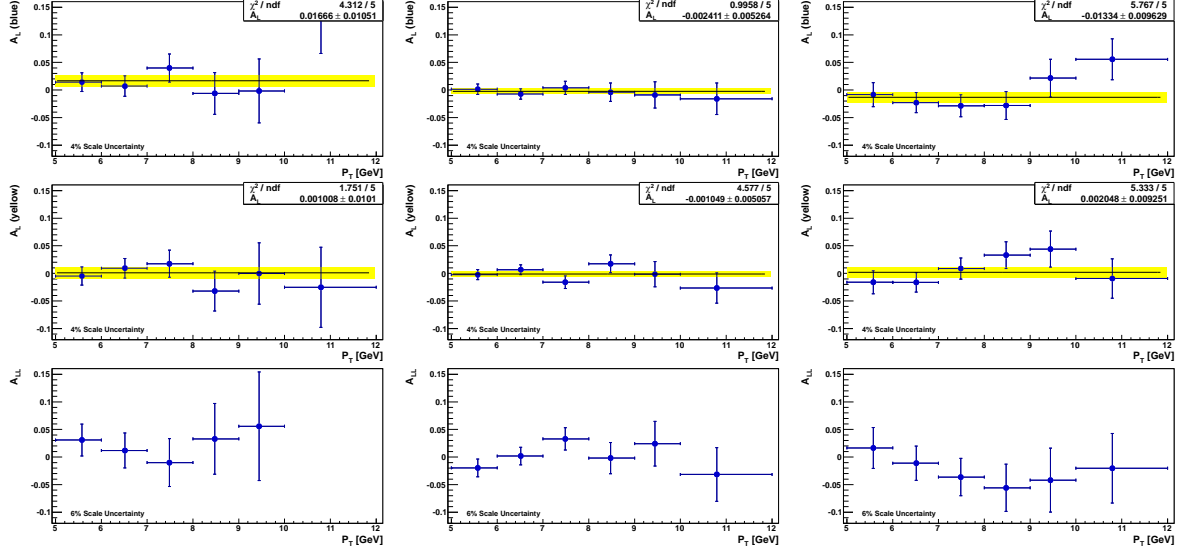


Figure 3.19: Raw longitudinal asymmetry results for three mass bins. Top row: A_L (blue); middle row: A_L (yellow); bottom row: A_{LL} . Left column: $0 < M_{\gamma\gamma} < 0.1 \text{ GeV}/c^2$; middle column: $0.1 < M_{\gamma\gamma} < 0.2 \text{ GeV}/c^2$; right column: $0.1 < M_{\gamma\gamma} < 0.2 \text{ GeV}/c^2$.

Mass Range [GeV]	A_L (blue)		A_L (yellow)		A_{LL}	
	Fit Result	χ^2/ndf	Fit Result	χ^2/ndf	Fit Result	χ^2/ndf
0.0 - 0.1	0.015 ± 0.010	4.49/6	0.007 ± 0.016	2.34/6	0.007 ± 0.016	5.39/6
0.1 - 0.2	-0.003 ± 0.005	1.13/6	0.001 ± 0.009	4.60/6	0.001 ± 0.009	4.93/6
0.2 - 0.3	-0.014 ± 0.009	5.78/6	-0.020 ± 0.016	5.40/6	-0.020 ± 0.016	2.29/6

Table 3.2: Tables of results for fitting results in Figure 3.19 to a constant.

sideband values are used for the estimate of the background asymmetry, and the uncertainty is propagated in the usual way. The final background estimates are listed in Table 3.3.

Transverse Spin Asymmetry

The background asymmetries for A_N were also estimated by computing the raw asymmetries in the mass bins described above. See Figure 3.20. The value for the blue beam is again the average of the sidebands, with the uncertainty propagated in the usual way. The yellow beam background asymmetry is set to zero, as a non-zero value would be parity violating. However, the uncertainty is set to uncertainty on the average of the two sidebands. For more details, see Ref. [18]. The final estimate of the background asymmetries are also in Table 3.3.

Background Asymmetry	Value
A_L (blue)	0.002 ± 0.007
A_L (yellow)	0.002 ± 0.007
A_{LL}	-0.004 ± 0.012
A_N (blue, $x_F < 0$)	-0.005 ± 0.013
A_N (yellow, $x_F < 0$)	0.000 ± 0.013

Table 3.3: Table of the background asymmetry estimate for each asymmetry type.

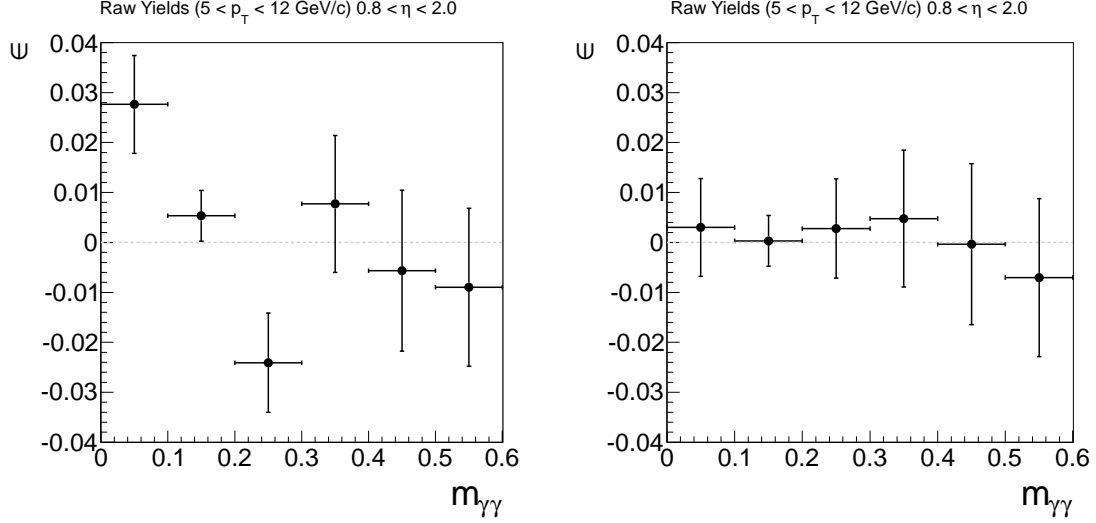


Figure 3.20: The raw A_N asymmetry ε versus mass. Left panel, $x_F < 0$; right panel, $x_F > 0$.

3.3 Unfolding and Reconstruction Efficiency

3.3.1 Computing the Migration Matrix

The migration matrix serves as the starting point for the smearing matrix and the reconstruction efficiency. Elements $M_{i,j}$ are defined as the number of π^0 s reconstructed in p_T bin i and generated in p_T bin j . If n is the number of p_T bins, then there is also a row with $i = n + 1$ which corresponds to generated π^0 s which are not reconstructed (in any p_T bin). Note, the unfolding is applied after cutting on the trigger, and thus all probabilities in this section are implicitly conditioned on the event having passed the trigger.

To fill the migration matrix, one must know the generated and reconstructed p_T values. However, it is often difficult to determine which reconstructed pair of photons corresponds with which generated π^0 . Each reconstructed π^0 can involve three to four SMD clusters, and each of these clusters may

- Have a 1-1 correspondence with a cluster caused by the generated π^0 .
- Be a subset of a cluster caused by the generated π^0 .
- Have some overlap with multiple generated particles, one (or more) of which may or may not have come from a π^0 .
- Be caused by false cluster splitting.

To categorize every possibility becomes a complex task.

Instead of the “bottom-up” approach based on comparing SMD clusters, we take a top-down approach, and compare the $\Delta R = \sqrt{\Delta\phi^2 + \Delta\eta^2}$ between generated π^0 s and reconstructed π^0 candidates. We associate a given reconstructed candidate with a given generated π^0 if $\Delta R < 0.04$. Several possibilities exist:

- a) there is a 1-1 match,
- b) one generated π^0 is associated with multiple reconstructed candidates,
- c) one generated π^0 is associated with no reconstructed candidates,
- d) one reconstructed candidate is associated with multiple generated π^0 s, or
- e) one reconstructed candidate is associated with no generated π^0 s.

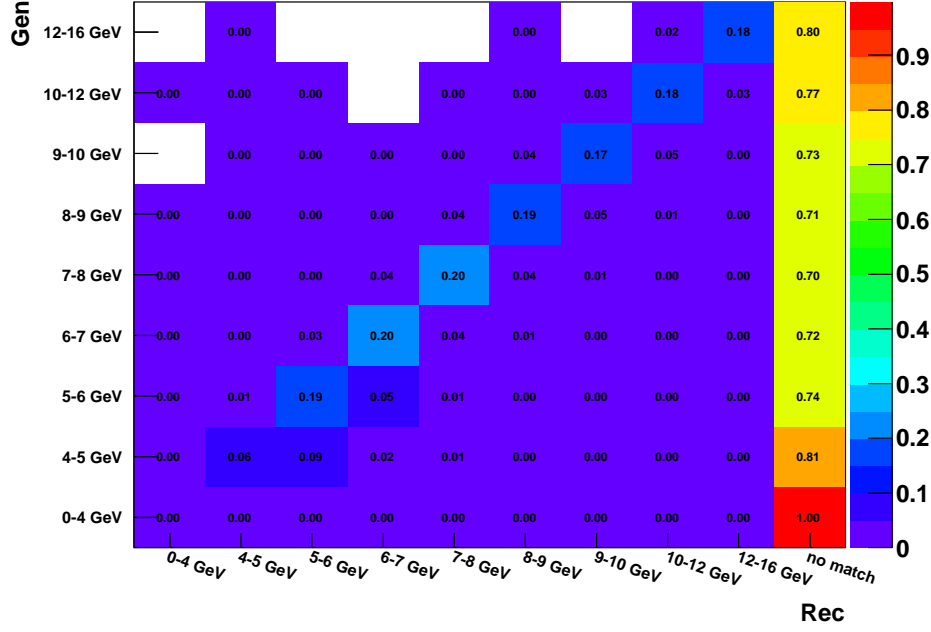


Figure 3.21: Migration matrix, normalized so the sum along each row (across all columns) is unity.

The merging procedure ensures that no reconstructed candidates are within $\Delta R < 0.05$. This results in each association between candidate pair and generated π^0 being uniquely in one of the five categories (a)-(e).

For case (a), the entry of $M_{i,j}$ for appropriate values of i and j is incremented by 1. For case (b), a weight is set equal to one over the number of reconstructed candidates, and $M_{i,j}$ is incremented by that weight for the appropriate value of j and for each appropriate value of i . For case (c), $M_{i,j}$ is incremented by one for the appropriate value of j and $i = n + 1$. For case (d), which is very rare, the reconstructed π^0 is associated with the generated π^0 with closest p_T and is then treated as in case (a). Case (e) is background and ignored, as the background has already been accounted for through the signal fraction.

Since the Monte Carlo is generated in multiple partonic p_T bins, the migration matrix is computed per p_T bin, and the weighted sum is formed, using the one over the generated luminosity of each partonic p_T bin.

The overall normalization of the migration matrix is not of interest at this stage, and so the matrix is typically presented by either normalizing the sum of each row or column to unity. The resulting migration matrix, with these two options for normalization, are shown in Figures 3.21 and 3.22. Note, that ROOT draws the matrix transposed from the usual manner, in that elements with a fixed i , i.e. the first index or the reconstructed bin, is drawn as a column instead of a row.

3.3.2 Computing the Smearing Matrix

The migration matrix is proportional to a numeric estimate of the joint probability of generating a π^0 with $p_T^{(G)}$ and reconstructing a π^0 with $p_T^{(R)}$. Let n_1 indicate the first p_T bin to be included in the smearing matrix, and n_2 the last p_T bin. Let n be the total number of bins, and let the $n + 1$ reconstructed bin be the “not reconstructed” bin. The smearing matrix S thus has $n_2 - n_1 + 1$ rows and columns, while the migration matrix M is $(n + 1) \times n$. Note the rows indicate reconstructed bins, and the columns generated bins.

The quantity needed for unfolding is the conditional probability of reconstructing a π^0 with $p_T^{(R)}$ given a generated π^0 with $p_T^{(G)}$,

$$p\left(p_T^{(R)} \middle| p_T^{(G)}\right) = \frac{p\left(p_T^{(R)}, p_T^{(G)}\right)}{p\left(p_T^{(G)}\right)}, \quad (3.78)$$

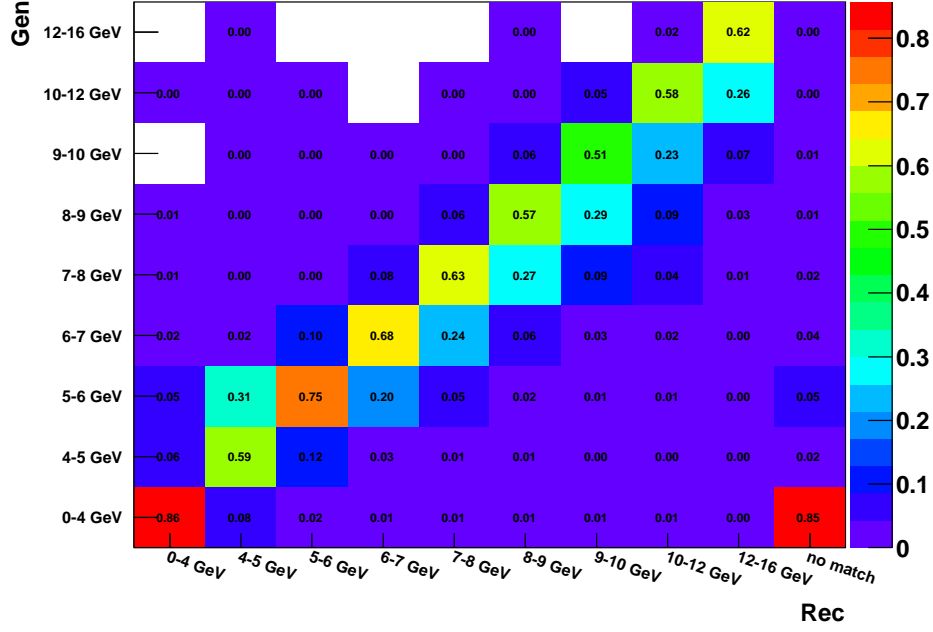


Figure 3.22: Migration matrix, normalized so the sum along each column (across all rows) is unity.

$$\approx \frac{M_{i,j}}{\sum_{k=1}^n M_{k,j}}. \quad (3.79)$$

Define

$$S_{i,j} = \frac{M_{i,j}}{\sum_{k=1}^n M_{k,j}}. \quad (3.80)$$

Therefore, the matrix S is similar to Figure 3.21, though they differ in that S does not include the no match column in the normalization, while the figure does. The reconstruction efficiency is closely related, and is defined as

$$\epsilon_R = \frac{\sum_{k=1}^n M_{k,j}}{\sum_{k=1}^{n+1} M_{k,j}}. \quad (3.81)$$

An alternate approach is to normalize only over the bins used for for unfolding. One then has

$$S'_{i,j} = \frac{M_{i,j}}{\sum_{k=n_1}^{n_2} M_{k,j}}, \quad (3.82)$$

$$\epsilon'_R = \frac{\sum_{k=n_1}^{n_2} M_{k,j}}{\sum_{k=1}^{n+1} M_{k,j}}. \quad (3.83)$$

Note that $S'_{i,j}\epsilon'_R = S_{i,j}\epsilon_R$ and thus either option is equivalent for computing the cross section.

The “outside smeared in” background $N_i^{(IO)}$ can be computed as

$$N_i^{(IO)} = L \sum_{j=1}^{n_1-1} M_{i,j} + L \sum_{j=n_2+1}^n M_{i,j}. \quad (3.84)$$

Assuming the unfolded yield is approximately the same as the yield in the simulation, i.e. setting $N_j^{(U)}$ in equation to the value $\sum_{j=1}^n M_{i,j}$ in Equation 3.5, and solving Equation 3.5 for f_i results in

$$f_i = \frac{\sum_{j=n_1}^{n_2} M_{i,j}}{\sum_{j=1}^n M_{i,j}} \quad (3.85)$$

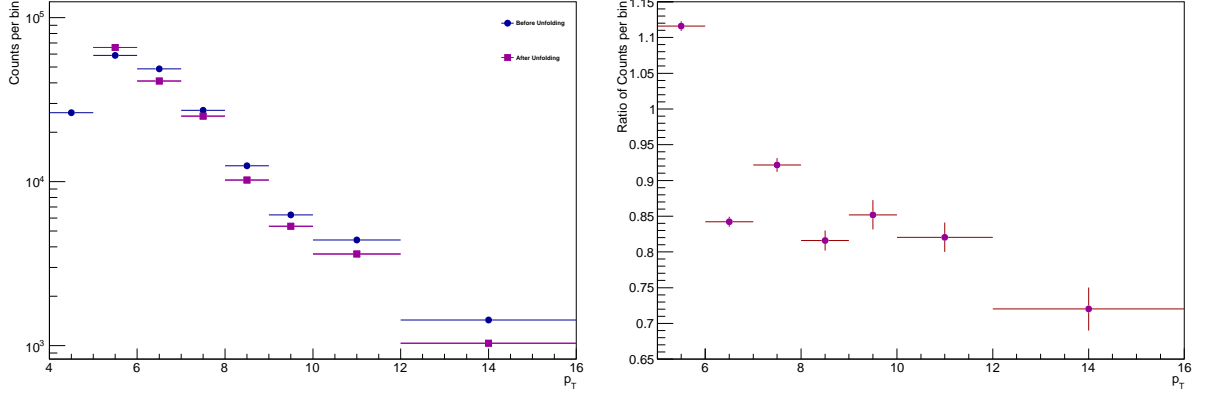


Figure 3.23: Left panel: number of π^0 counts before and after unfolding, with unfolding applied for p_T in 5-16 GeV/c. Right panel: ratio of the number of counts after unfolding over the number of counts before unfolding.

The code currently solves Equation 3.6 rather than Equation 3.4, though the difference between the two methods is minor [24].

The data and Monte Carlo have some disagreement for sub-trigger-threshold π^0 s, as seen in Figure 2.3. This is the main cause of the difference seen in Ref. SteveBlogAddVsMult. Additionally, because this discrepancy is thought to be caused by the trigger, it does not effect the value of $M_{i,2} + M_{i,10}$, where bin 2 is the reconstructed $4 < p_T < 5$ GeV/c and bin 10 is the “not reconstructed” bin. Thus, setting $n_1 = 3$ minimizes the effect of the discrepancy, and the smearing from bin 2 is still included through the correction procedure of using f_i or $N^{(IO)}$ but shows up summed with the “not reconstructed” bin.

3.3.3 Unfolded Counts

The equation for unfolding used in the code is Equation 3.6. The code solves this system of liner equations using by computing the QR decomposition of S' using Householder transformations. The quantity $N_j^{(U)}$ can be determined from the QR decomposition, while the full inverse S'^{-1} is used for the uncertainty propagation, i.e. Equation 3.7. The QR decomposition is a wise choice, as S^{-1} may be poorly conditioned. In the specific cases occurring in this analysis, the matrix condition is approximately unity, which is extremely good.

The number of counts, before and after unfolding, are shown in the left panel of Figure 3.23, with the results being unfolded in the p_T range 5-16 GeV/c. The ratio of counts after unfolding over counts before unfolding is shown in the right panel of Figure 3.23. Unfolding decreases the number of counts in most bins, due to the sharply falling cross section and the fairly stable p_T resolution.

3.3.4 Computing the Reco. Eff

The reconstruction efficiency is likewise computed based on the migration matrix, but using the subvector corresponding to generated π^0 s with no matched reconstructed π^0 candidate, shown in Equation 3.81. The resulting efficiency is shown in Figure 3.24, along with the trigger efficiency and the overall efficiency (reconstruction efficiency times trigger efficiency). At low p_T , the reconstruction efficiency is decreased due to the lower energy photon not passing the energy threshold as often (i.e. a smaller $Z_{\gamma\gamma}$ phase space in the p_T range above the photon energy cut). At higher p_T , the efficiency is decreases due to the two photons from the π^0 having a smaller separation. With smaller separation distances, it is more difficult to correctly identify the response of one versus two photons.

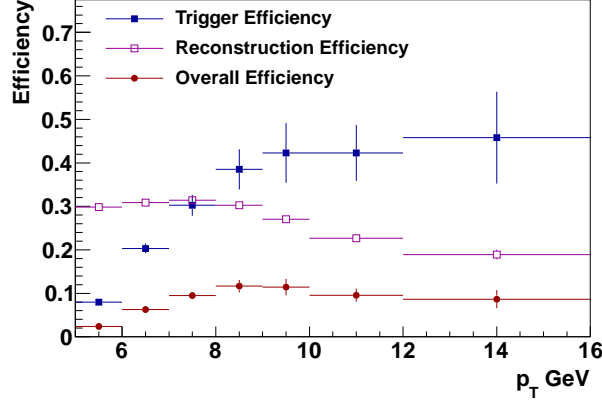


Figure 3.24: Trigger efficiency and reconstruction efficiency verses p_T GeV/c. Also shown in the total efficiency, the product of the trigger and reconstruction efficiencies.

3.4 Trigger Efficiency

The trigger efficiency is calculated from Pythia Monte Carlo data. In order to optimize processing time and storage, filters have been introduced [20] at both the Pythia and BFC level. Again, in order to best use processing time and storage, the effect of each of these components is computed separately, i.e. the effect of the Pythia filter, the BFC filter, and the trigger cut. The total trigger efficiency is then a product of three terms, related to each of these three features. For ease of notation, the term associated with the Pythia filter will be labeled (pFilt), the term associated with the BFC filter will be labeled (bFilt), and the term associated with the trigger will be labeled (trig). Recall, the efficiency is defined (as discussed in Section 3.1) as a conditional probability of the event passing the filter or trigger given that the event contains a generated π^0 within a given p_T bin. Note, the Monte Carlo data, in all cases, is again generated in partonic p_T bins, and weighted sums over partonic p_T are always carried out before taking ratios.

(pFilt) The (pFilt) term is computed by using a private Pythia production, using the Pythia generator within ROOT, and using a port of the Pythia level filter such that it will run within ROOT without the root4star or starsim framework. Each π^0 with $\eta > 0.5$ is initially saved to a TTree, along with a flag whether the event passed the Pythia filter. The (pFilt) value per bin is computed as the ratio of the number of π^0 s passing the filter divided by the number generated. Note, the bin may be either a 1D p_T or η bin or a 2D p_T or η bin. The result is shown in Figure 3.24, in the panel labeled (pFilt).

(bFilt) The (bFilt) term is again computed by using a private Pythia production, this time however **starsim** and the BFC is used. The official Pythia production could not be used, as the **.fzd** files were not saved. The **fzd** files, which contain the **Geant** output of **starsim** and is the input to the BFC, are saved for the private production and converted to **.geant.root** files using the standard routine, **fz2root.C**. The BFC also outputs the **Geant** information, for events which passed the filter, in the form of a **.geant.root** file. The (bFilt) value per bin is the number of π^0 s per bin which passed the Pythia and BFC filters (which are in the **.geant.root** file coming out of the BFC) divided by the number of π^0 s per bin which passed the Pythia filter (which are in the **.geant.root** file which came directly from the **.fzd** file).

(trig) For the trigger within filter efficiency, the official production is used. The term is computed as the number of π^0 s per bin in events passing the trigger and the filters divided by the number of π^0 s per bin in events which passed the filters.

Other possibilities One could adjust the Monte Carlo productions to test different combinations of these terms. For example, one could compute the product of (pFilt) times (bFilt) directly by proceeding as for the

(bFilt) alone, but by turning off the Pythia filter. These various checks were done using a relatively small sample, as a sanity check. The results are shown in Figure 3.25. No discrepancy is apparent.

Results The results for the product of the three terms, each computed separately, is shown in Figure 3.24. As expected, the efficiency is lower at lower p_T and rises to a plateau value. The plateau is at about 0.5, and occurs around $p_T = 10$ GeV/ c . The plateau is somewhat low due to geometric cuts in the trigger and filter.

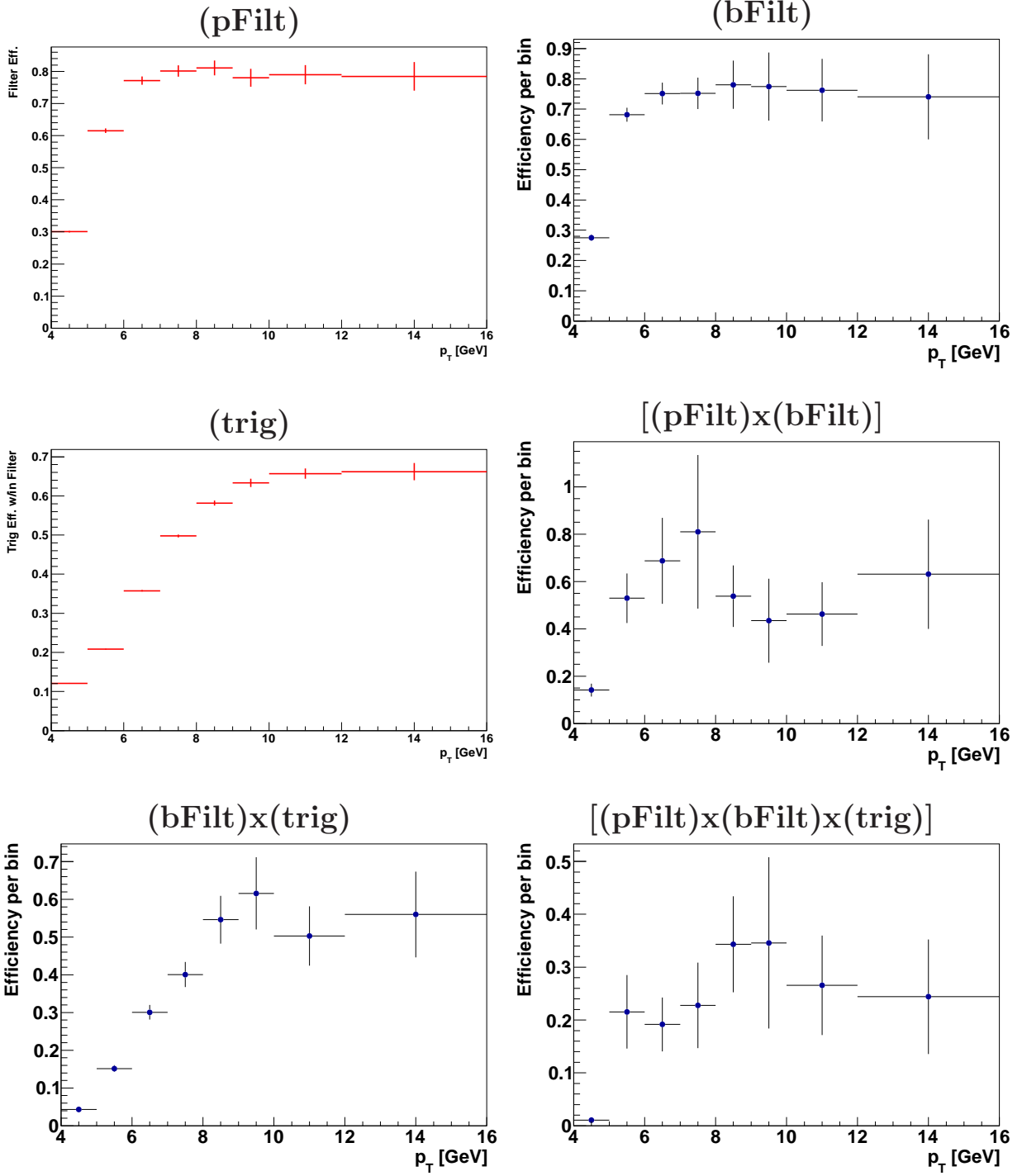


Figure 3.25: Comparison of computing the terms in the trigger efficiency separately or simultaneously. Square brackets indicate quantities computed simultaneously. Note: these plots were made Nov. 12th, when the simulated trigger for the simulation was still set to level ‘h’, as was the data. The more recent setting for simulations is ‘i’, which is 3% higher.

Chapter 4

Systematics

4.1 Vertical Scale Uncertainties

For the cross section, the vertical scale uncertainty is due to the uncertainty on the luminosity, as discussed in Section 2.4. The vertical scale uncertainties on the asymmetries are due to the uncertainty on the polarization. The luminosity weighted polarization is used for the asymmetries. Standard propagation of uncertainty results in a 4% scale uncertainty for the blue and yellow beam A_L results, a 6% scale uncertainty for the A_{LL} result, and a 4% scale uncertainty for the blue and yellow beam A_N result.

4.2 Non-Vertical Scale Uncertainties

Table 4.1 lists all of the considered systematics, shows for which result (cross section or longitudinal or transverse spin asymmetry) each systematic is applicable, and indicates whether the numeric value is included in the complete systematic. Some systematics are small enough that the numeric value is not included. Also, as noted in Section 3.1.3, some uncertainties denoted systematic for the cross section and longitudinal asymmetries are counted in the statistical uncertainty for the transverse asymmetry. A field in Table 4.1 indicates which uncertainties these are. This paragraph is followed by a subsection for each systematic in Table 4.1.

4.2.1 Background Fit–Propagated Uncertainty

The propagated uncertainty refers to that included in Equation 3.75.

Source	$d\sigma$	A_{LL}	A_N
Bkg. Fit–propagated	✓	✓	✓
Bkg. Fit–residual fit	✓	✓	✓
Bkg. asym. uncert.	✗	✓	✓
Single Beam Background	✗	✗	✓
Unfolding–propagated	✓	✗	✗
Unfolding–bin range	✓	✗	✗
Reconstruction efficiency	✓	✗	✗
Trigger efficiency	✓	✗	✗
ETOW energy resolution	✓	✗	✗
ETOW energy scale	✓	✗	✗

Table 4.1: Systematic uncertainties which are non-negligible for at least one result are listed. Each uncertainty is marked ✓ in the column for the result(s) in which the systematic is both applicable and non-negligible.

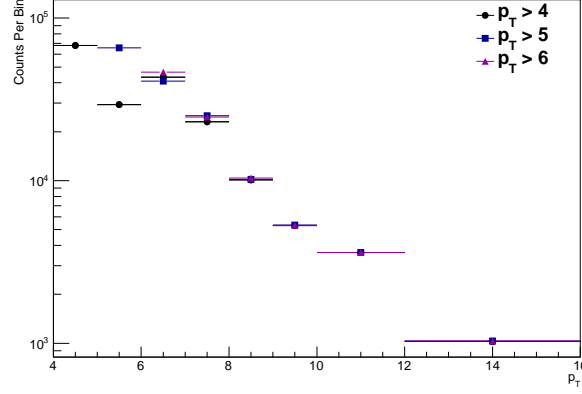


Figure 4.1: Unfolded counts per p_T bin, for different options of the lower bin limit for unfolding. The results agree well above 6 GeV/ c and quite well above 8 GeV/ c .

4.2.2 Background Fit–Residual Fit

The fit residuals are fit to a constant within the π^0 peak region, and this constant times the bin width gives a number of π^0 candidates, N^{res} . For the cross section, N^{res} is a systematic uncertainty on the number of π^0 counts. For the spin asymmetries, this value is propagated to an uncertainty on the signal fraction by dividing by the number of raw counts, i.e. an additional uncertainty on the signal fraction of N^{res}/N^{raw} is included.

4.2.3 Background Asymmetry Uncertainty

Section 3.2.7 details the background subtraction procedure for the spin asymmetries. The background asymmetry uncertainty is the propagated uncertainty due to the uncertainty on the background estimate.

4.2.4 Unfolding–Propagated Uncertainty

The uncertainties on the entries of the smearing matrix, related to the Monte Carlo statistics, is propagated analytically (as described in Section 3.1.1) and assigned as a systematic uncertainty.

4.2.5 Unfolding–Bin Range

The choice of which p_T bins to include effects the result, especially in the lower p_T bins. See Figure 4.1. The mean of the various choices is used for the final central value, and a systematic equal to the standard deviation is assigned.

4.2.6 Reconstruction Efficiency

The uncertainty on the reconstruction efficiency (arising from the amount of Monte Carlo statistics) is included as a systematic uncertainty on the cross section.

4.2.7 Trigger Efficiency

The uncertainty on the trigger efficiency (arising from the amount of Monte Carlo statistics) is included as a systematic uncertainty on the cross section.

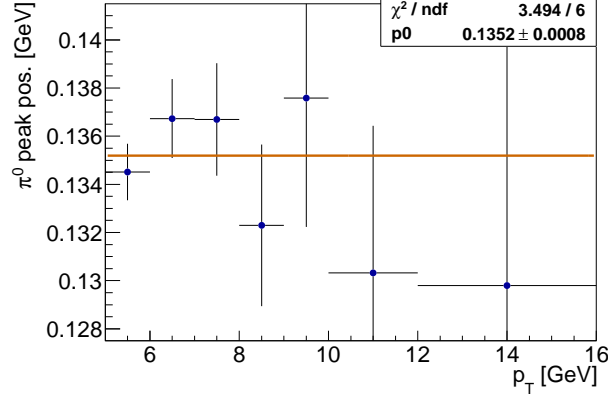


Figure 4.2: Peak position fit to a constant value.

4.2.8 ETOW Energy Resolution

Since the counts per p_T bin are corrected for unfolding, the only additional place the ETOW energy resolution causes an effect is in the mean p_T factor in the cross section. The ETOW resolution is $\delta E/E = 0.16/\sqrt{E}$. We put an uncertainty on $\langle p_T \rangle$ of

$$\delta^2 \langle p_T \rangle = 0.16 \sqrt{\frac{\langle p_T \rangle}{\cosh 1.1}}, \quad (4.1)$$

and propagate this to an uncertainty on the cross section.

4.2.9 ETOW Energy Scale

The EEMC group decided upon a 3% scale uncertainty for the ETOW energy scale, based, in part, by the differences in the π^0 peak position between the thesis of Weihong and this analysis, and also by considering the variation of the π^0 peak position within this analysis.

A more recent analysis [25] focusing just on the variation of the π^0 peak position suggests a value of 0.6% if one takes into account the error bars. This value is obtained by fitting the peak position to a constant across p_T , as shown in Figure 4.2. While the χ^2/ndf is unexpectedly small, the error bars are dominated by the uncertainty in the α scale factor. The error bars seem to accurately represent that the peak position of the signal is not extremely well defined, in agreement with visual inspection of Figure 3.8.

The relative uncertainty on the fit parameter is 0.6%, and the central value is within 0.25σ of the PDG accepted value. While the uncertainty in α already captures some aspect of the EEMC energy scale, there is no indication of an further scale uncertainty greater than 1%. Even ignoring the error bars, the standard deviation of the central values is 2.97 MeV, or 2.20% variation from the PDG value.

Other factors considered in the choice of the EEMC energy scale uncertainty include the p_T variation seen in W. He's thesis [6], and a variety of past experiences related to the relative and absolute EEMC energy scale. For example, it has historically (and continues) to be difficult to quantify gain shifts across different running years. After discussion within the EEMC group, it was decided to use the value of 3%.

The effect of the EEMC energy scale uncertainty on the cross section is computed as follows. For each edge between p_T bins, an exponential is fit using the cross section value for each of the adjacent p_T bins. The integral of this exponential between one plus or minus the EEMC energy scale uncertainty times the bin edge is computed, and assigned as a systematic uncertainty on the cross section in the bin which is at just greater p_T than the p_T bin edge under consideration.

4.2.10 Single Beam Background

It is expected that the single beam background would have a more dominant effect on A_N than on the cross section or A_{LL} , since the single beam background has azimuthal dependence due to the floor of the beam

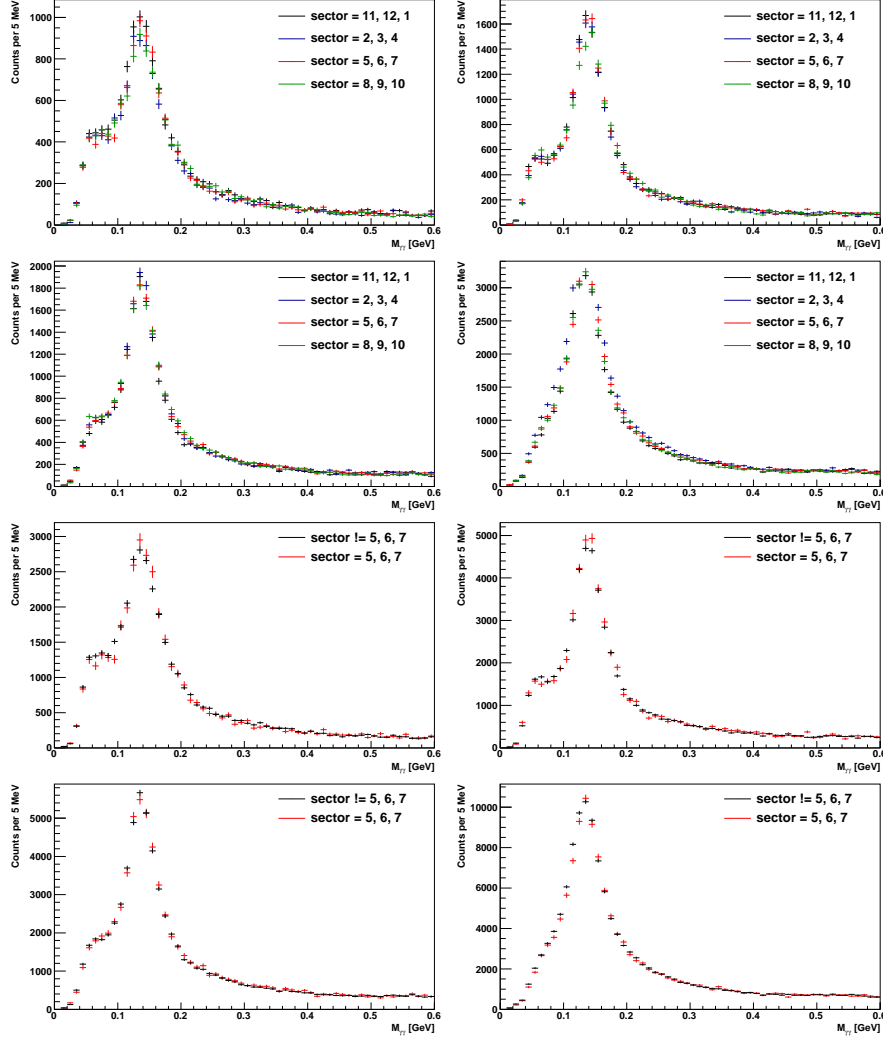


Figure 4.3: Comparison of the $M_{\gamma\gamma}$ distributions for different quarter sections of the EEMC. These plots were made January 18th, using a slightly modified set of cuts. The minor changes in the cuts do not diminish nor alter the message of this figure.

tunnel shielding the lower portion of the detector. A detailed study is presented in Part I of this analysis note, with the result of an uncertainty of 0.002 (absolute value) on A_N across all p_T and x_F bins.

To check for any apparent effect on the cross section or longitudinal asymmetries, the $M_{\gamma\gamma}$ distribution was separated into various sections, as shown in Figure 4.3. No effect is apparent. The single beam background for the cross section and longitudinal spin asymmetries thus considered negligible.

4.2.11 Residual Polarization Effects

Many studies have been conducted in the context of other spin analyses at STAR regarding the effect of residual polarization, i.e. a longitudinal component of the beam spin during transverse running and vice versa. Owing to the small size of all of our measured asymmetries and the large uncertainties, and based on the small values of transverse polarization, it has been concluded that such effects are negligible for this analysis.

4.2.12 Relative Luminosity

The uncertainty on the relative luminosity, based on the number of scalar board counts, is negligible compared to the uncertainty on the number of π^0 counts.

4.2.13 Other Studies for A_N

Effects of ϕ -binning In the A_N extraction, the data is binned in ϕ before fitting to the Fourier moments. The finite bin width and the distribution of events within the bin could effect the extracted moments. To determine the effect, the data is reweighted, using each data point once for each of positive and negative polarization, to effectively depolarize the data and induce a value of $A_N = 1$. The resulting extracted A_N is within 1.5% of the input [19] indicating this effect is negligible compared to other uncertainties.

Single-Arm Study Instead of using the cross ratio formula for A_N , results were also obtained using the following formula:

$\langle p_T \rangle_{LW}$	Stat.	Tot. Sys.	Fit Prop.	Res. Fit.	Unf. Prop.	Unf. Range	Reco. Eff.	Trig. Eff.	Energy. Res.	Energy Scale
5.456	0.004	0.441	0.001	0.001	0.018	0.277	0.009	0.039	0.052	0.336
6.456	0.007	0.416	0.002	0.002	0.025	0.055	0.009	0.056	0.049	0.405
7.456	0.009	0.372	0.003	0.001	0.031	0.034	0.011	0.080	0.045	0.357
8.456	0.016	0.471	0.006	0.003	0.053	0.011	0.016	0.119	0.043	0.450
9.456	0.022	0.435	0.010	0.003	0.075	0.003	0.025	0.162	0.040	0.393
10.830	0.022	0.631	0.010	0.003	0.081	0.001	0.033	0.152	0.038	0.604
13.379	0.036	1.453	0.019	0.009	0.170	0.003	0.060	0.231	0.034	1.422

Table 4.2: Table of relative uncertainties. The left column contains the Lafferty-Wyatt points for the cross section. Following columns contain the statistical and total systematic uncertainty, followed by columns for each of the contributing systematic uncertainties.

p_T Range [GeV/c]	A_{LL}	Stat.	Tot. Sys.	Fit. Prop.	Res. Fit.	Bkg. Uncert.
5-6	-0.023	0.020	0.003	0.001	0.001	0.003
6-7	0.004	0.021	0.004	0.001	0.000	0.004
7-8	0.049	0.029	0.007	0.004	0.001	0.005
8-9	0.000	0.044	0.007	0.001	0.000	0.007
9-10	0.039	0.060	0.011	0.009	0.001	0.006
10-12	-0.044	0.073	0.009	0.007	0.000	0.006

Table 4.3: Table of A_{LL} values and uncertainties per p_T bin. The right three columns are the values which are summed in quadrature to get the total systematic uncertainty.

$$\begin{aligned}
\frac{N^\uparrow(\phi) - N^\downarrow(\phi)}{N^\uparrow(\phi) + N^\downarrow(\phi)} &= \frac{(\Delta L/L_{\text{tot}}) + P_{\text{beam}} A_N \sin(\phi)}{1 + (\Delta L/L_{\text{tot}}) P_{\text{beam}} A_N \sin(\phi)}, \\
&\approx \frac{\Delta L}{L_{\text{tot}}} + P_{\text{beam}} A_N \sin(\phi),
\end{aligned} \tag{4.2}$$

which was then fit to $p_0 + p_1 \sin(\phi)$, with p_1 being interpreted as ε , just as it was when using the square-root formula. The approximation holds for $\Delta L/L \ll 1$. The results were consistent with the results from the cross ratio formula. For more details, see Ref. [21].

Signal Region Study A systematic related to the choice of the mass peak window was also investigated. The result was negligible over most bins, with one or two exceptions [22, 23]. Further studies suggested that the large fluctuations were likely statistical [21], and that this systematic was possibly double counting other systematics. The conclusion was to not include this systematic in the results.

4.3 Table of Results

Tables 4.2, 4.3, 4.4 and 4.5 include the numeric value for each of the contributing systematic uncertainties, as well as the combined systematic uncertainty. The dominant uncertainty for the cross section is the energy scale uncertainty. The dominant uncertainty for the spin asymmetries is the statistical uncertainty.

p_T [GeV/c] or x_F Range	A_N	Stat.	Tot. Sys.	Fit. Prop.	Res. Fit.	Bkg. Uncert.	Single. Beam Bkg.
0.6-0.13	-0.003	0.017	0.003	0.000	0.000	0.002	0.002
0.13-0.2	-0.003	0.018	0.004	0.001	0.000	0.004	0.002
0.2-0.27	0.036	0.046	0.009	0.006	0.001	0.006	0.002
5-6	-0.005	0.018	0.003	0.001	0.000	0.002	0.002
6-7	-0.005	0.022	0.004	0.001	0.001	0.004	0.002
7-8	0.020	0.031	0.005	0.002	0.000	0.005	0.002
8-9	0.013	0.047	0.006	0.001	0.000	0.006	0.002
9-10	0.044	0.075	0.026	0.025	0.000	0.007	0.002
10-12	-0.121	0.080	0.041	0.041	0.000	0.005	0.002

Table 4.4: Table of A_N values and uncertainties for $x_F > 0$. The right four columns are the values which are summed in quadrature to get the total systematic uncertainty.

p_T [GeV/c] or x_F Range	A_N	Stat.	Tot. Sys.	Fit. Prop.	Res. Fit.	Bkg. Uncert.	Single. Beam Bkg.
0.6-0.13	0.016	0.017	0.003	0.001	0.001	0.002	0.002
0.13-0.2	0.011	0.017	0.004	0.001	0.000	0.004	0.002
0.2-0.27	-0.003	0.045	0.006	0.001	0.000	0.006	0.002
5-6	0.003	0.018	0.003	0.000	0.000	0.002	0.002
6-7	0.016	0.022	0.005	0.001	0.001	0.004	0.002
7-8	0.019	0.031	0.006	0.002	0.000	0.005	0.002
8-9	0.034	0.047	0.009	0.006	0.001	0.006	0.002
9-10	-0.039	0.074	0.026	0.025	0.000	0.007	0.002
10-12	0.068	0.079	0.023	0.022	0.000	0.005	0.002

Table 4.5: Table of A_N values and uncertainties for $x_F < 0$. The right four columns are the values which are summed in quadrature to get the total systematic uncertainty.

Chapter 5

Results

5.1 Cross Section

The proposed figures for the cross section to show in the paper are shown in Figures 5.1, 5.2. Figure 5.1 includes the results along with selected, previously published, STAR π^0 cross section results, specifically the BEMC result (2005 data) [26] and two FPD results [27, 28]. This plot highlights the unique η and p_T coverage of this measurement, as well as showing overall abilities of the entire STAR detector. The cross section is plotted using at the LW-points [29]. The LW points are computed by fitting the final cross section, with all uncertainties, to an exponential over the full range.

Figure 5.2 compares the cross section results with a pQCD calculation from Ref. [30]. The EEMC π^0 cross section data points lie between the p_T and $2p_T$ scale. This is qualitatively consistent with published STAR $\sqrt{s} = 200$ GeV BEMC results (Figure 5.4), the published PHENIX $\sqrt{s} = 200$ GeV results (Figure 5.3, left panel) and the preliminary PHENIX $\sqrt{s} = 500$ GeV results (Figure 5.3, right panel). In all cases, the cross section is lower than the p_T -scale theory curve in the region of $6 < p_T < 16$ GeV/ c . Such a disagreement could be the signs of non-perturbative effects, or may suggest further refinements of the model for the π^0 fragmentation function. In private discussions with M. Stratmann and other theorists, the consensus has been that being within the energy scale uncertainty is a high level of agreement.

5.2 Longitudinal Spin Asymmetries

The A_L results for blue and yellow beam are given in Figure 5.5. The asymmetries are consistent with zero, as expected. Fitting to a constant over p_T yields -0.004 ± 0.007 for blue and -0.002 ± 0.007 for yellow, with reduced χ^2 values of 1.0/5 and 4.4/5. These can be compared with the preliminary ϵ_L values from W. He's thesis [6], also shown at SPIN 2010 [31].

The A_{LL} results are given in Figure 5.6. These can be compared with the preliminary results from W. He's thesis [6], also shown at SPIN 2010 [31]. The A_{LL} results cover a lower range in Bjorken x_2 [32] than inclusive jets and thus may still have impact on the global fits. Fitting A_{LL} to a constant results in 0.001 ± 0.012 , with a reduced χ^2 of 4.9/5.

5.3 Transverse Spin Asymmetry

The final A_N results are shown in Figure 5.7. The results for $x_F < 0$ are consistent with zero, as expected, and within the $x_F > 0$ coverage, no significant asymmetry is apparent. Within the uncertainties, no p_T dependence can be concluded. A plot comparing this result with previous STAR results is shown in Figure 5.8. The results are constant and show the unique x_F range of the EEMC.

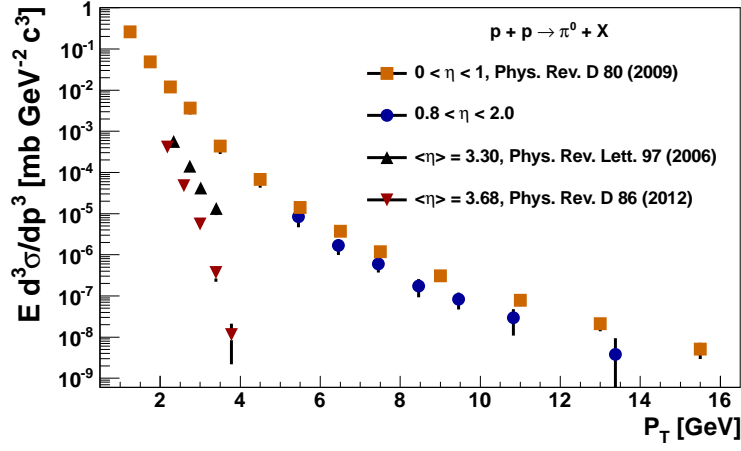


Figure 5.1: The π^0 differential cross section is plotted versus p_T , for various STAR subdetectors. Uncertainty bars are the combined statistical and systematic uncertainties. *[This plot is intended for the publication.]*

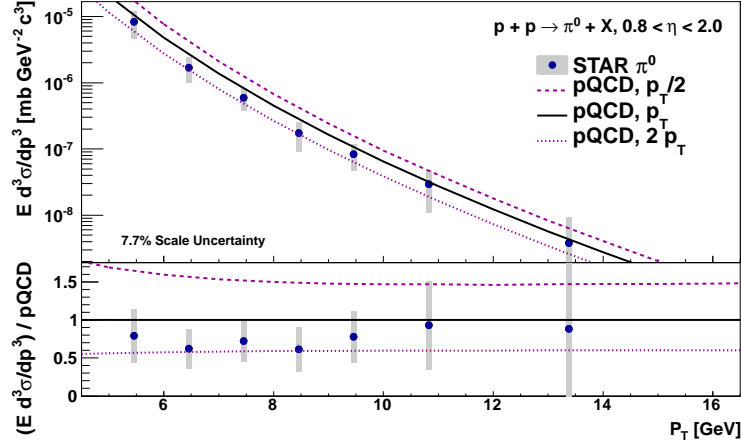


Figure 5.2: The π^0 cross section is compared with a pQCD [30] theoretical prediction at three different scales. The lower panel plots the ratio of the measurement over the p_T -scale theory curve. The uncertainty bars are the statistical uncertainty, and the uncertainty bands are the systematic uncertainty. *[This plot is intended for the publication.]*

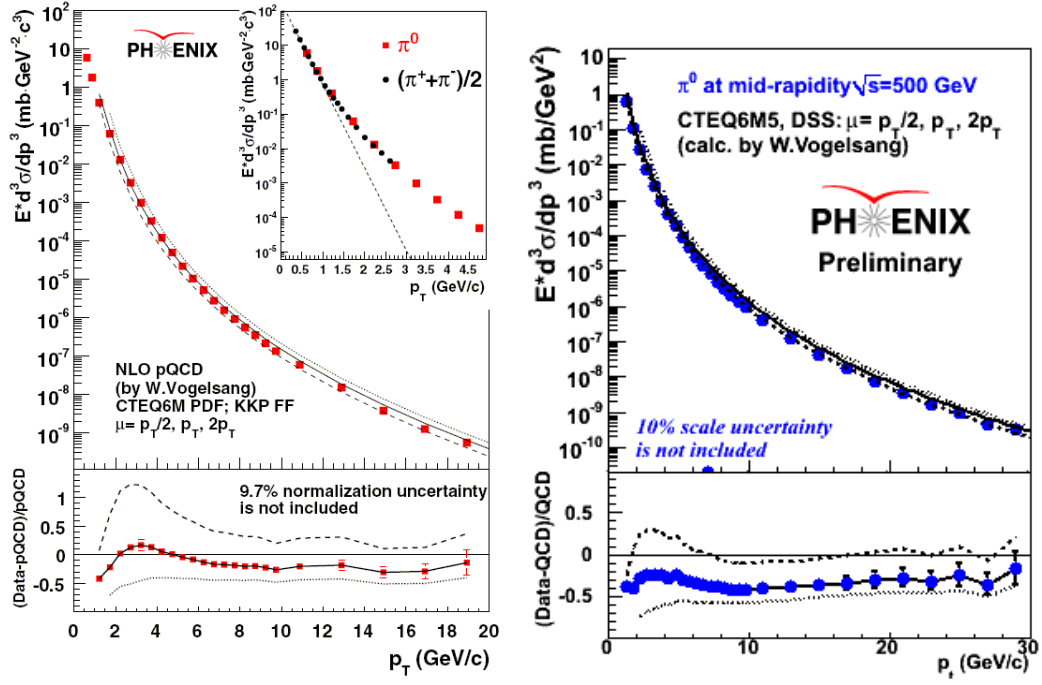


Figure 5.3: PHENIX $\sqrt{s} = 200$ and 500 GeV results.

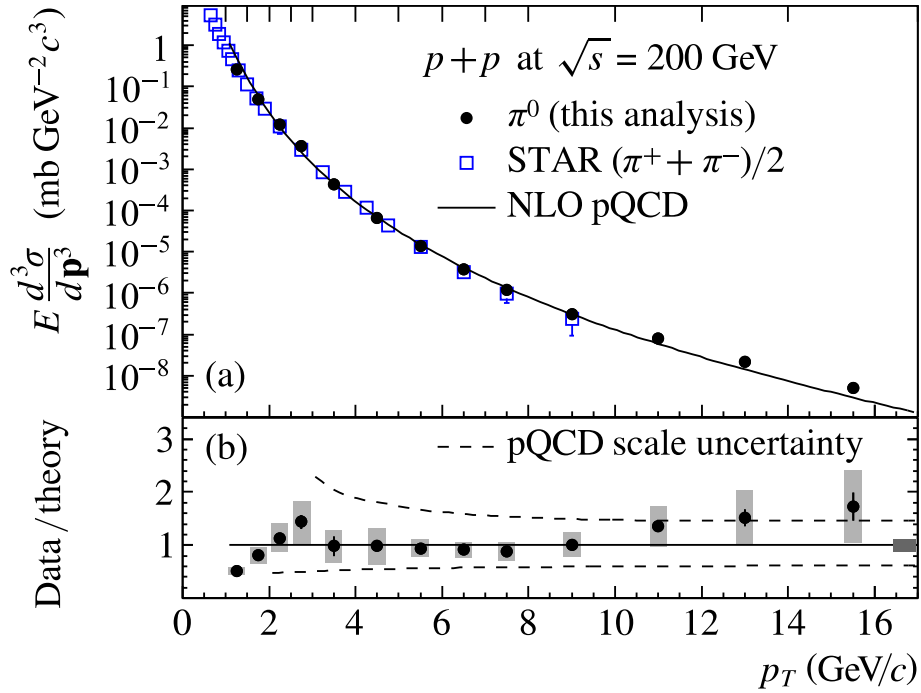


Figure 5.4: STAR $\sqrt{s} = 200$ GeV BEMC result.

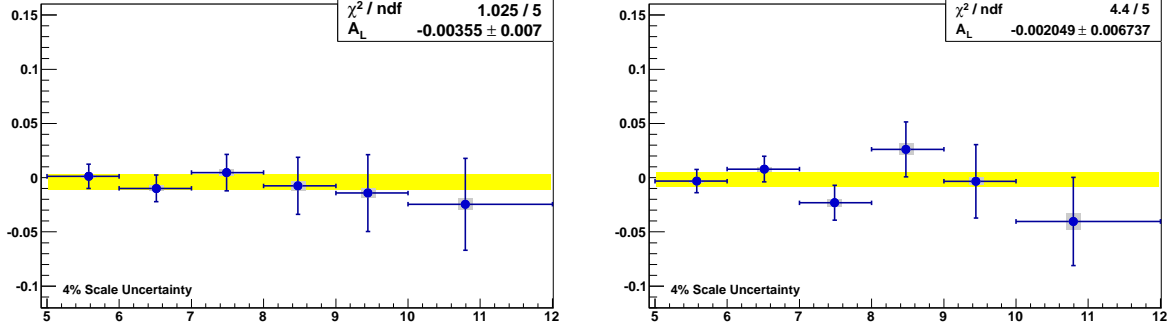


Figure 5.5: The $\pi^0 A_L$ results, including a fit to a constant value. Left panel is for the blue beam asymmetry and the right panel is for the yellow beam asymmetry. The error bar indicates the statistical uncertainty and the error box indicates the systematic uncertainty.

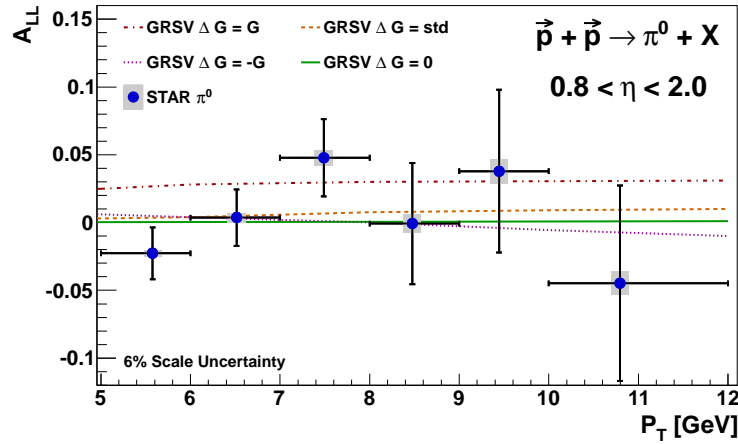


Figure 5.6: The $\pi^0 A_{LL}$ results in comparison with a pQCD calculation [30]. The error bar indicates the statistical uncertainty and the error box indicates the systematic uncertainty. *[This plot is intended for the publication.]*

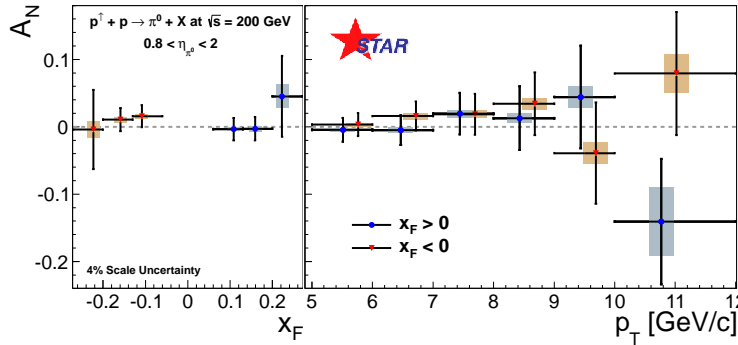


Figure 5.7: Final A_N result. Left panel is versus x_F and right panel is versus p_T . Statistical uncertainties are indicated by the uncertainty bar, and the systematic uncertainties are indicated by the uncertainty band.

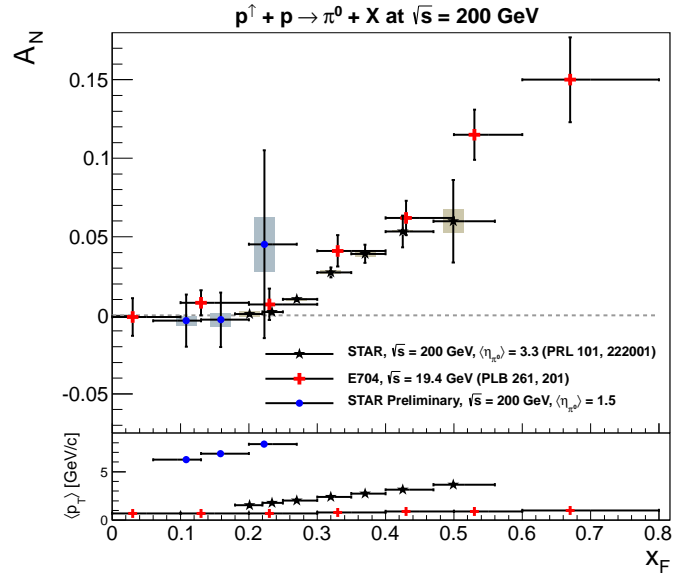


Figure 5.8: Comparison of these (EEMC) results with previously published results.

Appendix A

Run Lists

A.1 Longitudinal Runs for both Asymmetry and Cross Section

7132001 7132005 7132007 7132009 7132010 7132018 7132023 7132026 7132027 7132059
7132061 7133049 7133050 7133052 7133064 7133065 7133066 7133068 7134001 7134005
7134006 7134007 7134009 7134010 7134013 7134015 7134026 7134027 7134030 7134043
7134046 7134047 7134048 7134049 7134052 7134055 7134056 7134065 7134066 7134067
7134068 7134072 7134074 7134075 7134076 7135003 7135004 7136017 7136022 7136023
7136024 7136027 7136031 7136033 7136034 7136035 7136039 7136040 7136041 7136042
7136045 7136073 7136075 7136076 7136079 7136080 7136084 7137012 7137013 7137035
7137036 7138001 7138002 7138003 7138004 7138008 7138009 7138010 7138011 7138012
7138017 7138029 7138032 7138034 7138043 7139018 7139019 7139025 7139031 7139032
7139043 7140007 7140008 7140009 7140010 7140011 7140015 7140016 7140017 7140018
7140022 7140023 7140024 7140042 7140045 7140046 7140051 7140052 7141010 7141011
7141015 7141016 7141034 7141038 7141039 7141042 7141043 7141044 7141064 7141066
7141069 7141070 7141071 7141074 7141075 7141076 7141077 7142001 7142005 7142016
7142017 7142018 7142022 7142024 7142025 7142028 7142029 7142033 7142034 7142035
7142036 7142045 7142046 7142047 7142048 7142049 7142059 7142060 7142061 7143001
7143004 7143005 7143006 7143007 7143008 7143011 7143012 7143013 7143014 7143025
7143054 7143055 7143056 7143057 7143060 7144011 7144014 7144015 7144018 7145009
7145010 7145013 7145017 7145018 7145019 7145022 7145023 7145024 7145025 7145026
7145030 7145057 7145064 7145067 7145068 7145069 7145070 7146001 7146004 7146006
7146016 7146019 7146020 7146024 7146025 7146066 7146067 7146068 7146069 7146075
7146076 7146077 7146078 7147052 7147055 7147083 7148020 7148024 7148027 7148028
7148032 7148036 7148037 7148054 7148057 7148059 7148063 7148064 7148065 7148066
7148067 7149003 7149004 7149005 7149018 7149019 7149023 7149026 7150007 7150008
7150013 7152035 7152037 7152049 7152051 7152062 7153001 7153002 7153008 7153014
7153015 7153021 7153025 7153032 7153035 7153103 7154004 7154005 7154044 7154047
7154051 7154068 7154069 7154070 7155009 7155010 7155011 7155013 7155016 7155018
7155019 7155022 7155023 7155042 7155043 7155044 7155048 7155052 7155053 7156006
7156010 7156017 7156018 7156019 7156024 7156025 7156026 7156027 7156028 7133051
7133053 7134035 7136030 7137011 7137014 7139017 7139022 7139024 7140014 7143043
7143044 7143046 7143047 7143049 7145011 7146008 7146009 7147014 7148013 7148019
7153007 7153020 7154052 7155046 7156008

A.2 Additional Longitudinal Runs for the Cross Section

7135016 7135018 7135019 7135022 7135023 7135024 7135025 7135028 7143045 7143048
7135027 7140053

A.3 Transverse Runs for both Asymmetry and Cross Section

7097093 7097094 7097096 7097097 7097099 7097102 7097103 7097104 7097105 7098001
7098002 7098004 7098006 7098007 7098008 7098015 7098018 7098024 7098025 7098027
7098028 7098029 7098031 7098032 7098033 7098034 7098036 7098038 7098039 7098040
7098041 7098053 7098055 7098061 7098062 7098064 7098065 7098066 7098067 7098072
7098074 7098075 7098079 7098081 7098082 7098083 7099003 7099006 7099014 7099015
7099016 7099022 7099024 7099025 7099026 7099027 7099030 7099031 7099033 7099034
7099035 7100014 7100016 7100031 7100052 7100055 7100058 7100062 7100064 7100068
7100071 7100072 7100075 7100077 7101013 7101015 7101019 7101023 7101025 7101041
7101042 7101046 7101050 7101052 7101054 7101075 7101078 7101082 7101085 7101086
7103006 7103007 7103008 7103013 7103014 7103017 7103018 7103024 7103026 7103027
7103030 7103040 7103072 7103073 7103075 7103080 7103082 7103086 7103089 7103090
7103093 7103095 7103099 7104014 7104016 7115085 7115086 7115087 7115088 7115095
7115097 7115099 7115101 7115103 7115106 7115111 7115113 7115114 7115115 7115116
7115117 7115121 7115122 7115124 7115125 7115126 7115131 7115134 7116044 7116050
7116052 7116057 7116059 7117002 7117008 7117009 7117010 7117011 7117015 7117016
7117017 7117027 7117050 7117056 7117057 7117058 7117060 7117063 7117064 7117071
7118002 7118003 7118004 7118008 7118009 7118010 7118014 7118016 7118017 7118024
7118026 7118032 7118033 7118035 7118038 7118039 7118041 7118044 7118045 7118048
7118049 7118050 7118051 7118053 7118073 7118075 7118077 7118083 7118084 7118085
7118087 7118088 7118092 7119001 7119002 7119003 7119004 7119019 7119020 7119021
7119022 7119028 7119032 7119065 7119068 7119069 7119079 7119080 7119082 7119084
7119085 7119088 7119090 7119091 7120082 7120085 7120088 7120089 7120091 7120092
7120093 7120100 7120101 7120112 7120113 7120116 7120117 7120121 7120128 7120129
7120131 7120132 7120133 7121001 7121007 7121012 7121013 7121015 7121016 7121020
7121021 7121024 7121041 7121043 7125005 7125013 7125014 7125015 7125016 7125017
7125018 7125021 7125022 7125023 7125028 7125044 7125052 7125053 7125055 7125056
7125057 7125058 7125059 7125061 7125066 7125067 7125069 7125070 7126008 7126009
7126010 7126011 7126012 7126016 7126019 7126022 7126023 7126025 7126036 7126037
7126056 7126057 7126058 7126059 7126062 7126063 7126064 7126065 7127001 7127005
7127006 7127007 7127009 7127010 7127011 7127033 7127037 7127038 7127039 7127041
7127042 7127045 7127046 7127049 7127050 7127067 7127069 7127072 7127073 7127075
7127076 7127077 7127080 7127087 7127090 7127092 7127096 7128001 7128002 7128005
7128006 7128007 7128008 7128009 7128013 7128023 7128024 7128025 7128028 7128032
7128045 7128046 7128048 7128050 7128051 7128057 7128059 7128061 7128063 7129001
7129002 7129003 7129009 7129018 7129020 7129021 7129023 7129027 7129031 7129032
7129035 7129036 7129041 7097009 7097010 7097014 7097017 7097018 7097019 7097020
7097021 7097024 7097025 7097026 7097027 7097032 7097095 7098014 7098073 7098080
7099021 7099047 7100015 7100028 7100029 7100067 7100070 7100076 7100078 7101039
7103016 7103081 7103087 7103088 7103096 7115011 7115024 7115089 7115130 7115137
7117067 7117068 7118042 7120023 7120045 7120046 7120047 7120049 7120053 7121038
7121118 7121119 7121120 7121122 7122002 7122003 7122004 7122035 7122037 7122043
7122044 7122045 7122046 7122047 7122048 7122049 7122053 7122054 7122056 7122057
7122058 7122069 7122070 7123014 7123015 7123019 7123020 7123022 7123024 7123025
7123027 7123028 7123030 7123031 7123032 7124009 7124016 7124018 7124021 7124024
7124026 7124029 7124031 7124034 7124063

A.4 Additional Transverse Runs for the Cross Section

7114068 7114070 7114071 7114073 7114076 7114077 7114079 7114080 7114081 7114082
7114083 7114084 7114085 7114088 7114091 7114092 7114093 7114101 7114102 7114103
7114106 7115002 7115003 7115007 7115008 7115009 7115010 7115016 7115017 7115022
7115029 7115030 7115033 7115034 7115038 7115039 7115040

Bibliography

- [1] <http://drupal.star.bnl.gov/STAR/blog/spinka/2012/sep/09/run6-runlist>
- [2] http://www.star.bnl.gov/protected/spin/sowinski/runQC_2006/
- [3] http://www.star.bnl.gov/protected/spin/sowinski/runQC_2006/prior.csv.txt
- [4] List of relative luminosities per run.
- [5] <http://www4.rcf.bnl.gov/~cnipol/pubdocs/Run060offline/>
- [6] W. He, “The Double Spin Asymmetry in Inclusive π^0 Production for Longitudinally Polarized pp Collisions at $\sqrt{s} = 200$ GeV at the Endcap Electromagnetic Calorimeter at STAR.” PhD dissertation, Indiana University (2008). <http://drupal.star.bnl.gov/STAR/node/14867>
- [7] <http://drupal.star.bnl.gov/STAR/blog/sgliske/2012/aug/28/varying-thesholds-2006-eemc-http-mb-l2gamma>
- [8] Values are based on initialize files for the simulated trigger. Discrepancies exist about the exact dates of validity.
- [9] J. Dunlop’s Trigger FAQ for 2006. <http://orion.star.bnl.gov/protected/common/common2006/trigger2006/triggers2006.html>
- [10] Presented Oct. 16th, 2012. <http://drupal.star.bnl.gov/STAR/system/files/2012-10-02-EEMC-SamplingFraction-Gibson-SlightlyUpdated.pdf>
- [11] <http://drupal.star.bnl.gov/STAR/blog/drach09/2012/sep/04/pseudorapidity-fiducial-volume>
- [12] <http://drupal.star.bnl.gov/STAR/blog/sgliske/2012/jul/20/eemc-pi0-cut-optimization>,
<http://drupal.star.bnl.gov/STAR/blog/sgliske/2012/jul/21/more-mc-pi0-cut-optimization>,
<http://drupal.star.bnl.gov/STAR/blog/sgliske/2012/jul/23/eta-cut-eemc-pi0s>.
- [13] <http://drupal.star.bnl.gov/STAR/blog/sgliske/2013/feb/07/repeat-cut-review>,
<http://drupal.star.bnl.gov/STAR/blog/sgliske/2013/apr/09/minor-updates-february>
- [14] The official simulation request page. <http://drupal.star.bnl.gov/STAR/starsimrequests/2010/jul/27/run-6-photon-jet-simulation-request-spin-physics>
- [15] J. Drachenberg, “Forward Di-hadron Asymmetries from Polarized p+p at $\sqrt{s} = 200$ GeV.” PhD dissertation, Texas A&M University (2012). <http://drupal.star.bnl.gov/STAR/node/23775>
- [16] G. G. Ohlsen and P. W. Keaton, Jr., Nucl. Instrum. Meth. 109, 41 (1973).
- [17] <http://drupal.star.bnl.gov/STAR/blog/sgliske/2013/mar/27/updated-pi0-longitudinal-background-asymmetries>
- [18] <http://drupal.star.bnl.gov/STAR/blog/drach09/2013/mar/14/2006-eemc-neutral-pions-update-spin-pwg-march-14-2013>
- [19] <http://drupal.star.bnl.gov/STAR/blog/drach09/2012/nov/30/2006-eemc-neutral-pions-systematics-bin-smearing>

- [20] See many emails on the Phana mailing list, March through November, 2010, e.g. <http://www.star.bnl.gov/HyperNews-star/protected/get/phana/452.html>. Also see blogs from Ilya and <http://drupal.star.bnl.gov/STAR/node/17179> and Alice <http://drupal.star.bnl.gov/STAR/blog/aliceb/2010/jan/15/endcap-gamma-filtered-mc-bias-tests> and a document prepared by Mike <http://drupal.star.bnl.gov/STAR/system/files/gammafilter.pdf>.
- [21] <http://drupal.star.bnl.gov/STAR/blog/drach09/2013/mar/28/2006-eemc-neutral-pions-updated-kinematic-range>
- [22] <http://drupal.star.bnl.gov/STAR/blog/drach09/2013/mar/20/2006-eemc-neutral-pions-update-spin-pwg-march-21-2013>
- [23] <http://drupal.star.bnl.gov/STAR/blog/drach09/2013/mar/28/2006-eemc-neutral-pions-update-spin-pwg-march-28-2013>
- [24] <http://drupal.star.bnl.gov/STAR/blog/sgliske/2013/apr/08/additive-vs-multiplicative>
- [25] <http://drupal.star.bnl.gov/STAR/blog/sgliske/2013/apr/04/eemc-energy-scale>
- [26] Phys. Rev. D **80** (2009) arXiv:0911.2773
<http://drupal.star.bnl.gov/STAR/publications/longitudinal-double-spin-asymmetry-and-cross-section-inclusive-ne>
- [27] Phys. Rev. Lett. **97** (2006)
- [28] Phys. Rev. D **86** (2012)
- [29] NIM A **355** (1995) 541-547
- [30] Private communication.
- [31] <http://drupal.star.bnl.gov/STAR/presentations/spin2008/scott-wissink>
- [32] <http://drupal.star.bnl.gov/STAR/blog/sgliske/2013/mar/20/bjorken-x-eemc-pi0s>